4. Comparison with Observations

4.1. Introduction

The previous chapters make some specific predictions about the nature of the wind-field in the tropical cyclone boundary-layer. These can be briefly summarised as:

- *The surface-wind factor increases from 0.6 to 0.7 in the outer core to 0.8 to 1.0 near the eyewall, and is greater on the left of the storm (in the Northern Hemisphere).*
- *The azimuthal-mean azimuthal wind in the upper boundary-layer is slightly supergradient in the cyclone periphery, and increasingly so near the core. The amount varies according to the storm intensity and radial wind profile. The boundary-layer depth decreases from around 1.5 km at 100-km radius to about 500 m in the inner core.*
- *In a moving storm, the jet is more strongly supergradient on the left (right) side in the Northern (Southern) Hemisphere.*

The purpose of this chapter is to test these predictions against data.

Some of the above lend themselves to relatively easy, qualitative verification. For instance, the predicted difference in shape in the wind vertical-profile in the boundary-layer between the left and right sides of the storm ought not to be hard to check. The predicted surface-wind factor field is again likely to be easy to check. However, verifying that the winds in the upper boundary-layer are super-gradient demands more thorough analysis. It is not sufficient to simply prepare analyses of the wind and pressure observations and compare these through the gradient-wind equation. This would bypass two important questions: firstly, by how much are the winds supergradient, and secondly, how confident are we that any apparent gradient imbalance is real, rather than an artifact of the nature of the observations or the analysis technique.

Answering the second of these clearly implies that the analysis of gradient balance (or otherwise) must include the estimation of the errors in the analysis. Indeed, as analyses of spatial fields invariably contain spatially correlated errors, a direct calculation would require the estimation of the full analysis error covariance matrix, to correctly propagate errors when analysed fields are differentiated or integrated. This would be cumbersome, not least because the gradient-wind equation is nonlinear. Thus a Monte-Carlo method will be used instead, to estimate the errors and place confidence intervals on the analyses.

It is also important to note that analysing gradient balance near the eyewall of a tropical cyclone places significant demands on the analysis accuracy. A particular concern is the accuracy to which the observations are located relative to the cyclone. For instance, if the RMW is 40 km, an error in the cyclone track (or observation location) of 5 km will lead to a 12% error in the centripetal term in the gradient-wind equation. This is similar to the maximum extent to which the winds were supergradient in the moderate cyclone in Chapter 3, and thus unacceptable. Yet post-analysis best track data bases typically give the cyclone position to 0.1 degree of latitude and longitude, or roughly 10 km. Thus round-off error in the reporting of the best-track alone can potentially give errors which invalidate the analysis of gradient-wind balance, even in the event it was initially prepared to higher precision than 0.1 degree.

It is useful at this point to briefly review some previous contributions. Gray (1967) and Gray and Shea (1973) analysed aircraft winds at two levels by compositing them relative to the RMW and comparing the vertical shear to the aircraft observations of horizontal temperature gradient, through the cylindrical-coordinates form of the thermal wind equation. The main reason for using this, rather than the gradient-wind

equation, was that the winds were measured by Doppler radar measurement of the aircraft motion relative to the sea surface, which introduced a systematic bias as the surface was drifting due to the wind stress. Subtracting winds at two levels removed this. The winds were composited relative to the RMW on each flight radial leg, and across several storms. Gray and Shea (1973) found the winds were supergradient at all levels immediately inside of the RMW, and his figures show that this was perhaps more marked at the 900 hPa level, than further aloft.

Willoughby (1990) used more accurate winds derived from inertial navigation equipment, composited data from only single storms, and relative to distance from the centre, not the RMW. His data covered a period of typically 6 hours, and his analyses included both an estimate of the wind and pressure radial profiles, and their (linear) time variation. Analyses were prepared using an adaptation of the statistical scheme of Ooyama (1987) which employs cubic B-splines as the analysis basis functions. He presented analyses for 13 storms, and found no evidence of supergradient flow. However he did not include any discussion of analysis error, and some important details in the analysis were not sufficiently described. In particular, the grid on which the B-splines were defined was not given, nor were the spatial smoothing parameters applied, the assumed error characteristics of the observations, and the resulting analysis error.

Gray's (1991) comment on Willoughby's (1990) results largely re-presented his earlier work, while Willoughby's (1991) reply included some further storms and emphasised his perceived short-comings in Gray's analysis technique. His objections to Gray's compositing relative to the RMW, and across several storms, seem to be particularly well founded. On the other hand, Gray pointed out that the majority of Willoughby's flights were at 850 or 700 hPa, while his included a significant amount of

900 hPa data, and suggested that the lower level was more conducive to supergradient flow. On this latter point, Willoughby (1990) had contained a crude calculation which suggested the possibility of supergradient flow in the boundary-layer.

A significant weakness on both sides of the argument is the absence of statistical analysis. For instance, Gray's case would have been much stronger had he used any of the well-known techniques for showing two quantities are different, such as null hypothesis significance testing, or confidence intervals. Similarly, one might expect that, given the large amount of relatively accurate data used, that Willoughby's analysis errors were fairly small. But his case would have been more impressive had he actually calculated these.

4.2 Hurricane Georges

4.2.1 Introduction and Data Coverage

Hurricane Georges was one of the major storms for the 1998 Atlantic season, reaching a peak intensity of 135 knots. In this section, the structure of the low-level winds will be analysed in detail at about the time of peak intensity. First, however, we give a brief description of the life-cycle of Georges, and of the two aircraft reconnaissance missions which took the measurements to be analysed here. This opening discussion draws heavily on the Hurricane Preliminary Report by Guiney (1999), and the Mission Summaries by Aberson (1998) and Black (1998).

Hurricane Georges (see Fig 4.1 for the track) formed from an easterly wave which crossed the coast of Senegal on 13th September, 1998. A closed circulation had formed by early on the 15th, and the US National Hurricane Centre (NHC) estimated that the system reached tropical depression status at 1200 UTC, when it was about 500 km SSW of the Cape Verde Islands. The system intensified steadily over the next few days as it followed a steady track towards the WNW, reaching tropical storm intensity at 1200 UTC on the 16th, and hurricane intensity at around 1800 UTC on the 18th.

Intensification became more rapid on the 19th, under the influence of an upper-level anticyclone over Georges. The NHC best-track analysis indicated that peak intensity of 135 knots, with a central pressure of 937 hPa, was reached at 0600 UTC on the 20th. The analysis at this time included the use of aircraft reconnaissance and dropsonde data. Georges weakened markedly after this, under the influence of upper-level north-westerly shear, before making the first of several landfalls on Antigua at 0430 UTC on the 20th with a central pressure of 966 hPa. Further landfalls followed on St Kitts and Nevis, Puerto Rico, the Dominican Republic and Cuba over the next 42 hours,

while the storm continued its general weakening trend.

Passing back over the ocean, Georges began to re-intensify, before making landfall at 1530 UTC on the 25th at Key West, Florida, with a central pressure of 981 hPa. After moving into the Gulf of Mexico, Georges slowed and turned gradually northwards, under the influence of a mid-tropospheric anticyclone which migrated from being north of the storm, into the southeastern United States. Georges made its final landfall at 1130 UTC on the 28th at Biloxi, Mississippi, before drifting generally eastwards as it dissipated.

A three aircraft mission was flown into Georges by the NOAA Hurricane Research Division from late on the 19th, into the early 20th. The goals of the mission were to measure the synoptic flow surrounding Georges, and for two of the three aircraft to make deployments of GPS dropsondes in the cyclone core, particularly near the eyewall. The first of these (Black 1998) began its initial “figure-4" pattern through the core at 1911 UTC on the 19th, beginning about 90 km to the west of the eye. A west-east pass through the eye was followed by north-south and south-north passes, each extending about 80 km from the centre and finishing at 2037 UTC. A total of 12 dropsondes were launched, eight in the eyewall and four at the ends of the radial flight legs. The aircraft then continued with the synoptic surveillance part of the mission. Performance of the dropsondes was good, apart from a tendency for the eyewall wind measurements to fail in the lowest few tens of metres.

The second set of core measurements began at about 0000 UTC on the 20th (Aberson 1998) to the north of the eye. A single “figure-4" pattern was flown during which 16 dropsondes were deployed. Dropsonde performance for this flight was similar

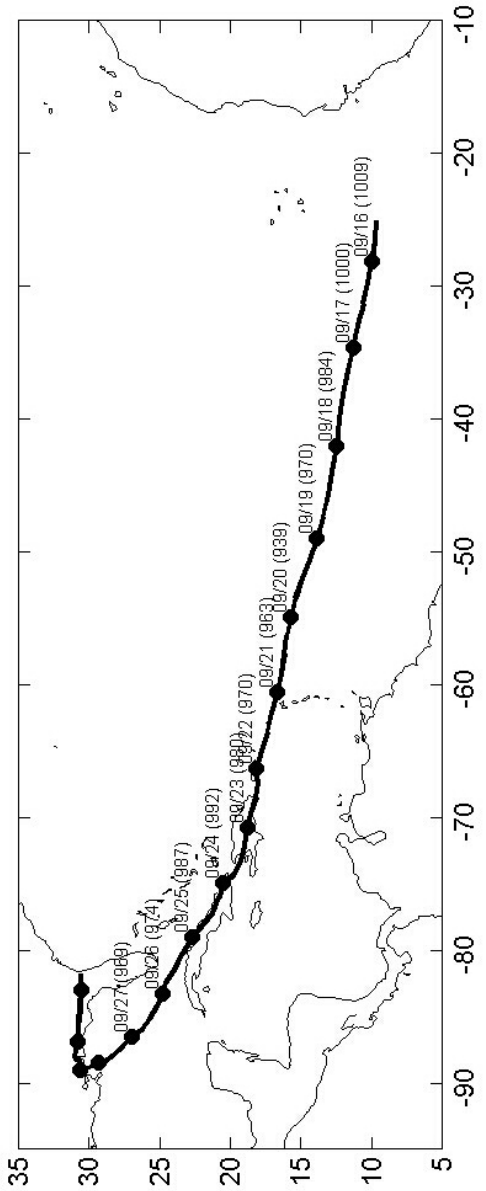

Figure 4.1 The best-track analysis for Hurricane Georges from the U.S. National Hurricane Center. Tick marks showing the month, day and estimated central pressure (hPa) are at 00UTC.

to the earlier flight, that is, good apart from several wind failures near the surface in the eyewall. The storm-relative aircraft tracks and dropsonde deployment points are shown in Fig 4.2. These two periods of observations will for convenience be referred to as the "early" and "late" periods.

In addition, a reconnaissance flight conducted by the US Air Force partially overlapped the first of the HRD missions, and deployed another three dropsondes in the eye and eyewall. These were also obtained.

During this period of intensive observations, Hurricane Georges had a well-defined eye with a highly symmetric inner core, as evidenced by radar and passive microwave imagery (Fig 4.3 and 4.4). Black (1998) described the eye thus:

> "Hurricane Georges had a well-defined, closed, and nearly symmetrical eyewall as viewed by the belly radar, and the tail radar showed echo tops as high as 18 km. The eye was almost completely clear except for some shallow cumulus above the sea surface. The eyewall was visually spectacular, with detailed and complex structure, a pronounced outward slope, and cirrus overhang."

Furthermore, Knaff et al. (2002 and personal communication) identified Georges during this period as an annular hurricane, that is, a cyclone for which "the IR imagery is characterised by a large circular eye surrounded by a nearly uniform ring of deep convection with a distinct lack of deep convective features (i.e. spiral bands) outside this ring".

Hurricane Georges at this time was thus largely free of other sources of asymmetry, such as shear or proximity to landfall. It is therefore an ideal candidate for testing the theory developed in chapters 2 and 3. In the absence of other causes, it is be

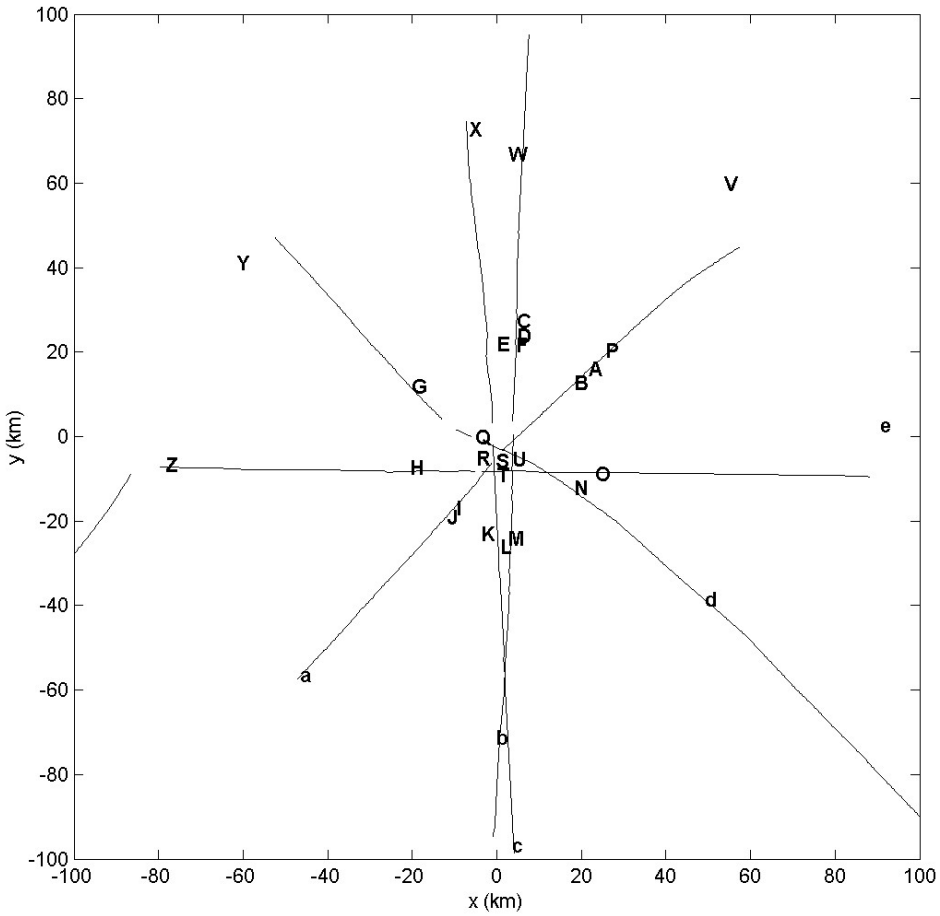

Figure 4.2 The aircraft reconnaissance "radial legs" and deployment points of dropsondes used in this study, in storm-relative coordinates.

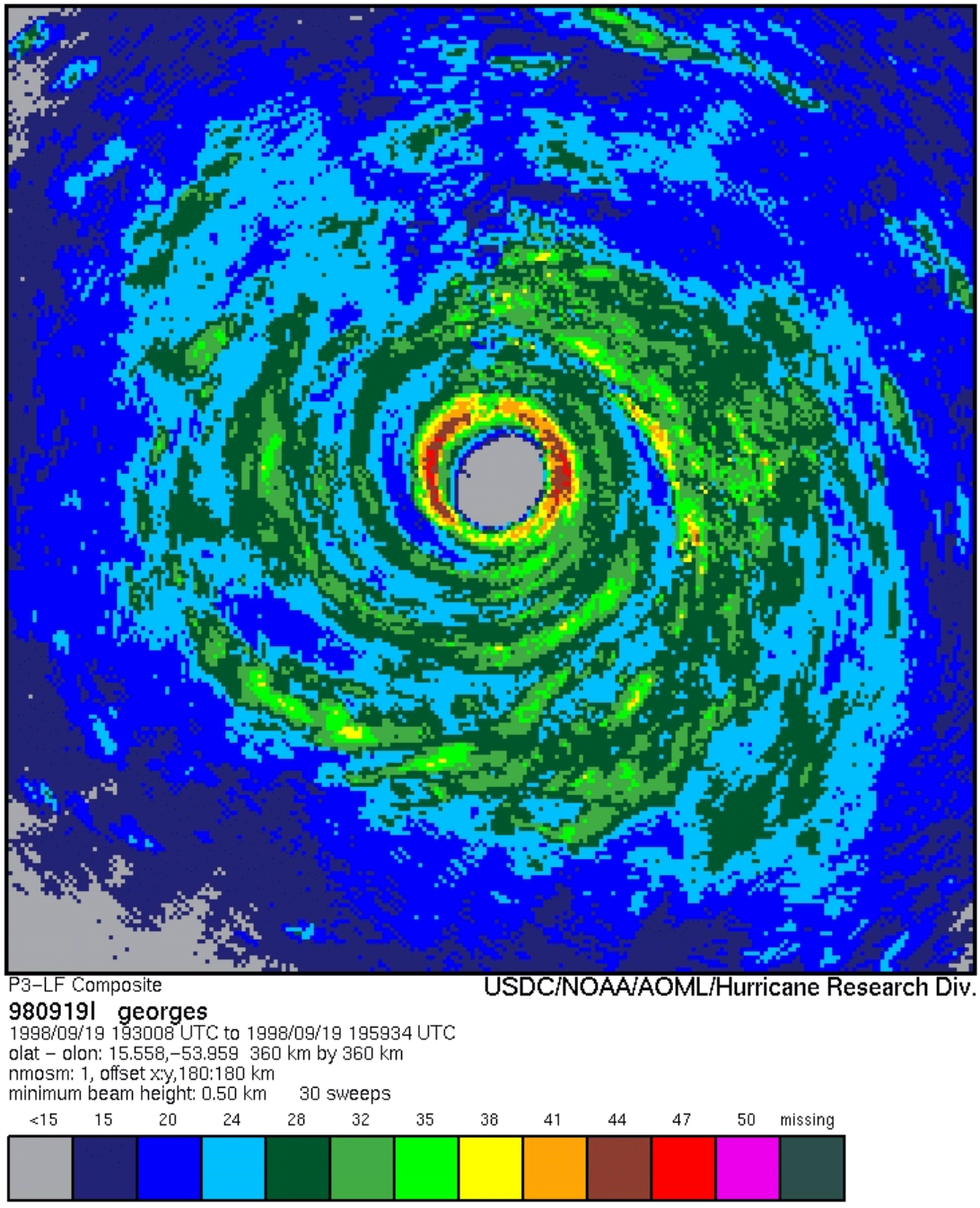

Figure 4.3 Composite radar reflectivity image from HRD reconnaissance aircraft between 1930 and 1959 UTC on 19 September 1998. Image courtesy of NOAA HRD.

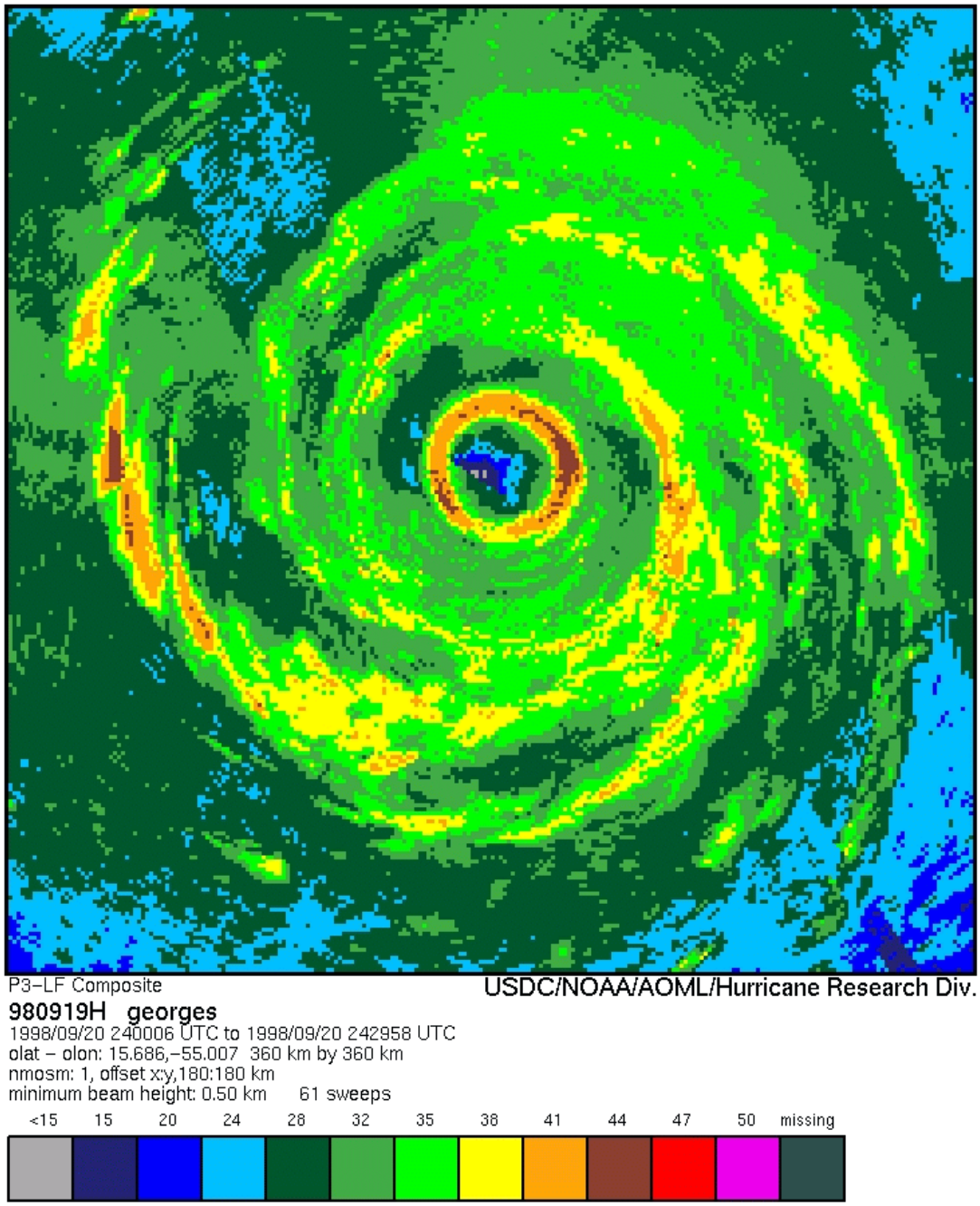

Figure 4.4 The same as Fig 4.3, except between 0006 and 0030 UTC on 20 September 1998. Image courtesy of NOAA HRD,

Name	Serial No	Date/Time (UTC)	Lat (N)	Lon (W)	Pr (hPa)	Comments
Hurricane Research Division N42RF						
d	981750008	980820/000304	15.42	54.46	582	RH2, too wet at sfc?
N	981820069	980820/000811	15.66	54.77	558	Eyewall. Triple wind max. RH too wet low?
Q	981820011	980820/001119	15.77	55.00	552	Eye.
G	973720021	980820/001339	15.88	55.15	557	Eyewall.
Y	974150010	980820/002147	16.15	55.57	586	3 mb PR corr. RH2 used.
a	981750001	980820/003231	15.28	55.47	584	None
J	981740056	980820/003836	15.62	55.17	567	Eyewall. Did not hit sfc.
I	981820065	980820/003900	15.64	55.15	561	RH too dry aloft, too wet near sfc?
B	974730072	980820/004332	15.91	54.91	563	Sloping max RH too dry aloft?
A	981820016	980820/004412	15.94	54.88	557	Eyewall.
V	981820058	980820/005157	16.34	54.61	584	None
W	982630003	980820/010229	16.41	55.13	701	Sloping RH max.
E	981820041	980820/010855	16.01	55.18	673	Eyewall. 10 m/s updraft.
R	982720294	980820/011232	15.77	55.24	664	Eye.
K	982630078	980820/011455	15.61	55.24	681	Eyewall. Dry bias corrected.
b	975020049	980820/012116	15.18	55.23	701	Sloping RMAX doubtful.
Hurricane Research Division N43RF						
Z	974530024	980819/191143	15.50	54.50	572	None
H	974730061	980819/191837	15.50	53.99	568	Eyewall.
O	981820001	980819/192341	15.49	53.60	567	Eyewall.
e	973910029	980819/193333	15.60	53.01	573	None
X	974530114	980819/194635	16.24	53.97	569	None
T	974530110	980819/195702	15.51	53.95	572	Near-sfc RH?
L	973840053	980819/195910	15.36	53.95	569	Near sfc RH?
c	974510127	980819/200819	14.73	53.96	569	RH2 used.
M	982430062	980819/201846	15.39	54.01	564	Eyewall.
F	982430041	980819/202816	15.81	54.03	568	Eyewall.
D	974150035	980819/202832	15.83	54.03	564	Eyewall.
C	974940047	980819/202849	15.86	54.03	557	Eyewall
Air-force reconnaissance						
P	981010052	980919/190626	15.74	53.51	697	NE eyewall.
S	981010060	980919/191315	15.51	53.78	697	Eye. RH looks low but not changed.
U	981030005	980919/204850	15.58	54.12	697	Eye. RH looks low, but was not changed.

Table 4.1 Dropsonde data used for the analysis of Hurricane Georges. The first two columns give the letter used to identify the sonde in this report and the manufacturers serial number. The next four columns give the time and location of the launch, followed by comments from the responsible mission scientist. Only those sondes used in the analysis (i.e. within 100 km of the cyclone centre) are included in the table.

expected that the low-level asymmetry will be well-explained by the motion. Further, the relative symmetry and good data coverage also makes Georges a good candidate for an analysis of the azimuthally-averaged gradient balance.

The data used in this analysis were:

- Thirty-one GPS dropsonde soundings within approximately 100 km of the centre of the storm. These were obtained in post-processed, quality-controlled form from HRD and are summarised in Table 4.1. Additional soundings from distances ranging from 300 to several thousand kilometres were also obtained, but are not used here. The soundings consist of measurements of temperature, humidity, pressure, wind and location at 0.5 s intervals, together with height values found by a hydrostatic integration. For reasons to be discussed below, it was necessary to discard the height data and redo the hydrostatic integrations. The soundings also included the aircraft altitude at release time (from a radar altimeter) and an estimate of the height of the last pressure observation (usually less than 10 m, obtained by examination of the telemetry signal), either of which can provide a boundary condition for the hydrostatic integration. The final pressure and height can be used with the hydrostatic equation to estimate a surface pressure, which shall be called the "splash pressure". Full details of the GPS dropsonde system are contained in Hock and Franklin (1999).
- Research aircraft measurements of three-dimensional wind, thermodynamic, and storm track data. These were storm-relative winds in cylindrical coordinates, averaged into 0.5 km radius bins for each of the twenty radial legs flown.
- Several radar composite images from the lower-fuselage radar on the HRD aircraft.
- Various infra-red, visible and passive microwave satellite imagery from GOES

and DMSP satellites.

- Analyses of the track of Georges from NHC and HRD. Two analyses were available from HRD, with different degrees of smoothing. These will be referred to as the HRD high-resolution and low-resolution tracks. The various tracks are discussed in more detail below.

4.2.2 Cyclone Track

All dropsonde and aircraft data were first renavigated into a Cartesian coordinate system with origin tangent to the earth at 15.55°N, 54.20°W and the *y*-axis directed northwards. Times were expressed relative to a nominal base time of 2100 UTC on September 19th, 1998. The base latitude and longitude chosen were the location of Georges at this time, interpolated from the NHC best-track analysis. The HRD aircraft storm-relative cylindrical coordinate wind data were converted back into earth-relative Cartesian winds, using the same track (i.e. the HRD high-resolution) as for their conversion to storm-relative cylindrical coordinates.

The three track analyses available are shown in Fig 4.5. It can be seen that the NHC and HRD low-resolution tracks differ by up to 10 km, but are of similar resolution, while the HRD high-resolution track contains a trochoidal oscillation missing from the other tracks. Part of the difference is probably due to the fact that the NHC track is nominally a surface track, while the HRD tracks are determined by objectively fitting smoothing splines through reconnaissance aircraft "fixes" at various levels. Centres from HRD aircraft data are given greater weight than those from other aircraft, satellite or radar data. In particular, the HRD high-resolution track is based largely on centre fixes at 600 hPa from the missions described above.

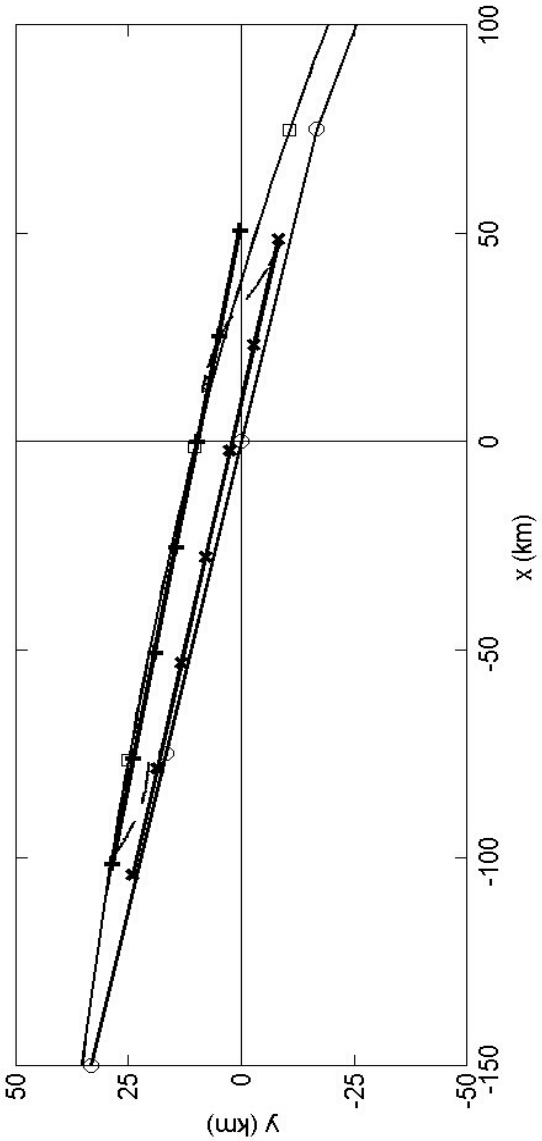

Figure 4.5 Various tracks for Hurricane Georges during the study period. They are the NHC best-track (thin line with circles), the HRD low-resolution (thin line with squares) and high-resolution (broken thin line) tracks, and the tracks found by applying the Marks-circulation method to the flight-level earth-relative wind data (heavy line with ×'s), and translating-pressure-fit methods to the flight-level pressure-height data (heavy line with +'s). Tick marks are at three hour intervals for the first two, omitted for the third, and hourly for the latter two.

The differences between these tracks are important, because of the high sensitivity of gradient-wind balance calculations to the radius of curvature. Moreover, it may also be necessary to allow for tilt of the cyclone in analyses at different levels (Marks et al.1992). While this is not expected to be large in the case of Georges, it could be for other storms. This can only be determined from the data; thus it is necessary to develop techniques to objectively determine track that work on both dense data (at flight-level) and relatively sparse data (i.e. dropsondes, below flight-level).

Marks et al. (1992) calculated the track of Hurricane Norbert from Doppler radar wind data by maximising the circulation C around the centre of the storm. That is, maximising

$$C(\boldsymbol{a}) = \sum_{i=1}^{n_{\text{obs}}} v_{\text{az}}(\boldsymbol{u}_i, \boldsymbol{x}_i, t_i; \boldsymbol{a}) \qquad \textbf{(4.1)}$$

where $\boldsymbol{a} = (x_t, y_t, u_t, v_t)$, (x_t, y_t) is the cyclone location at time 0 and (u_t, v_t) its motion vector, v_{az} is the azimuthal wind calculated from the observed earth-relative wind $\boldsymbol{u}_i$ at location $\boldsymbol{x}_i$ and time t_i given the track $\boldsymbol{a}$, and n_{obs} is the number of observations. The maximisation was carried out using the simplex method of Nelder and Mead (1965; see also Press et al.1992 section 10.4). The maximisation can in principal be carried out with v_{az} being either the storm-relative or earth-relative azimuthal wind, although Marks et al. (1992) used the earth-relative wind. For uniformly spaced observations, these produce very similar results. However, it was found that using the earth-relative winds occasionally can produce large errors when the data were unevenly spaced in azimuth, as well as a less vertically consistent track, than was found when using the storm-relative wind. On the other hand, the iteration can diverge (with enormous translation speeds)

if too few data are available and the storm-relative winds are used. Either of these problems may arise when a small amount of data, such as the dropsonde winds, are used. (Marks et al. applied the method to Doppler radar winds with fairly uniform and complete coverage). This method will henceforth be called the Marks-circulation method.

Using flight-level wind data, the track was found by this method to be given by $(x_t, y_t) = (-1.7, 8.9)$ km and $(u_t, v_t) = (-7.11, 1.34)$ m s^{-1} if the storm-relative winds are used, or $(x_t, y_t) = (-2.2, 2.5)$ km and $(u_t, v_t) = (-7.07, 1.49)$ m s^{-1} with earth-relative winds.

A technique for using the dropsonde and aircraft pressure-height data to find the track was also developed. This involves minimising the cost function

$$J(\boldsymbol{\beta}, \boldsymbol{a}) = \sum_{i=1}^{n_{\text{obs}}} \frac{(p_i - p_{\text{Hol}}(r(\boldsymbol{x}_i, t_i; \boldsymbol{a}); \boldsymbol{\beta}))^2}{\sigma_{pi}^2} \qquad \textbf{(4.2)}$$

Here $\boldsymbol{\beta} = (v_m, r_m, b, p_c)$ defines the shape and intensity of the Holland (1980) parametric profile p_{Hol} given by

$$p_{\text{Hol}}(r; \boldsymbol{\beta}) = p_c \left(1 + \frac{v_m^2}{bR_d T_v - v_m^2} \exp\left(1 - \left(\frac{r_m}{r} \right)^b \right) \right) \qquad \textbf{(4.3)}$$

This reduces to Holland's familiar form where v_m is the maximum cyclostrophic wind at radius r_m, p_c is the central pressure, b is Holland's profile shape parameter, and the gas constant R_d and virtual temperature T_v are used to evaluate the density at r_m. It is written

in terms of the maximum wind, rather than the usual central pressure deficit form, to facilitate comparison with other parametric profiles. Finally, $\boldsymbol{a}$ defines the linear track as above, r gives the distance of the observation from the track, and σ_{pi}^2 is the estimated error variance of the i-th observation. This is minimised over the control variable ($\boldsymbol{\beta}$, $\boldsymbol{a}$). J is differentiable with respect to ($\boldsymbol{\beta}$, $\boldsymbol{a}$), and so the Levenberg-Marquadt algorithm (Press et al. 1992 section 15.5), which converges much more rapidly than the simplex method, was used for the minimisation. This requires the derivatives of (4.3) with respect to the control vector, which are given, together with a derivation of (4.3), in Appendix 4.A1. This method will be called the translating-pressure-fit method.

Figure 4.6 illustrates the performance of this method, as applied to the dropsonde splash surface pressure observations. For clarity of illustration, an example with a small amount of data was chosen. The left panel shows the pressure observations plotted as a function of radius relative to the NHC track. It is apparent that there is a large amount of scatter between observations, especially in the region of maximum pressure gradient. The track determined from these observations is $(x_t, y_t) = (-1.8, 9.0)$ km and $(u_t, v_t) = (-7.04, 1.35)$ m s^{-1} and they are plotted against radius, relative to that track, in the right panel. It can be seen that the fitted track has the effect of making the observations lie much closer to a single curve. The impact of radial mis-location of observations will clearly be largest at the radius of maximum radial pressure gradient.

If flight-level data are used, then the track was found by this method to be given by $(x_t, y_t) = (0.2, 9.7)$ km and $(u_t, v_t) = (-7.05, 1.31)$ m s^{-1}, which is very close to that found using the flight-level storm-relative winds. Comparing this to the track found using the dropsonde surface pressures, there is vortex tilt between the flight level (approximately 4.5 km) and the surface, which varies from $(-2.0, -0.9)$ km at the

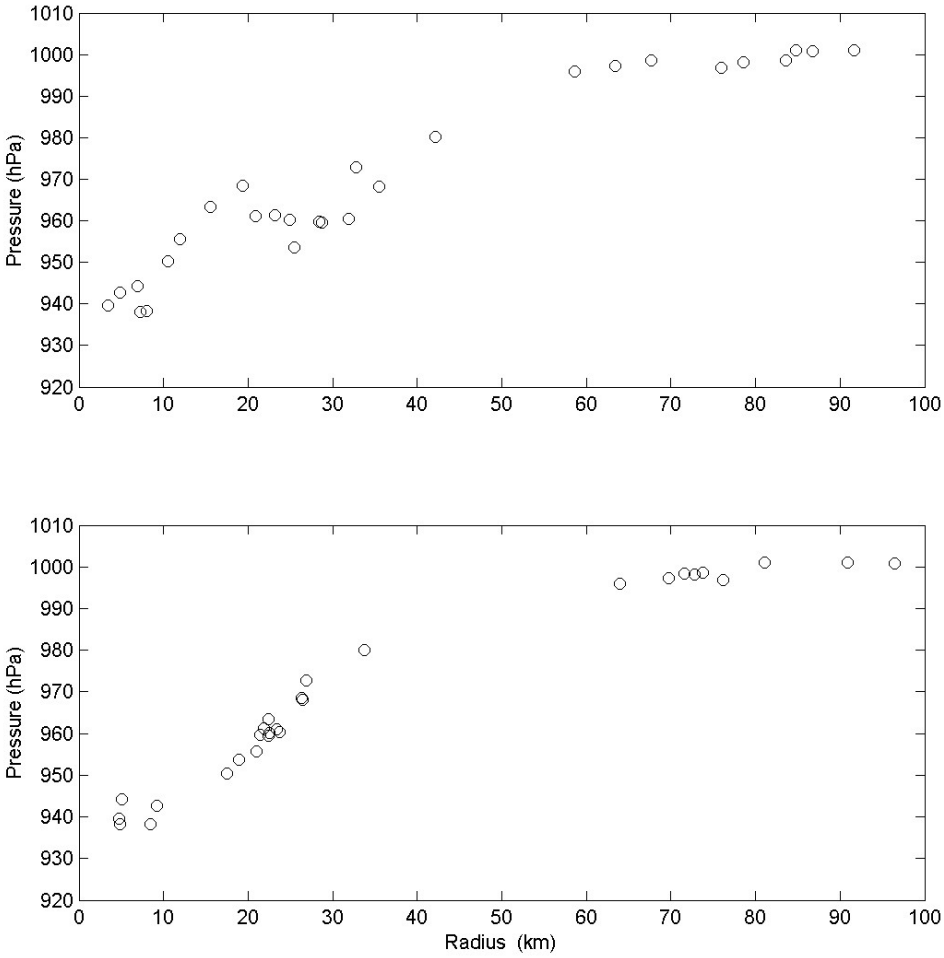

Figure 4.6 Dropsonde splash surface pressures in the core of Hurricane Georges, as a function of radius. Top: radius relative to the NHC best track. Bottom: radius relative to the track determined from the pressure observations by the translating-pressure-fit method as described in the text.

beginning of the observing period to (−1.9, −0.2) km at the end, with the surface centre to the WSW of the flight-level centre[1]. This tilt appears to be real and not an artifact of the data. The surface pressure gradient at the RMW of Georges is about 2 hPa km^{-1}, so ignoring a 2-km displacement leads to a 4 hPa amplitude, azimuthal wave-number one, asymmetry in the surface pressure field. This is readily apparent if a suitable parametric pressure profile (such as Holland's) is fitted to the observations located relative to track based on flight-level pressure data, and the residuals from the fit plotted against azimuth.

A similar minimisation was tried using a cost function based on the Holland gradient-wind parametric profile,

$$J_{vH}(\boldsymbol{\beta},\ \boldsymbol{a}) = \sum_{i=1}^{n_{\text{obs}}} \frac{(v_{\text{az}}(\boldsymbol{u}_i,\ \boldsymbol{x}_i,\ t_i;\ \boldsymbol{a}) - v_{\text{Hol}}(r(\boldsymbol{x}_i,\ t_i;\ \boldsymbol{a});\ \boldsymbol{\beta}))^2}{\sigma_{vi}^2} \qquad \textbf{(4.4)}$$

where

$$v_{Hol}(r;\ \boldsymbol{\beta}) = -\frac{fr}{2} + \sqrt{v_m^2 \exp\left(1 - \left(\frac{r_m}{r}\right)^b\right)\left(\frac{r_m}{r}\right)^b + \left(\frac{fr}{2}\right)^2} \qquad \textbf{(4.5)}$$

and σ_{vi}^2 is the estimated error variance of the i-th wind observation. A modification of Levenberg-Marquadt which took account of the dependence of v_{az} (the "observation") on the control variable $\boldsymbol{a}$ was developed to minimise this and is described in Appendix 4.A3. When this worked, the track was very similar to that found by the Marks-

[1] Care was taken to use the actual time of observation, not of dropsonde release. This was necessary since fall durations were around 400 s, during which the hurricane moved some 3 km.

circulation method. However, the iteration occasionally produced results which were clearly wrong. This appears to be because the Holland profile has a rather broader peak at the RMW than the observations, and thus gave an inherently less good fit, in combination with the fact that fitting eight parameters with around twenty to thirty observations meant that the fit was not well constrained and occasionally diverged or ended up in a spurious local minimum.

Similar techniques were tried using the Willoughby (2002) parametric profiles in place of Holland's. The performance with pressure was indistinguishable, while the performance with wind was better than Holland due to the more realistic profile shape near the RMW. However, this profile requires more parameters to be fitted than Holland's, and is computationally more expensive in its pressure form because the radial integration of the gradient-wind equation has to be done numerically. As the Holland pressure profile is adequate for finding the track, it was preferred.

The tracks of Georges as determined by the Marks-circulation and translating-pressure-fit methods applied to the flight-level data are shown in Fig 4.5, together with the various NHC and HRD tracks. The two linear tracks determined here are clearly in very good agreement with each other, and with the HRD low-resolution track. One indication of the value of the translating-pressure-fit track is that the range of radii at which the flight-level maximum wind occurs, when calculated from the various tracks, is least for the translating-pressure-fit track. Another advantage of it is that it represents an objective fit to data from the entire period, rather than being derived from aircraft "fixes" of the minimum wind, which are possibly affected by short-duration transient effects – indeed, the HRD high-resolution track shows evidence of a trochoidal track oscillation.

For the remainder of this analysis, the track obtained from the flight-level mass data by the translating-pressure-fit method will be used where track information is required. This is sufficiently accurate for the qualitative description of the wind field, and the analysis of the surface-wind factor. However, greater precision is needed for the analysis of gradient-wind balance and for that, the vortex tilts diagnosed above will be applied also.

4.2.3 The Wind Field

The dropsondes listed in Table 4.1 can be conveniently divided into three groups, those near the radius of maximum winds (at a radius of between 15 and 40 km), those in the eye (radius of less than 15 km), and those in the outer core (radius between 40 and 100 km). In this section, the measurements in each group are discussed, followed by an analysis of the surface-wind factor for the cyclone core as a whole.

4.2.3.1 The Winds Near the Radius of Maximum Winds

The measured wind speed profiles from the 16 eyewall sondes are shown in Fig 4.7, together with their storm-relative positions (when they passed through 1-km height), and their launch times. It is clear that there is substantial variation between individual profiles, both in the broad shape of the profile, and in the magnitude of the smaller-scale oscillations within the overall envelope. However, it is equally clear from the figure that a large part of the variation between profiles relates to their position within the storm.

The similarity between profiles that are close to each other (in a storm-relative sense) becomes more remarkable when one notes that these observations were taken over a period of over five hours. In particular, profiles N and O were taken almost 5 hours apart, A and P over 4 hours apart, and while I and J were separated by only 34

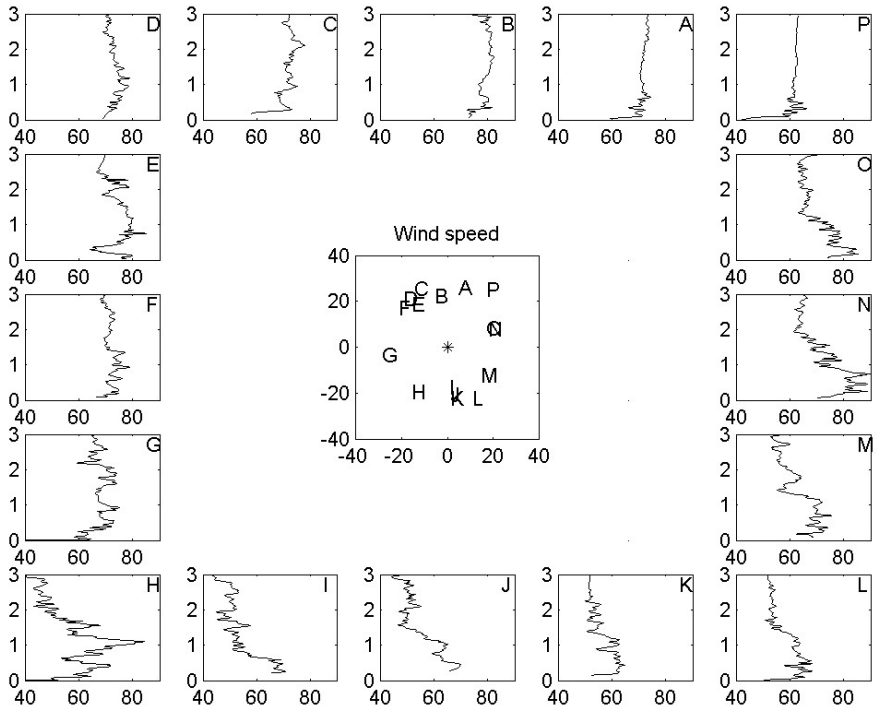

Figure 4.7 Profiles of earth-relative wind speed observed by dropsondes in and near the eyewall of Hurricane Georges. The position of the sonde as it fell through a height of 1 km is shown in the central panel. Further details of each profile may be found in Table 4.1.

seconds, K was half an hour later. It is thus reasonable to conclude that the variability in measured wind speed profiles depends largely on location within the storm.

The winds resolved into storm-relative cylindrical coordinates are shown in Figs 4.8 and 4.9. Most of the profiles do not show zero radial flow at the top of the profile, which may be because small errors in the track can cause significant errors in the resolution into storm-relative winds[2]. Nevertheless, there is some suggestion of systematic inflow to the south-east, and systematic outflow to the north-west, which may be related to the weak south-easterly shear which Knaff (2002) associated with his "annular hurricanes". Both of these factors complicate the interpretation of what, from the perspective of boundary-layer processes, is the "inflow" and "outflow". However, it seems that, starting from profiles A and moving anticlockwise, that there is a tendency for the boundary-layer inflow to become deeper and stronger towards the front of the storm, together with the formation of an outflow layer above, which persists around the rest of the storm. This outflow layer generally lies above the strongest azimuthal winds in the profile. The strongest near-surface inflow seems to occur in two patches, ahead of (profiles F and G) and behind (N, O) the storm.

The storm-relative azimuthal winds have a low-level maximum in all profiles, which is most marked to the south and east of the storm, where it is up to 20 m s^{-1} stronger than the winds in the upper part of the profile. It is least strong to the north. Profile E shows an additional maximum very near the surface, with lighter winds immediately aloft. This latter near-surface maximum is associated with increased inflow, relative to the lighter winds aloft.

[2]For instance, a 2-km position error for a purely azimuthal 75 m s^{-1} wind at a radius of 25 km can cause a spurious radial wind of up to 6 m s^{-1}.

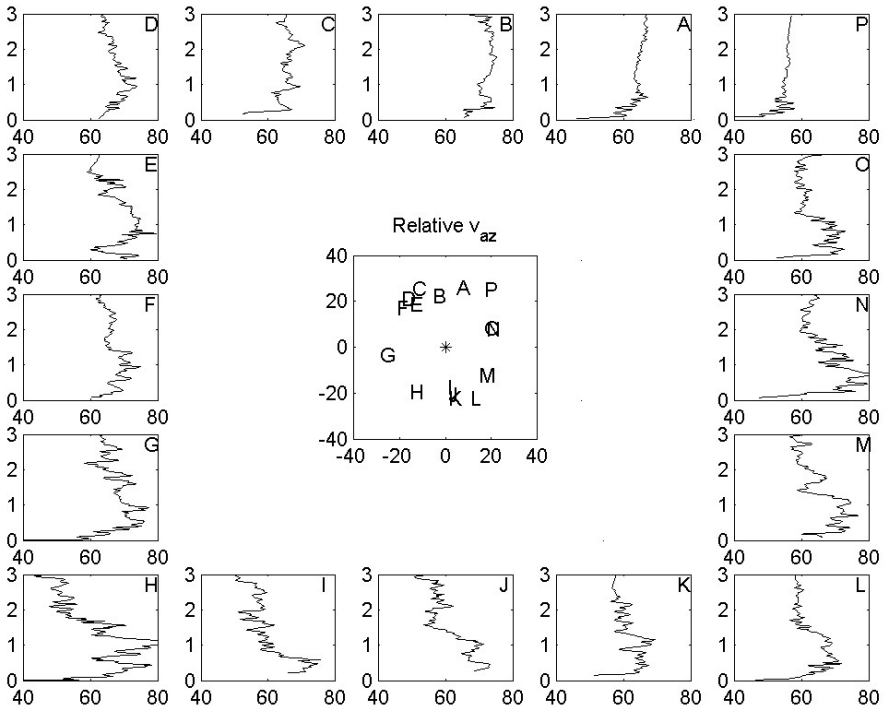

Figure 4.8 Same as Fig 4.6, except for the storm-relative azimuthal wind component.

Much of the smaller-scale structure in the profiles is presumably turbulence. In an effort to remove this, the profiles were averaged into 100 m layers, divided into four quadrants according to their position at a height of 1 km, and averaged. Averages over all 16 profiles were also calculated, and are all shown in Fig 4.9. Apart from the south-west quadrant, which is the average of only two relatively "noisy" profiles, the resulting mean profiles are reasonably smooth. Averaged around the storm, the near-surface inflow layer is 1.1 km deep, with a secondary inflow band above 2.2 km which is presumably forced by latent heat release in the eyewall (e.g. Willoughby 1995). Marked outflow is present only to the south-west, although it seems reasonable to interpret the zero radial component just above 1 km in the eastern quadrants as being boundary-layer forced outflow, relative to the thermally- and shear-forced inflow aloft. This interpretation fits in well with the earlier modelling work, and also with the heights of the azimuthal flow maxima in the various quadrants.

The average azimuthal wind over the whole storm shows a broad maximum between about 500 and 1200 m. The flow decreases rapidly in the first few hundred metres above this, then more slowly. This would be consistent with the maximum being supergradient, since gradient balance implies thermal balance, and thus fairly constant shear above the boundary-layer (unless the radial temperature gradient is greater immediately above the maximum than further aloft, which would be unlikely). However, since the size of the relatively sudden decrease immediately above the maximum, is less than the standard deviation of the differences between profiles, if is difficult to be confident that the change in slope is real. The gradient-wind balance will be analysed in detail below.

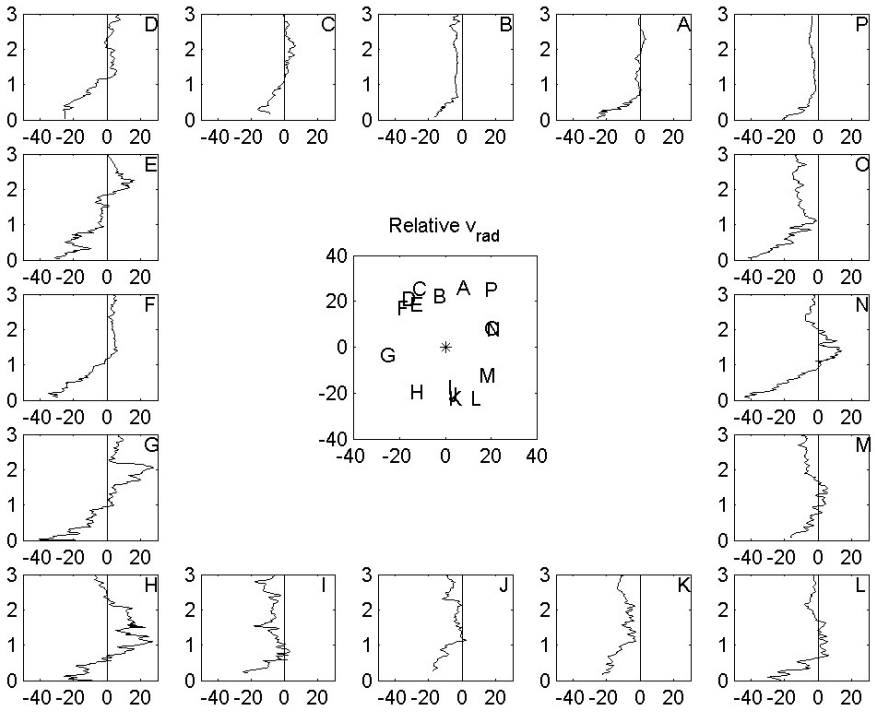

Figure 4.9 Same as Fig 4.6, except for the storm-relative radial wind component

Mean profiles stratified by radius, are shown in Fig 4.11. It is clear that the inner annulus (15- to 25-km radius) has a lower and more marked azimuthal maximum, stronger near-surface winds, and slightly shallower inflow, than the 25-35 km annulus. All three characteristics are in agreement with the analytical and numerical modelling work described in earlier chapters.

4.2.3.2 The Winds in the Eye

Five dropsondes were deployed in the eye during the period in question. The profiles of wind speed, and storm-relative components, are shown in Fig 4.12. The azimuthal wind is from 10 to 20 m s^{-1} at the surface, and either decreases or remains roughly constant with height. The radial flow measurements show neither systematic variation nor consistency from profile to profile. It is possible that the measurements here may be dominated by some small-scale, vertically coherent, but transient feature, such as an eyewall meso-vortex (eg Schubert et al.1999).

4.2.3.3 The Winds in the Outer Core

The profiles of wind speed for the ten dropsondes at radii between 50 and 100 km are shown in Fig 4.13. There is no readily apparent wind speed maximum to the rear of the storm (profiles d, e), but it is quite marked to the north (profiles V, W, X) and becomes less prominent but closer to the surface, cyclonically around the storm to the south. The exception to this trend is profile Y, which has its maximum speed very near the surface.

Averages of the storm-relative wind components for each quadrant, and overall, in the annulus between 50- and 100-km radius, are shown in Fig 4.14. The overall mean shows an inflow layer a little over 1 km deep, with a suggestion of weak outflow centred

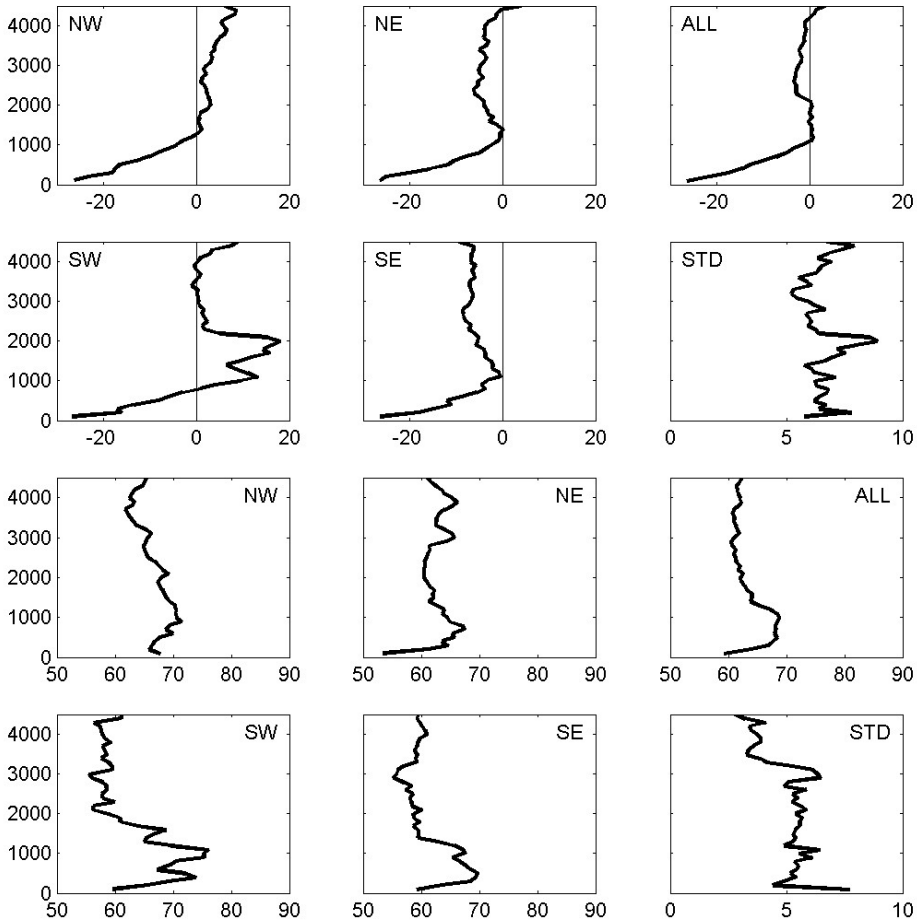

Figure 4.10 Mean profiles of radial (top 6 panels) and azimuthal (lower 6) storm-relative wind, from dropsondes between 15- and 40-km radius. Each group of six panels contains averages over the four quadrants, and the whole annulus, as labelled. The panel labelled STD shows the standard deviation for the whole annulus.

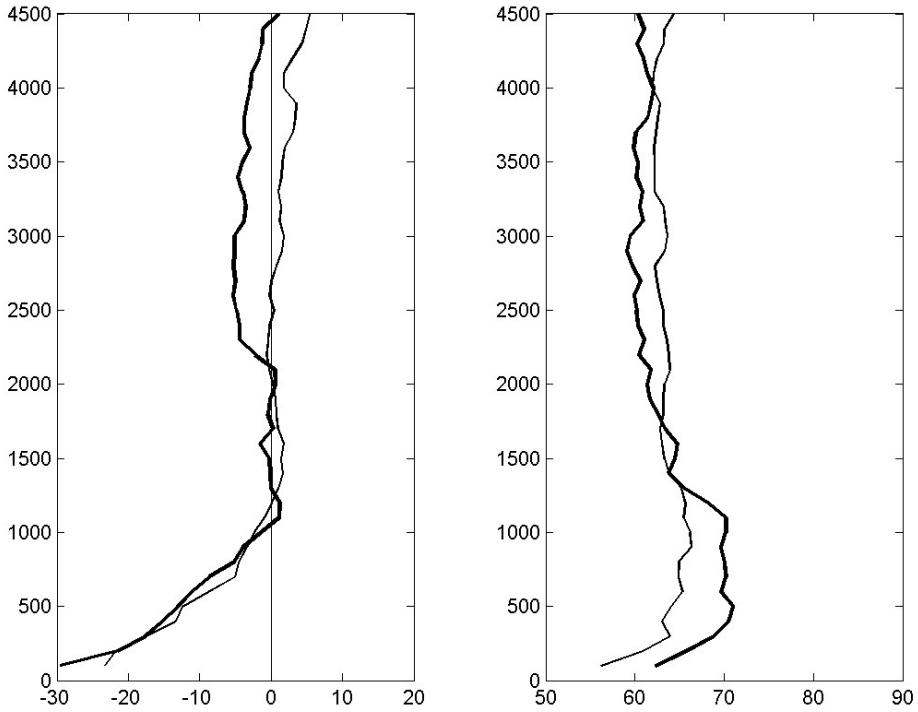

Figure 4.11 Mean storm-relative radial (left) and azimuthal (right) wind, for the radii between 15 and 25 km (heavy) and between 25 and 40 km (light).

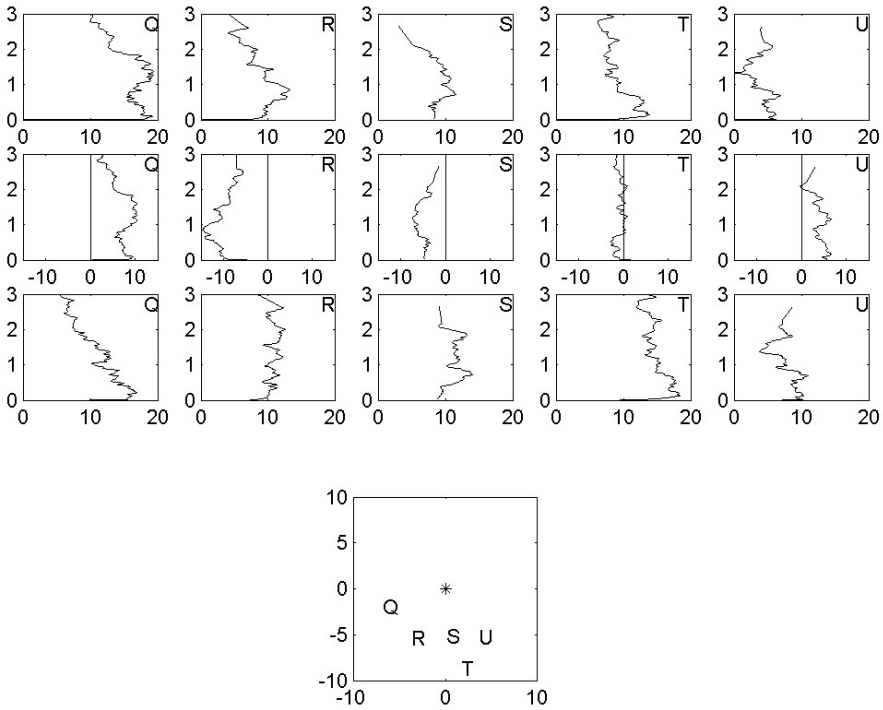

Figure 4.12 Dropsonde observations of wind speed (top) and storm-relative radial (middle) and azimuthal (bottom) wind, for observations in the eye. The positions shown are those as the sonde passed through 1-km height.

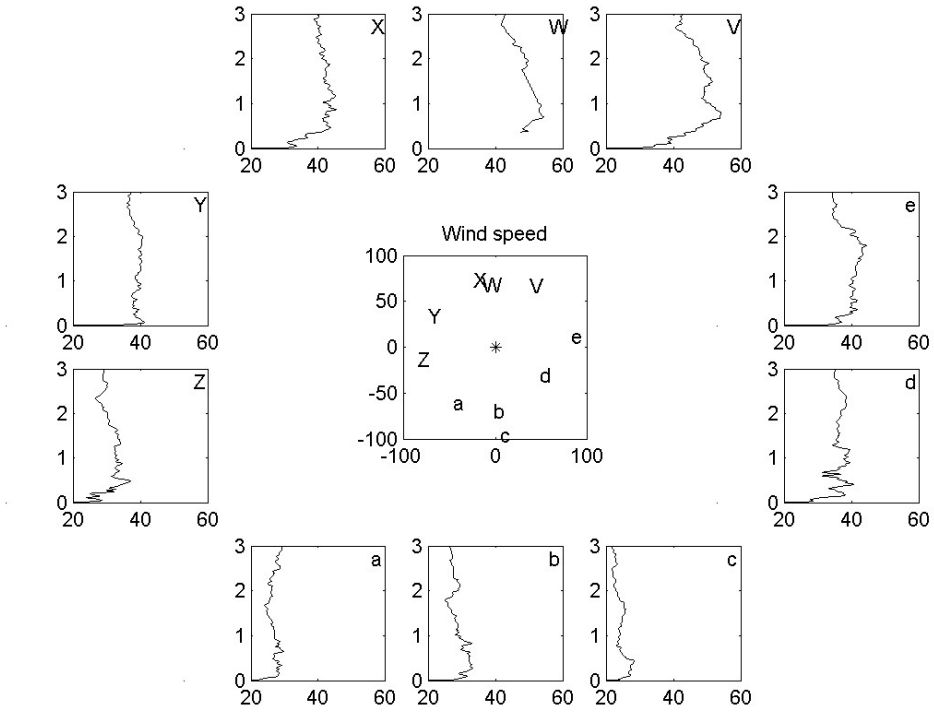

Figure 4.13 Dropsonde observations of wind speed, for observations at radii between 40 and 100 km. The positions shown are those as the sonde passed through 1-km height.

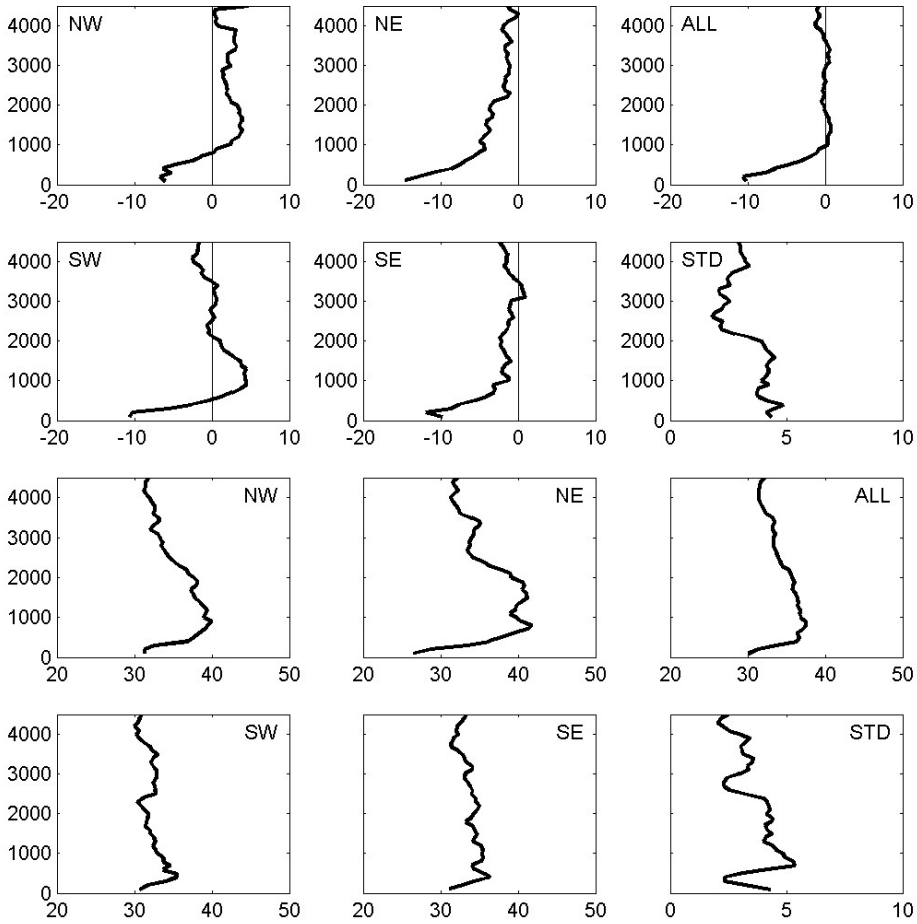

Figure 4.14 The same as Fig 4.9, except for observations between 40- and 100-km radius.

near 1.5 km. The maximum mean azimuthal wind is near the top of the inflow layer at 800 m. This maximum is broader and stronger to the north of the storm than to the south, where it is comparatively weaker, narrow and closer to the surface. The inflow is deepest to the north-east, and the storm-relative outflow strongest, at about 5 m s^{-1}, in the two western quadrants, where it largely lies above the azimuthal wind maximum.

4.2.3.4 Surface-Wind Factor

The ratios of the earth-relative wind speed at 50 m, to that at 1500 m and 2500 m, were calculated from the wind observations. The height of 50 m for the "near-surface" wind was chosen as many of the sondes failed in the lowest few tens of metres, and there was insufficient remaining data for an analysis. The latter two heights were chosen as representative of typical reconnaissance flight levels. Note that these represent "slant" wind reduction factors, following the dropsonde path, which rotates roughly 60° in azimuth in falling from 3 km to the surface in the near-eyewall drops.

The observed ratios were located at the sonde's 50-m position and analysed by a standard univariate statistical interpolation (SI) scheme (see for example Lorenc 1981, Daley 1991 chapter 4). The resulting analyses are shown in Fig 4.15. The background field for these was set to be uniform at 0.8, which is close to the climatological value, with the background error standard deviation taken as 0.1, which is representative of the variability of the ratio in Powell and Black (1990). The background error correlation between points (r_1,λ_1) and (r_2,λ_2) was assumed to be given by a Gaussian function in polar coordinates,

$$C(r_1,\lambda_1,\ r_2,\lambda_2) = \exp\left(- \frac{(r_1 - r_2)^2}{2L_r^2} - \frac{(\lambda_1 - \lambda_2)^2}{2L_{az}^2} \right) \qquad \textbf{(4.6)}$$

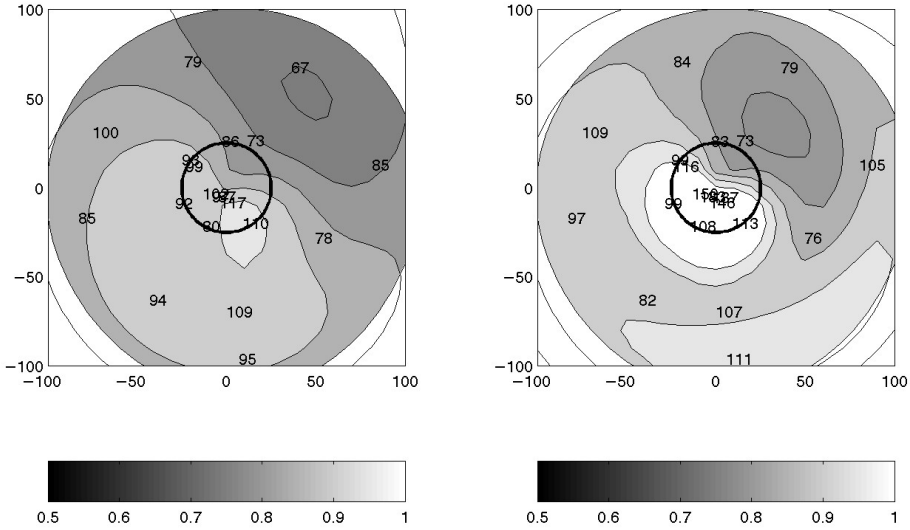

Figure 4.15 Analyses of wind reduction factors from 1500 m (left) and 2500 m (right), to 50 m. Contour interval is 0.05, the observations used in the analysis multiplied by 100 are also shown. The central black circle shows the approximate RMW. The shading between the contours is applied only where the estimated analysis-error is below 0.08.

with length scales L_r = 30 km and $L_{az} = \pi/3$. The observation errors were assumed to be independent with standard deviation also of 0.1, which is consistent with the individual wind measurements having total-error standard deviations of the order of 5%. The analysis-error covariance matrix was also calculated, and the analysis was deemed to be unreliable wherever the estimated analysis-error exceeded 0.08, and was not shaded. These blank areas correspond to data sparse regions. It should be noted that the analyses are moderately sensitive to the necessarily ad hoc assumptions about the background and observation error statistics. These were chosen, in the absence of much other information, as much to give an analysis that fitted the observations reasonably well as to satisfy some intuitively reasonable constraints on the error parameterizations; for example, that the radial length scale should be of the order of the radius of maximum winds. The observations are also plotted in the figure, and it can be seen that the analyses are in good agreement with them.

The resulting analyses of surface-wind factor from the two heights are in good agreement with the theoretical predictions. Both the increase towards the storm centre, and the left-right asymmetry, are clearly apparent, although the analysis resolution is insufficient (because of lack of observation density) to capture all the fine detail in the model calculation. Here, the maximum appears to lie towards the left-rear, rather than the left-front. This appears to be because the comparison here is between measured winds at two heights, rather than the gradient-wind and a near-surface wind; thus comparison with Fig 3.15 is most appropriate. An unexpected feature is the secondary maximum in the left rear quadrant at a radius of approximately 90 km. This maximum is defined by three observations, profiles b, c and e in Fig 4.13. While the latter of these is arguably unrepresentative as it shows a rapid decrease in wind speed above 2 km, the others have similar shapes. Moreover, they were taken some five hours apart and so it

appears this is not a transient feature. Rather, it seems to be associated with an outer convective ring which was apparent on radar imagery and strongest to the rear of the storm, for much of the observation period.

4.2.4 Analysis of Balance

Here, the dropsonde observations of the wind and mass fields will be analysed and the extent to which the azimuthal mean is in gradient balance will be diagnosed. However, it is necessary to begin by carefully considering the nature of the dropsonde data. Full details of the data processing are given by Hock and Franklin (1999); here only sufficient detail to understand the analysis issues is given.

The dropsondes measure pressure, temperature, humidity and position. The position data are used to calculate the wind, and the pressure and thermodynamic data are used to calculate the geopotential height by integrating the hydrostatic equation. The hydrostatic integration may be started from one of two points at which both the height and pressure are known. The first is to use the last reported pressure before the instrument hits the sea, the so-called "splash pressure"[3]. The height of this last observation is estimated from the telemetry signal, and is typically less than 10 m. Alternatively, the integration may begin from the aircraft's observed pressure and height (from the radar altimeter), and proceed downwards. This also provides an additional estimate of the surface pressure. In practise, the upwards integration is usually used except in cases where the dropsonde fails before impact.

[3]A small hydrostatic correction was applied to the last-reported pressures to bring them to the surface; this adjusted pressure will henceforth be called the "splash pressure".

Two important assumptions underlie these calculations: firstly, that the atmosphere is in hydrostatic balance, and secondly, that the dropsonde path is vertical. The first cannot be corrected for if false, and will be assumed to be true.

The second assumption, that the dropsonde path is vertical, is quite definitely untrue. The eyewall dropsondes in Hurricane Georges typically rotated about 60^{o} in azimuth as they fell, as well as having an inwards displacement of up to about 3 km, the bulk of which typically occurred in the lowest 500 metres or so of the dropsonde trajectory. This radial displacement will introduce a marked systematic difference between the upwards and downwards hydrostatic integrations, since a maximum wind of 65 m s^{-1} at a radius of 25 km corresponds to a surface pressure gradient of approximately 1.8 hPa km^{-1}. This difference was found to cause problems in analysing the pressure gradient if a mix of upwards and downwards profiles are used, as the "upwards" profiles had systematically lower pressures at any given height, than the "downwards" profiles, due to their hydrostatic "anchor point" being closer to the centre of the storm.

A related issue is that of the radius at which the calculated pressure-height data should be regarded as applying. For instance, assume all sondes experience an inwards displacement of 1/10 of the RMW in the lowest kilometre of their fall, that there is no horizontal virtual temperature gradient, and that all the integrations are upwards. If the calculated pressures at heights above 1 km were applied at the radius of the sonde as it passed through that height, this is equivalent to displacing the surface pressure gradient field outwards by one tenth of the RMW. At the RMW, the calculated cyclostrophic wind will therefore be biassed high by $1.1^{1/2}$ or approximately 5%, which is significant in the context of this analysis. Thus, it is necessary to apply the derived pressure-height

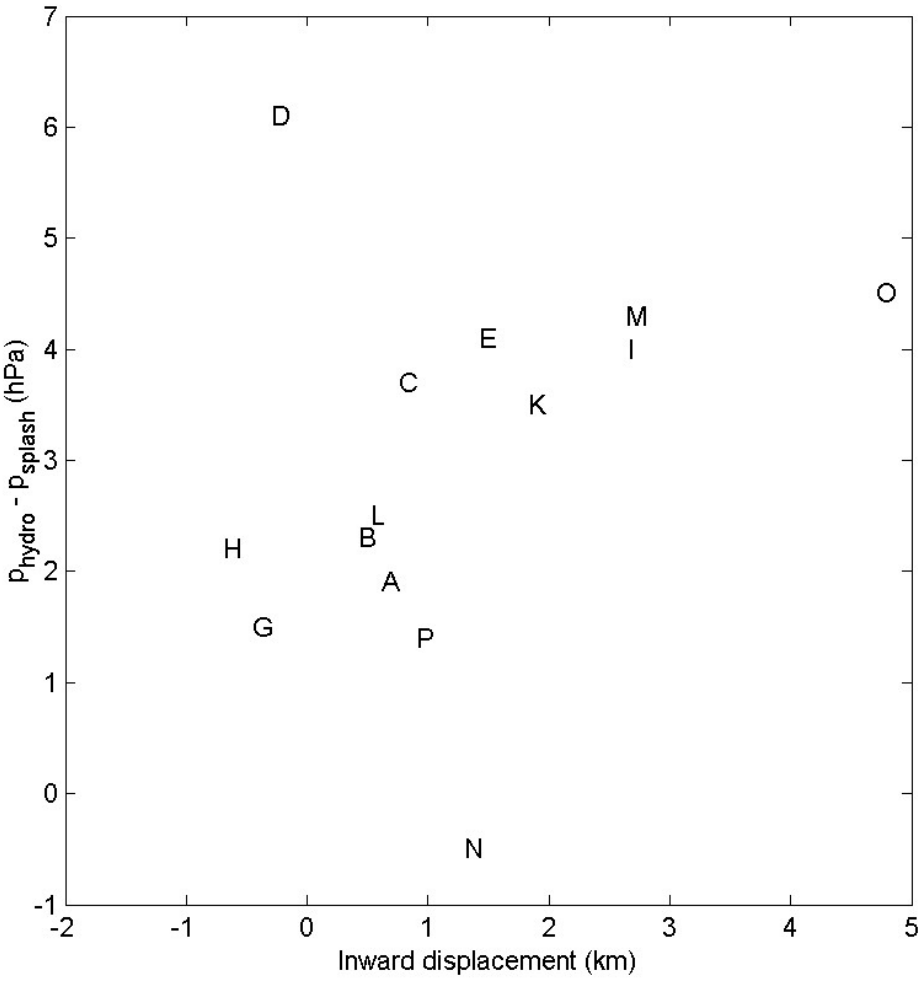

Figure 4.16 Scatter plot of difference between hydrostatic and splash surface pressure, and inwards displacement of the dropsonde trajectory, for near-eyewall sondes in Hurricane Georges.

data at the radius of whichever hydrostatic anchor point was used.

The effect of radial displacement shows up in the difference between the surface pressure calculated by integrating the hydrostatic equation downwards from the aircraft along the dropsonde trajectory, and the splash pressure. Figure 4.16 is a scatter plot of this difference against the radial displacement of all the near-eyewall sondes, and the relationship is clear, as is the fact that the difference is almost always the same sign. Sondes D and N are outliers from this trend; the latter possibly because the relative humidity measurements[4] were too high, while the former was at a larger radius than either its release or splash radius for most of its fall, and so may have experienced unrepresentatively cold temperatures, biassing its hydrostatic surface pressure high. There is also an offset of 1 – 2 hPa at zero radial displacement, which can be significantly reduced by correcting the aircraft altitude to a geopotential[5].

A further correction is made to account for the radial temperature gradient. The cyclone is warm-cored, thus the temperatures immediately above the splash point will be higher than those experienced by the falling sonde. To correct for this, the measured virtual temperatures were located relative to the storm, and the radial temperature gradient estimated by fitting straight lines. This was carried out separately for the measurements near the RMW (i.e. those between 15- and 40-km radius) and those in the outer core (between 50- and 100-km radius). It was also found to be necessary to treat separately those from the two observing periods, since the warm core strengthened

[4]Based on comments by the mission scientist, contained in the data file.

[5]The gravitational acceleration at 15°N of g = 9.7838 m s^{-2}, compared to the standard 9.80665 m s^{-2}, makes an effective difference of about 10 m in the release height.

slightly between the flights, and the radial temperature gradient in the outer core reversed. An example of the analysis, together with the radial temperature gradients so found, is shown in Fig 4.17, and it can be seen that the linear fits adequately describe the radial temperature variation. The reversed radial temperature gradient in the later set of observations may be due to evaporative cooling, since the radar imagery (Figs 4.3 and 4.4) shows a marked increase in stratiform rain between the two flights. A similar increase in rain can be inferred from the changes in the 85 GHz SSM/I imagery from overpasses at 1049 and 2355 UTC on September 19 (not shown). The change in radial temperature gradient was not apparent in the aircraft temperature observations, at approximately 4.5 km altitude.

These estimated radial virtual temperature gradients were used to linearly adjust the dropsonde observations to the hydrostatic anchor radius. The hydrostatic equation was then integrated to give the corrected pressure-height relationship in that vertical column. The integration was carried out in both upwards and downwards where the data coverage permitted, and it was found that this procedure largely eliminated the correlation between the radial displacement and the difference between the two surface pressure estimates (i.e. downwards hydrostatic integration, and splash) previously noted.

The amount of data available is not large, and it is also very unevenly distributed radially. Thus it was decided to fit the Willoughby (2002) parametric profile to the data, rather than analysing them to some grid. The Willoughby profile was designed specifically to accurately fit aircraft wind observations. Here, it is used both in its original form (i.e., as a wind profile), and as the equivalent radial pressure profile found by radially integrating the gradient-wind equation. The profile (in either form) is fit to the observations using the Levenberg-Marquadt method (Press et al. 1992, section 15.5).

The derivatives with respect to the control variable were found as described in appendix 4.A2. The equation that was minimised was

$$J(\boldsymbol{a}) = \sum_{i=1}^{n_{obs}} \frac{(p_i - p_w(r_i; \boldsymbol{a}))^2}{\sigma_p^2 + (\sigma_r \, \partial p_w/\partial r)^2} \qquad \textbf{(4.7)}$$

where p_i is the i-th pressure observation at radius r_i, p_w is the pressure form of the Willoughby parametric profile, $\boldsymbol{a}$ is the vector of parameters for p_w, σ_p = 1 hPa is the estimated standard deviation of the pressure observation error, σ_r = 1 km is the estimated standard deviation of the position error (including track uncertainties) and n_{obs} is the number of observations. The choice of σ_p = 1 hPa is rather larger than Hock and Franklin (1999) suggest, but the residual differences between the upwards and downwards integrations, the need to include errors of representation, and the uncertainty in the splash pressure due to the wavy nature of the sea surface, support this choice. The components of the control vector are $\boldsymbol{a} = (v_{m1}, L_1, v_{m2}, L_2, r_m, n_1, p_c, T_v, L_b)$, where v_{m1} and L_1 (v_{m2} and L_2) give the amplitude and length scale of the first (second) exponential, r_m is the radius of maximum winds, n_1 the shape parameter for the winds in the eye, p_c the central pressure, T_v the mean virtual temperature, and L_b the blending zone half-width. Note that the effects of observational error in both pressure and location are included. While the errors in the dropsonde location are negligible for this purpose, the track is not as accurately known, so it is appropriate to allow for this in the fit. Including this component of error leads to a slightly greater gradient in the fitted pressure profile near the RMW than if it is omitted, as shown in Appendix 4.A3.

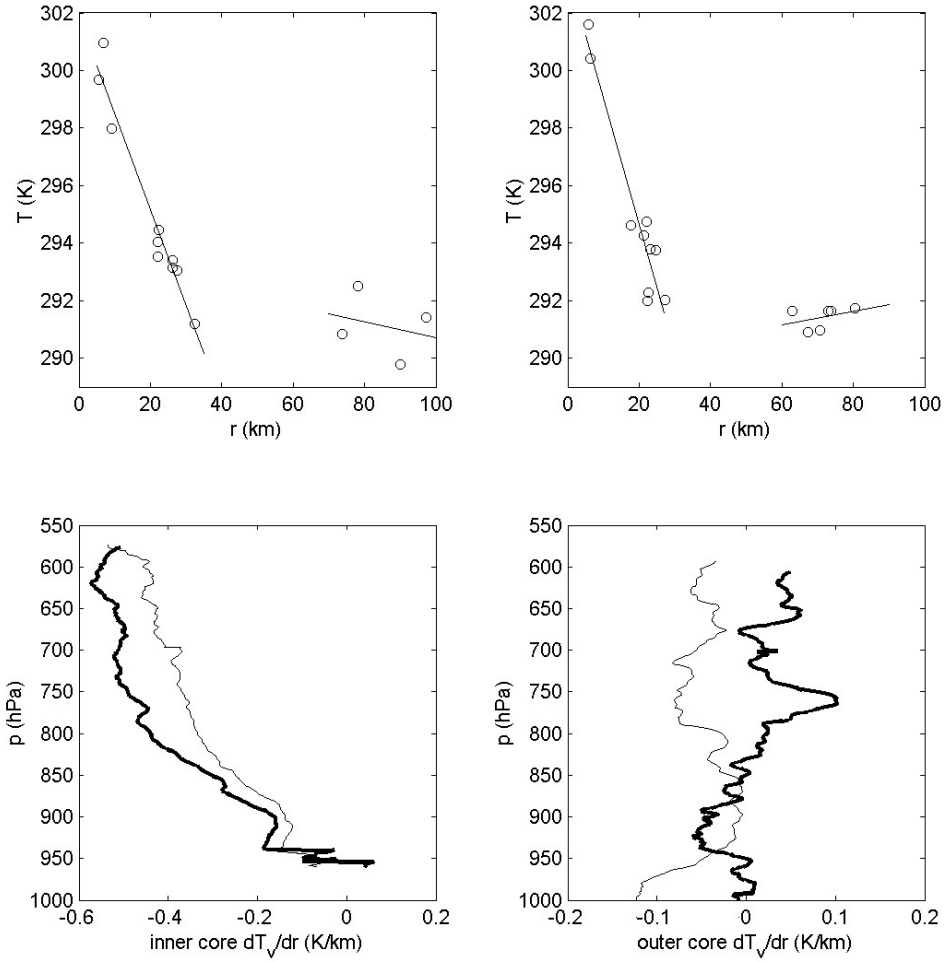

Figure 4.17 Top: Dropsonde observations of T_v at 800 hPa as a function of radius in Hurricane Georges for the early (left) and late (right) periods, together with fitted lines as described in the text. Bottom: Estimated radial virtual temperature gradient for the early (light lines) and late (heavy) periods, in the inner (left) and outer (right) core regions.

4.2.4.1 Gradient-Wind Equation I: Pressure Analysis

In this section, the pressure-height data derived above are used to estimate a radial pressure profile at a range of heights. This is differentiated and used to calculate the gradient-wind speed. The storm motion is subtracted from the wind observations, which are then resolved into azimuthal and radial components. The storm-relative azimuthal winds are then compared to the calculated gradient winds. The track found by the translating-pressure-fit method and discussed earlier, including the vortex tilt, is used for these coordinate transformations.

The initial approach was to combine the observations from both periods. However, this produced incorrect results since there were small changes in the cyclone structure between the two observation periods. An example of the problems that arise is given in Fig 4.18, which shows the results for a height of 1 km. The pressure profile clearly fits the observations well. Moreover, analysis of the residuals shows that both the 15-40 km and 50-100 km bands are uncorrelated with radius; that is, that the gradients in these bands are accurately estimated, and the numerical fitting procedure has worked properly. The lack of correlation in the residuals, considered as a whole, can also be seen by examining the lower panel of Fig 4.18. However, it is also clear that the pressures near the RMW rose between the early and late periods, as the RMW contracted, and that the residuals from each period, when considered separately, are correlated with radius. That is, the fitted curve underestimates the radial pressure gradient in both periods. It is also clear from the figure that a similar problem arises with the outer core observations. Thus the apparent supergradient flow in both regions is spurious, and it is necessary to consider the periods separately.

The pressure profile was then fit to just the observations from the first observing

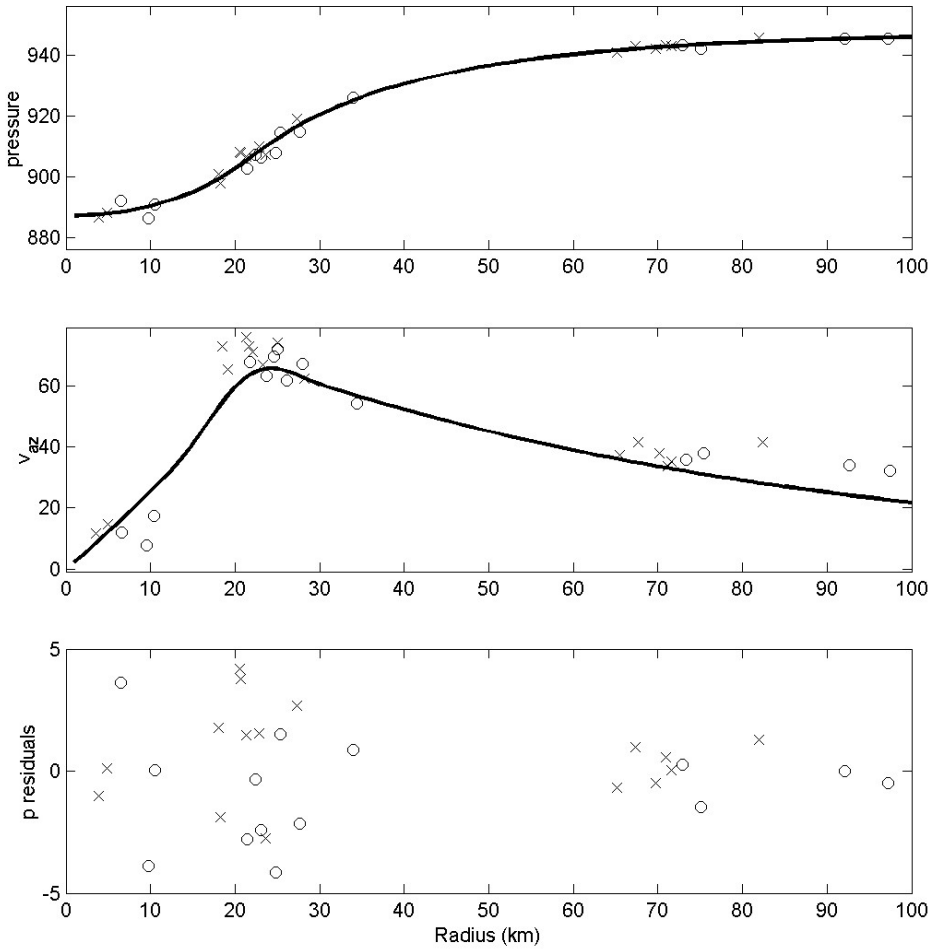

Figure 4.18 Top: Observations of pressure from the early (o) and late (x) periods, at a height of 500 m in Hurricane Georges, together with the best fit Willoughby radial pressure profile. Middle: Observations of storm-relative azimuthal wind from the early (o) and late (x) periods, together with the gradient-wind speed calculated from the fitted pressure curve. Bottom: Differences between the observed and fitted pressures.

period. It turned out to be impractical to fit all the parameters, as the Hessian matrix in the iteration became singular. The problems were particularly severe with the second length scale L_2, and the blending half-width L_b. These were accordingly held fixed at 400 km and 9 km, respectively, which were found to be suitable values from fitting the profile to the flight-level data. Occasional problems with matrix ill-conditioning during the iteration were solved by the use, when necessary, of singular-value decomposition rather than Q-R decomposition for the linear system solution, as discussed in Appendix 4.A3. In addition, the reasonable constraints that $L_1 > L_b$, and $1 < n_1 < 2$, were applied. These fits were carried out every 100 m from the surface to 2.5 km.

The observations or pressure and wind at 500 m, 1 km and 2 km, together with the fitted pressure profiles and the corresponding gradient-wind profiles, are shown in fig 4.19. At all levels, the storm-relative azimuthal wind observations in the vicinity of the RMW are typically a few m s^{-1} less than the estimated gradient-wind speed. This is an unexpected result which is discussed further below. The apparent supergradient flow in the outer core is believed to be spurious, since with only four observations, widely spaced in azimuth, any small asymmetries in the storm would result in an inaccurate estimate of the azimuthal-mean pressure gradient there.

The vertical profiles of the fitted maximum gradient-wind, and its radius, together with the fitted value of the cost function, are shown in Fig 4.20. It can be seen that there is good vertical consistency, and that the maximum gradient-wind slowly decreases with height, while its radius increases, as would be expected. The general decrease with height of the cost function implies that the observations fit the profile better, further away from the surface. Lorenc (1986) discusses two sources of

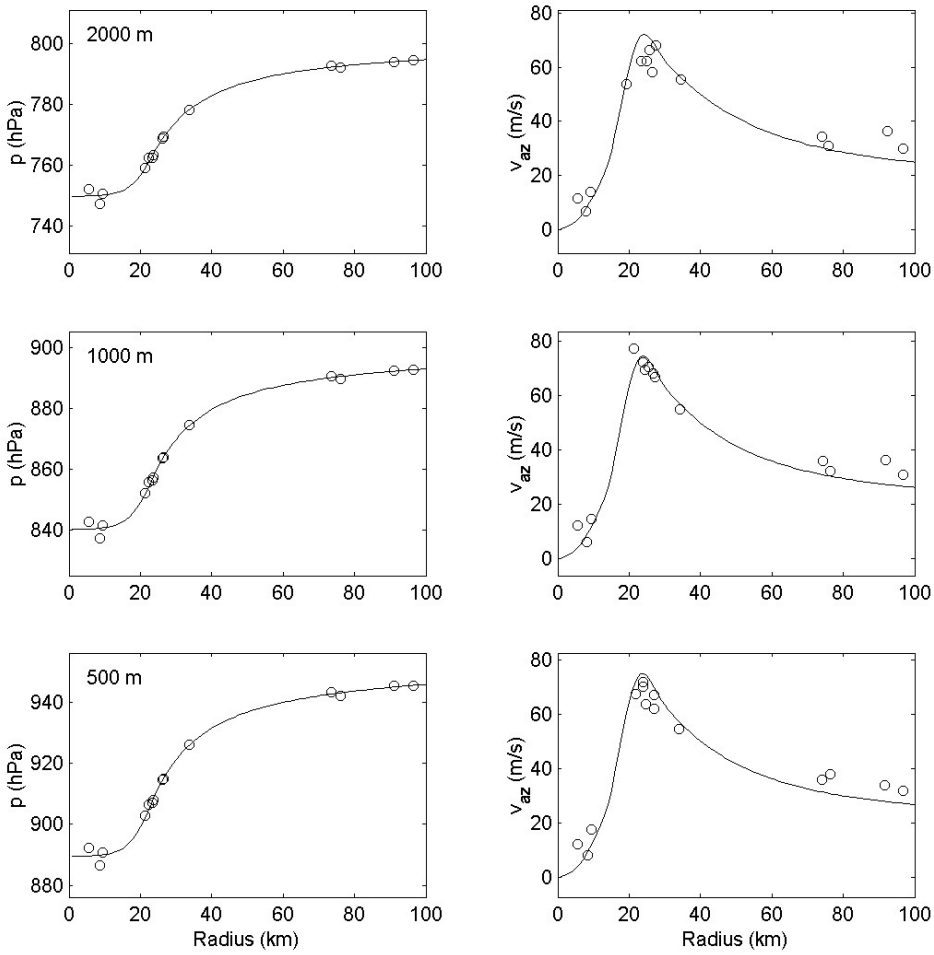

Figure 4.19 Left panels: Observations of pressure at 2 km (top), 1 km (middle) and 500 m (bottom), together with fitted curves, for the early period. Right: Observations of storm-relative azimuthal wind, together with the gradient-wind speed, at the same heights.

observational error relevant to objective analysis: instrumental, and representational. The latter arises from phenomena on scales which are unresolved by the analysis. All except one of the pressure-height profiles used were integrated upwards from the surface, so it seems unlikely that "instrument" (here including the hydrostatic integration) error decreases with height. It is unclear whether the decrease with height is because the representational errors are larger near the surface, or because this component of the error is proportional to the pressure, as would occur if the unresolved features were approximately balanced, and of roughly constant velocity amplitude with height.

An identical similar procedure was applied to data from the second period. The fitted parameters are summarised in Fig 4.22, and it can be seen that there is both good vertical consistency, and that the results are physically reasonable in that v_m decreases, and r_m increases, with height. The flow near the RMW is is now found to be indistinguishable from gradient balance above 400 m. The gradient and observed wind are compared in Fig 4.21, for the same three representative levels as before. The outer core winds are closer to gradient balance than found in the earlier case, which seems to be due to the greater amount of data giving a more reliable estimate of the radial pressure gradient there, in this case.

Note that J/n_f is close to constant with height in the late period, and smaller than in the early period. It appears that the hypothesised unresolved low-level features of the early period, are now weaker or absent. It is interesting to note in this context that the eye shape parameter n_1 has also decreased, reducing the barotropic instability of the inner edge of the RMW. Thus the tendency to generate eyewall meso-vortices has decreased (Schubert et al. 1999).

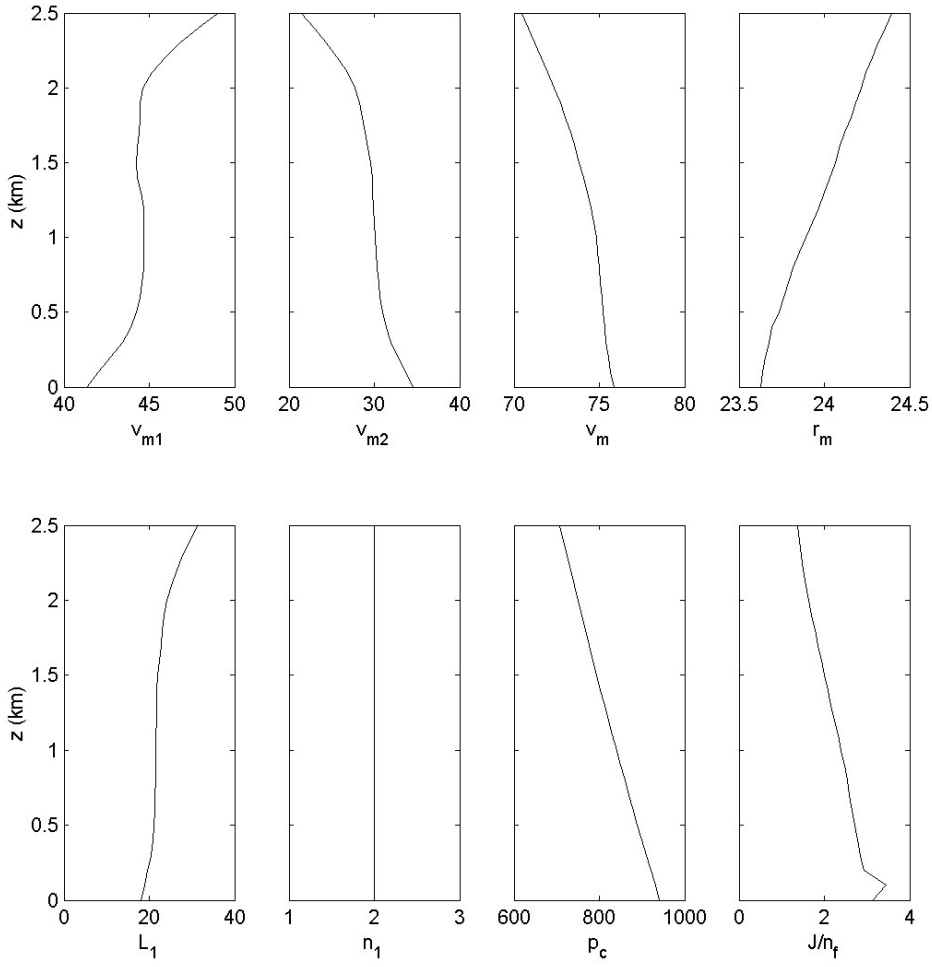

Figure 4.20 Fitted parameters in the Willoughby parametric profile, for pressure fits to the early data. From top left: the velocity scale of the first outer profile, the velocity scale of the second outer profile, the maximum wind, the radius of maximum winds, the length scale of the first outer exponential, the eye shape parameter, the central pressure, and the goodness-of-fit J divided by the number of degrees of freedom.

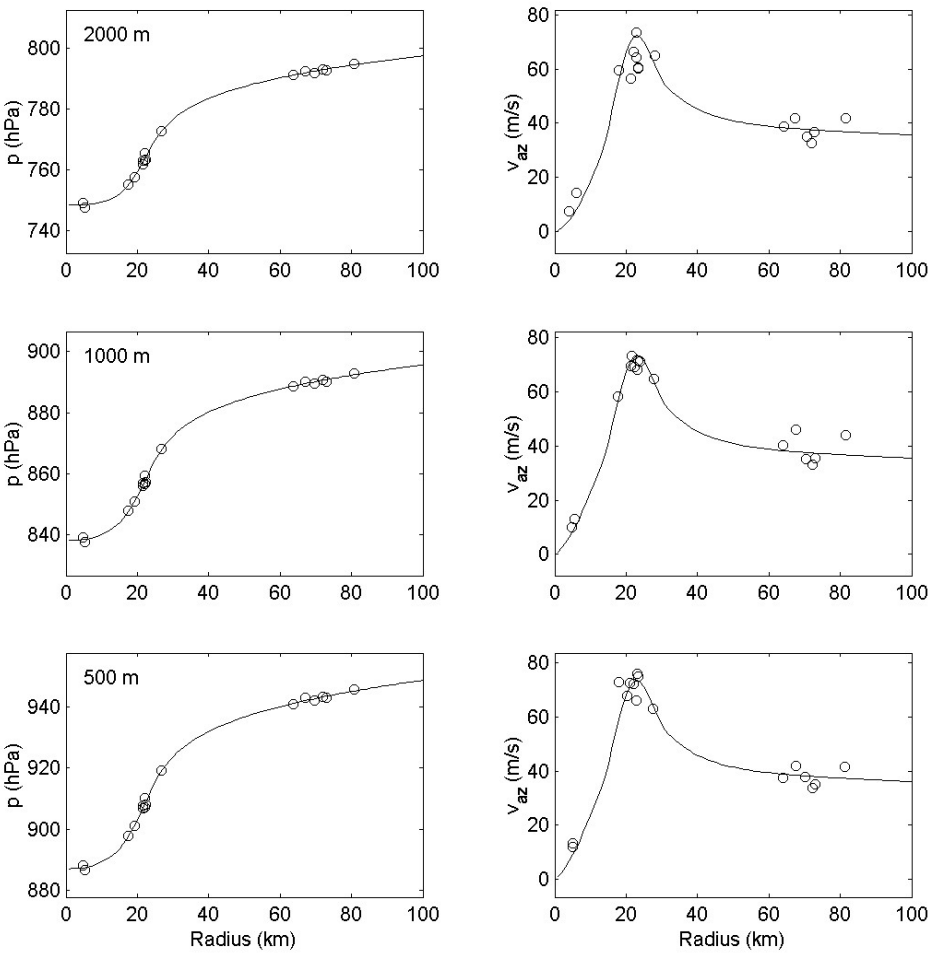

Figure 4.21 Same as Fig 4.19, but for the late period.

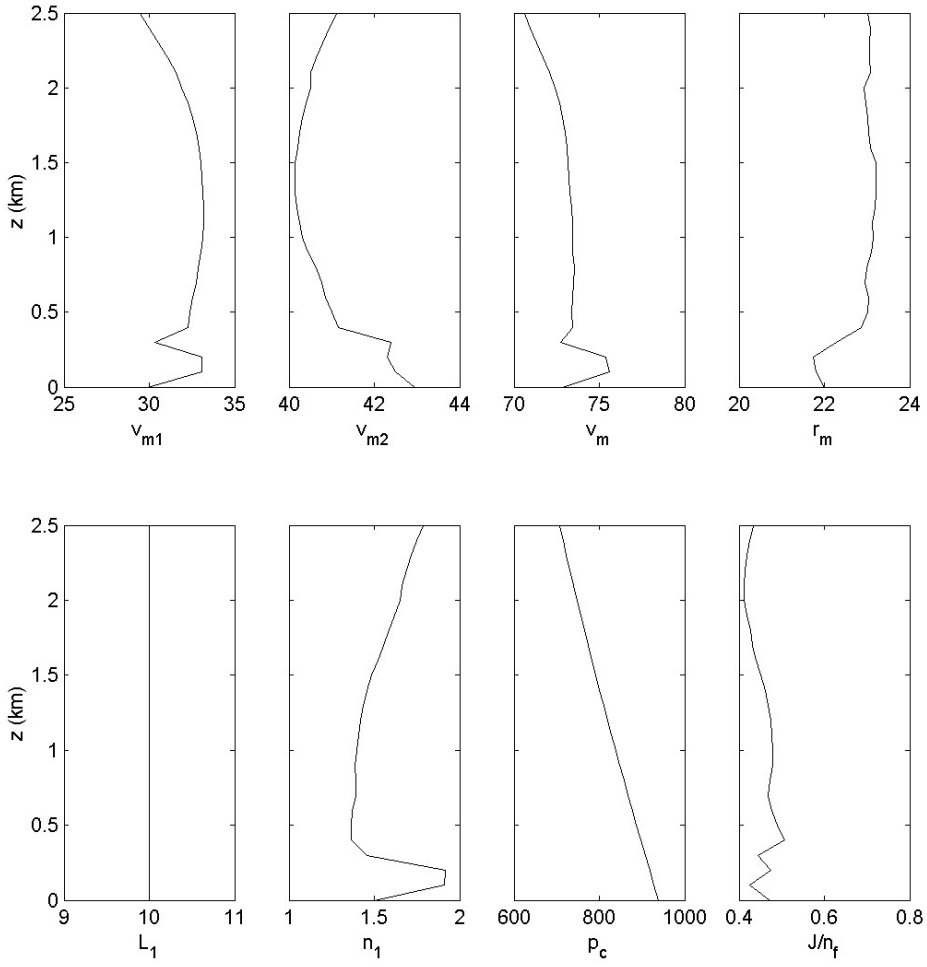

Figure 4.22 Same as Fig 4.20, but for the late period.

Several components of the analysis technique have the effect of increasing the fitted pressure gradient near the RMW, and hence reducing the diagnosed supergradient flow. In particular, radial mislocation of the data relative to the RMW, either by combining the two measurement periods, or by less careful determination of the track, produces more diffuse data near the RMW, a weaker fitted $\partial p/\partial r$ there, and apparently more supergradient flow than found above. This effect is rather similar to that of analysing data from the two periods together. The inclusion of the observation location error in (4.7) also leads to an increase in the estimated gradient-wind.

Similar analyses were carried out using the Holland pressure profile, and the Willoughby profile with only a single exponential (that is, v_{m2} forced to be 0). In the former case, a deep layer of markedly supergradient flow was diagnosed during both periods, while in the latter, a shallower layer of less strongly supergradient flow was found. However, close examination of the residuals from the fit in the vicinity of the RMW showed that a part of the radial pressure gradient there had not been fitted. Essentially, these profiles lacked sufficient flexibility to conform both to the strong gradient near the RMW and to the observations in the outer core, and so underestimated the gradient-wind speed near the RMW. This problem was particularly severe with the Holland profile, which tends (as acknowledged by Holland) to have too broad a maximum at the RMW.

Thus the analysis technique tends to be conservative from the point of view of searching for supergradient winds, in that the omission or alteration of components of it results in the diagnosis of a weaker gradient-wind, and apparently more supergradient flow, than actually found.

4.2.4.2 Gradient-Wind Equation II: Wind Analysis

In this section, the degree of gradient balance is analysed from the opposite perspective. That is, the wind field is analysed and used to radially integrate the gradient-wind equation to give the gradient pressure profile. This is then compared to the dropsonde pressure-height data found above.

The observations are again divided into two periods. The vertical profiles of the fitted parameters for both periods shown in Fig 4.23, and display reasonable vertical consistency, a tendency for the RMW to increase with height, and the maximum wind peaking at 400 m and 1.1 km (earlier period) and 500 m (later period), before decreasing with height. The 1.1 km peak in the earlier period may be spurious, as it is significantly affected by the maximum in profile H, which may be unrepresentative of steady flow because of its sharpness. The *J* value includes the effects of turbulence, asymmetries (apart from that removed by subtracting the motion), and instrument error. While it decreases with height for the earlier period, which is consistent with turbulence dominating the error, the later period shows a broad maximum near 1.5 km. Examination of the residuals shows this is the result of a wave-number one asymmetry of amplitude 5 m s^{-1}, with the strongest winds to the north. This decreases in amplitude to about 2 to 3 m s^{-1} near the surface and at 3 km. It also undergoes a strong cyclonic rotation with increasing height in the lowest 600 m. In contrast, the earlier period shows an asymmetry of about 2 m s^{-1} with less variation with height.

Radial integration of the gradient-wind equation requires a known pressure at some radius. The obvious choices, of using the lowest observed pressure in the eye or the average of all the eye observations, turns out to be unsatisfactory because the fitted profile shape inside the RMW (defined by n_1) is relatively noisy. This occurs because the

observations that affect this are all very near the centre, and small changes in them produce large changes in n_1, which leads to a random variation of a few hPa in the pressure rise from the centre to the RMW, between levels. Thus, it was decided to "anchor" the integration at the mean radius and pressure of the outer core observations.

The wind observations and fitted profiles, and the resulting gradient pressure profile as well as the pressure observations, are shown in Fig 4.24 and 4.25 for a few representative levels for each period. It can be seen that the pressures calculated by integrating the gradient-wind equation agree well with the observations, particularly in the earlier period. A systematic difference of about 2 hPa between the pressure observations near the RMW, and the calculated gradient pressure, could be consistent with supergradient flow. However, this could also be due to the fitted winds being a little too strong in the data void centred around radius 50 km, so it would unwise to regard this difference as evidence of supergradient flow. Note that the decreased barotropic instability of the eye, found in the pressure fits, can also be seen in the change of n_1 here.

4.2.5 Model Simulations

The model described in chapter 3 was modified to allow the option of forcing by the Willoughby parametric profile. There is a choice of parameters for the Willoughby profile, as these have been fitted every 100 m in height, to both pressure and wind data, for both early and late periods. The values v_{m1} = 35 m s^{-1}, L_1 = 24 km, v_{m2} = 35 m s^{-1}, L_2 = 800 km, r_m = 23.2 km, n_1 = 0.9 were chosen to represent a reasonable consensus of the fitted values. It was necessary to set L_1 a little larger than found in the fits to avoid inertial instability. Similarly, n_1 was set to be slightly less than 1 to avoid barotropic instability. The storm translation was set to the value used in the rest of the analysis, (–7.05, 1.31) m s^{-1}.

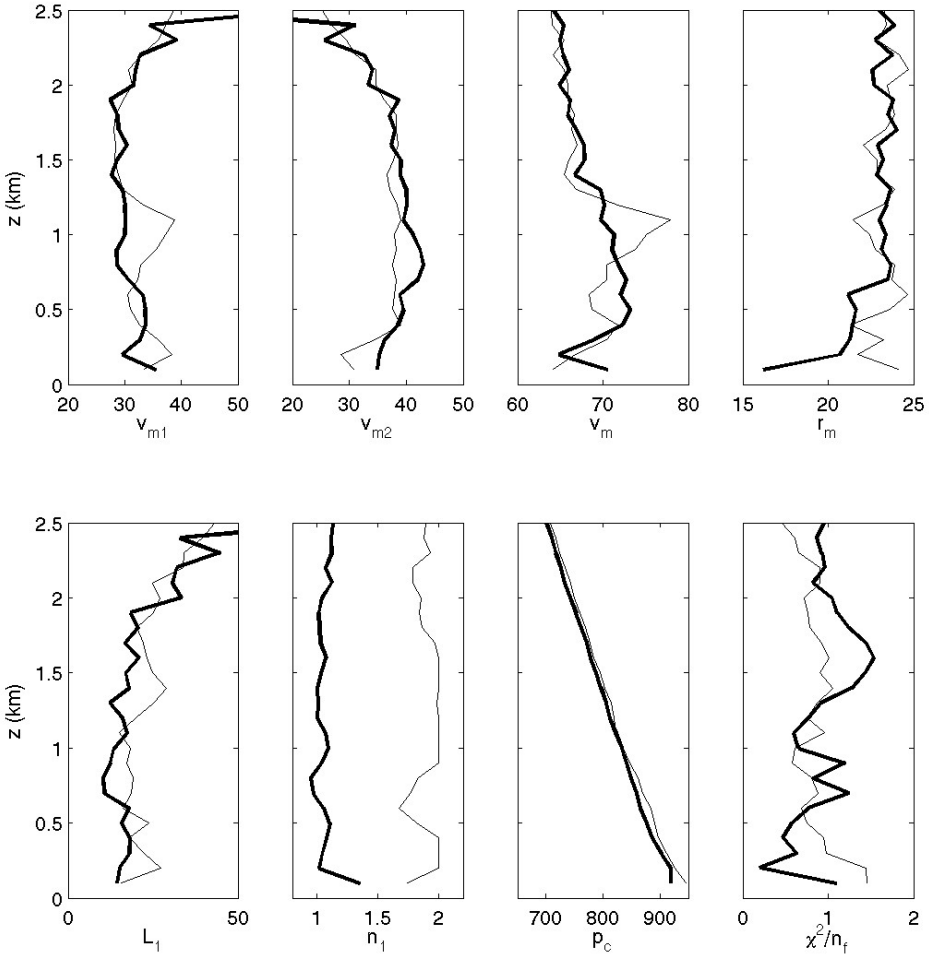

Figure 4.23 Same as fig 4.20, but for the wind fits for the early (light) and late (heavy) periods.

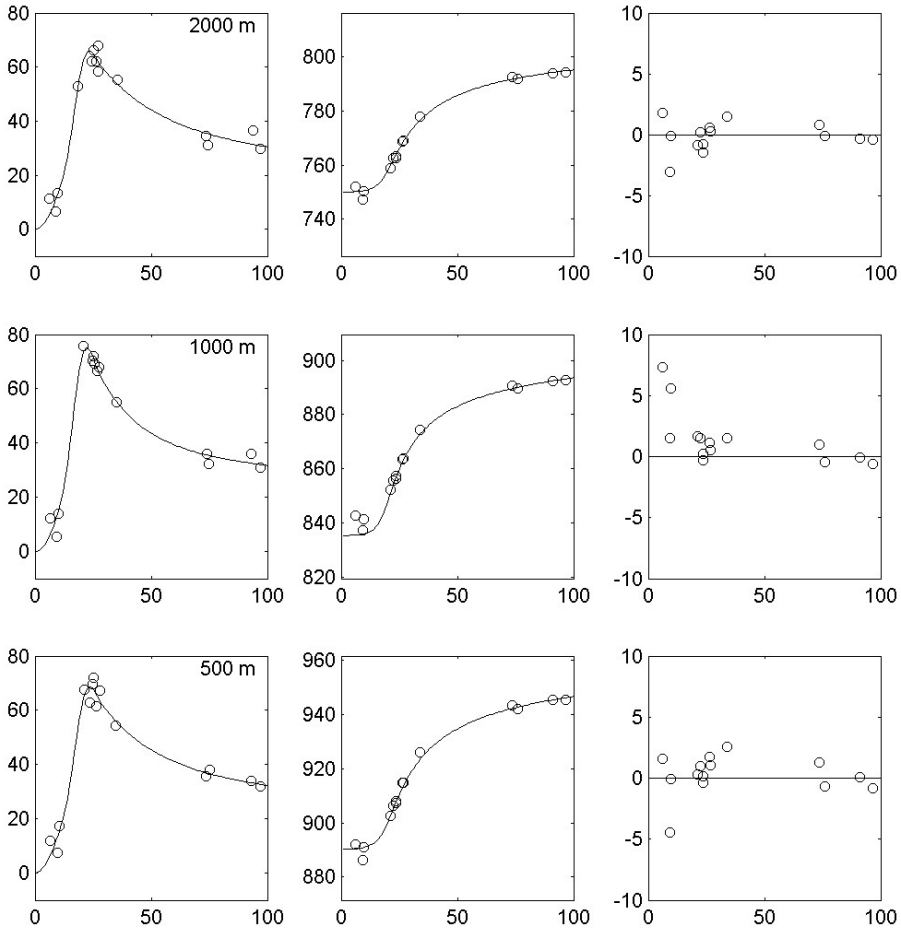

Figure 4.24 Fits of the Willoughby wind profile at 2 km (top), 1 km (middle) and 500 m (bottom), to observations from the early period. Left: Observed and fitted storm-relative azimuthal wind. Centre: Pressure observations and gradient pressure curve. Right: Differences between the gradient pressure and the observations.

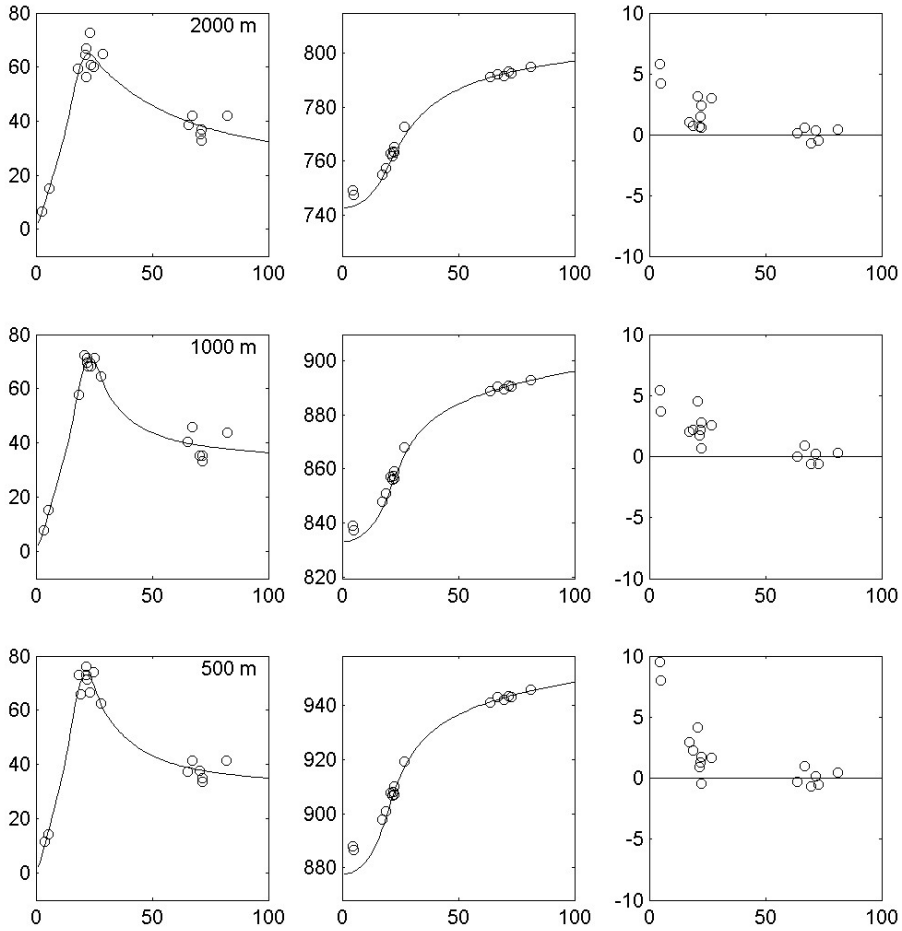

Figure 4.25 Same as Fig 4.24, but for the late period.

Figures 4.26 and 4.27 contain the observed and modelled profiles of storm-relative azimuthal and radial wind components respectively, for the soundings near the RMW. The modelled profiles was interpolated from the model grid to the observed dropsonde trajectories.

To the north of the storm (profiles P, A, B and C) the agreement in both wind components is very good. The weak azimuthal maximum near 500-m height has been faithfully captured, and the depth of the inflow layer is correct, albeit too strong in profiles B and C. Ahead of the storm (profiles D, E, F and G) the inflow is well handled, but the outflow layers in profiles E and G are missing, and the azimuthal flow is less well predicted. The model partially captures the pronounced low-level azimuthal maximum to the south of the storm (profiles H, I, J, K, L and M). One reason for difficulty in this region may be the very sharp gradients, coupled with small differences in navigation. The successful depiction of the marked outflow in profile H is however marred by a severe overprediction of outflow in profiles I, J and K. To the rear, profile N and O were not well handled, with neither the very strong inflow nor the marked decrease in azimuthal component above 500 m, being captured. The radar imagery (Figs 4.3 and 4.4) shows a convective maximum in this area, which would be expected to significantly modify the winds in its vicinity, and is probably the reason for the poor performance here.

The modelled winds were also compared to the outer core observations. The comparisons were less successful and are not shown here. It is believed that the reason for the relatively poor comparisons is the convective band visible in Fig 4.3 near a radius of 70 km in the eastern half of the storm, which had strengthened and contracted slightly by the time of Fig 4.4. While many of the outer core observations were taken in the vicinity of this band, it was not represented in the Willoughby profile used to force the

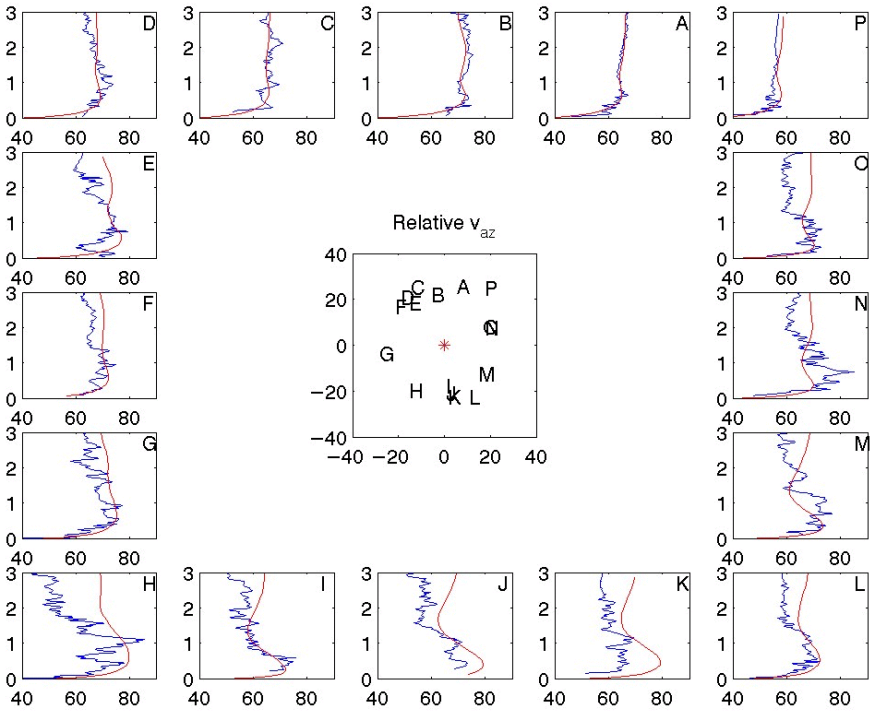

Figure 4.26 Profiles of storm-relative azimuthal wind observed in and near the eyewall of Hurricane Georges (blue) together with the modelled winds along the same trajectory (red). Positions in the centre panel are as the sonde fell through 1 km..

model.

A similar simulation was undertaken with the model forced by the Holland (1980) profile. While the predicted asymmetry was broadly similar, the detailed agreement between model and observations was substantially worse, and is not shown here. For instance, the modelled profile P showed a marked low-level azimuthal maximum with strong outflow above, absent in the observations and simulation with the Willoughby profile.

4.2.6 Discussion

The dropsonde observations in Hurricane Georges have been compared with the theoretical and numerical work described earlier in three ways. The first has been a qualitative comparison of the shapes of the profiles, and in particular the height and relative strength of the low-level jet, with the theory. It was shown both by examining the individual profiles, and mean profiles stratified by radius and/or azimuth, that a substantial part of the large variability between individual profiles is due to a systematic spatial variability within the storm, which is consistent to that found in the modelling work. In particular, the jet becomes closer to the surface towards the storm centre, and is more marked on the left of the storm. Analyses of the observed surface-wind factor were also in good agreement with the theory.

Secondly, the degree of gradient balance was been diagnosed both by comparing the observed winds to an estimate of the gradient-wind obtained from a pressure analysis, and by comparing the observed pressures to an estimate of the gradient pressure field obtained from a wind analysis. The results are quite consistent, in that the flow near the RMW above 400-m altitude seems to be very close to gradient balance in

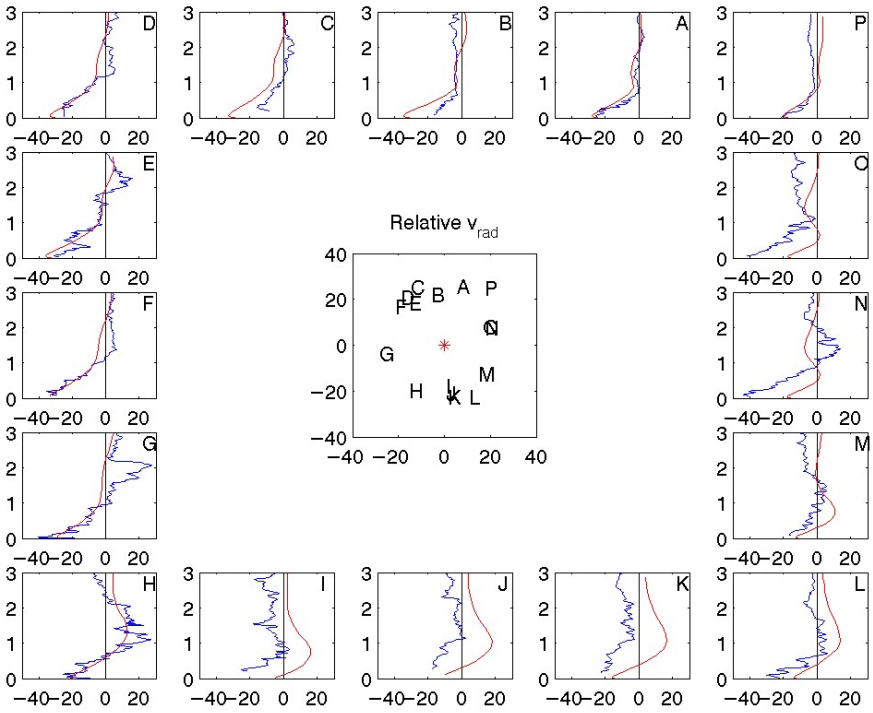

Figure 4.27 Same as Fig 4.26, but for the storm-relative radial wind component.

the later period, and weakly subgradient in the earlier. These results are contrary to the theory, which suggested the flow in the upper part of the boundary-layer should be supergradient. In particular, the apparently subgradient flow in the earlier period is mysterious. The imbalance of approximately 5 m s^{-1} implies a large radial acceleration of $(65^2 - 60^2)/24000 \approx 0.025$ m $s^{-2} \approx 90$ m s^{-1} hr^{-1}. Individual air parcels may not, of course, remain in this area for very long, but this is nevertheless a substantial acceleration. Possibly it is related to changes in storm structure, including the contraction of the RMW, the increase of the outer core winds, and the formation of an extensive stratiform rain shield, already noted. The formation of a convective ring near 60-km radius discussed above may represent the beginning of an eyewall replacement cycle. If so, this is known to lead to the eventual weakening and replacement of the inner eyewall and associated wind maximum, so could perhaps explain the lack of supergradient flow. Unfortunately, immediately after this observational period Georges began to weaken under the influence of shear and made landfall, so this must remain speculation.

There may also be issues with the analysis technique. For instance, the hydrostatic integration necessarily ignores the effects of liquid water loading, and assumes hydrostatic balance. Although the method used for this integration described above yields improved consistency between the upwards and downwards integrations, differences of up to a few hPa remain and could be affecting the results.

The amount of data is quite small, and is unevenly distributed in radius. Thus it is possible that over-fitting is occurring, that is, that errors (instrumental or of representation) in the data are resulting in a spurious increased pressure gradient in the fitted profile. In particular, if the vortex tilt is not taken account of, a weaker gradient

is fitted and supergradient flow is diagnosed from about 500 m to 1500 m, but a marked azimuthal wave-number one pattern appears in the pressure residuals. Similarly, combining the two periods “smears out” the pressure gradient near the RMW as shown above, and produces some apparently supergradient flow. However, both the time change and the vortex tilt are physically plausible features of the cyclone, which appear from the available data to be real, and it is therefore argued that their neglect would be an error.

4.3 Hurricane Mitch

4.3.1 Introduction and Data Coverage

Hurricane Mitch was one of the deadliest Atlantic hurricanes on record, with fresh-water flooding following its landfall in Honduras claiming over 9,000 lives. Its peak intensity was estimated by the NHC to be 155 knots, with a central pressure of 905 hPa, at 1800 UTC on 26 October 1998. This is an October intensity record for the Atlantic basin, and occurred as Mitch moved steadily into the western Carribbean. Following this, Mitch gradually slowed, began to weaken, and eventually turned south towards the Honduras coast. The NHC best track is shown in Fig 4.28. Further details of Mitch may be found in Guiney and Pasch (1999) and Guiney and Lawrence (1999).

A Hurricane Research Division aircraft extensively surveyed the core region of Hurricane Mitch late on October 27th, by which time the central pressure had risen to around 930 hPa and was continuing to rise. This was some 30 hours before the landfall on Honduras, with the nearest land approximately 85 kilometres away. A total of 10 radial legs were flown, during which 31 GPS dropsondes were deployed, all except one of which were within 100 km of the storm centre. The storm-relative dropsonde launch points, and aircraft radial legs, are shown in Fig 4.29.

The data used in this analysis were:

- Thirty GPS dropsonde soundings within 100 km of the centre of the storm, summarised in Table 4.2, in the same format as those used for the analysis of Hurricane Georges.
- Research aircraft measurements of three-dimensional wind, thermodynamic, and storm track data. These were storm-relative winds in cylindrical coordinates, averaged into 0.5 km radius bins for each of the ten radial legs flown.

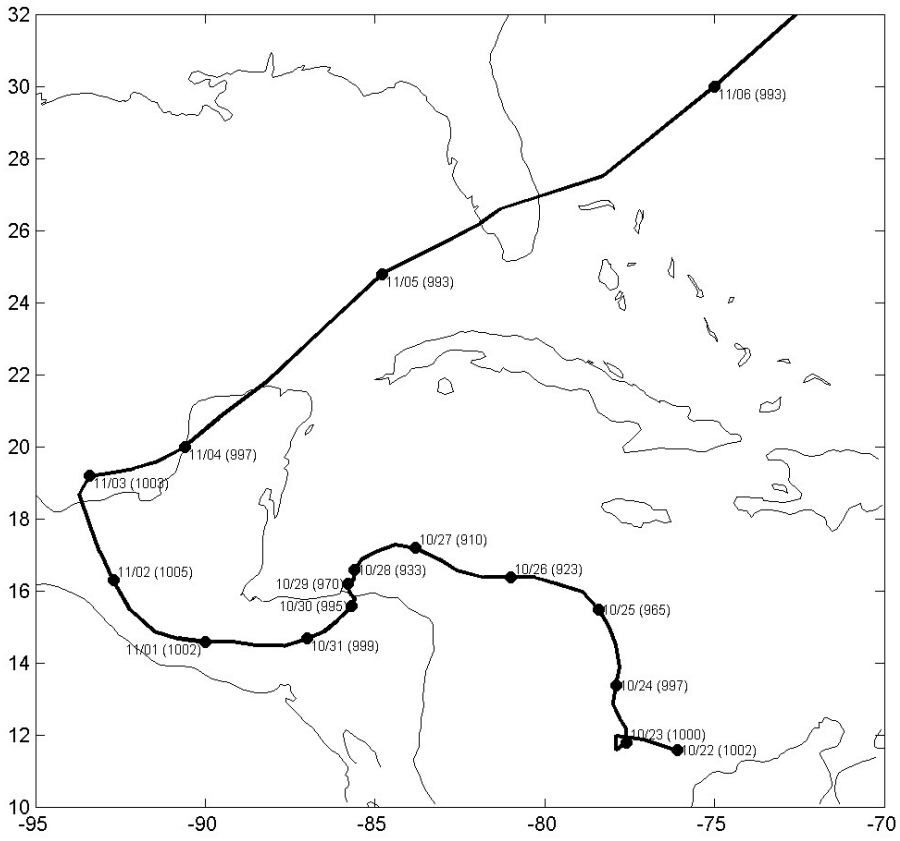

Figure 4.28 The best-track analysis for Hurricane Mitch from the U.S. National Hurricane Center. Tick marks showing the month, day and estimated central pressure (hPa) are at 00UTC.

Table 4.2 The same as Table 4.1, but for Hurricane Mitch.

Name	Serial No	Date/Time (UTC)	Lat (N)	Lon (W)	Pr (mb)	Comments
I	983410124	981027/212857	16.92	85.78	679	NW eyewall.
V	983310027	981027/213312	16.69	85.59	655	Eye.
N	981040049	981027/213636	16.52	85.41	668	SE wall. Poor GPS.
d	983310121	981027/213911	16.41	85.29	686	SE eyewall. Super near surface.
e	983340064	981027/215318	16.68	84.79	695	50 nm E of center.
P	983340066	981027/220330	16.71	85.26	681	E wall.
Q	983340078	981027/220355	16.71	85.28	676	E wall.
R	974530045	981027/220423	16.70	85.32	673	E wall.
K	981040046	981027/221223	16.67	85.89	689	Winds very intermittent, hence long filter.
b	982720392	981027/222105	16.59	86.43	697	Mixed RH, poor GPS.
L	983410111	981027/223448	16.48	85.90	683	SW wall.
C	983340050	981027/224250	16.76	85.45	666	NE wall.
B	974910010	981027/224311	16.78	85.43	668	Assumed to not reach sfc. NE wall. Split RH.
A	983410045	981027/224330	16.80	85.41	672	NE wall.
E	973840047	981027/230601	16.91	85.60	676	N wall.
F	983410106	981027/230633	16.88	85.61	675	N wall.
G	983310142	981027/230731	16.82	85.61	677	N wall. Split RH sensor.
M	983310127	981027/231352	16.37	85.60	668	S wall.
c	981810013	981027/232125	15.99	85.44	695	50 nm south.
O	983340068	981027/233547	16.47	85.32	675	SE wall.
S	983340088	981027/233635	16.48	85.37	672	SE wall. Big updrafts. Poor GPS.
T	983340063	981027/233712	16.50	85.40	671	SE wall. Poor GPS.
X	982720319	981027/233954	16.57	85.58	659	Eye.
J	972630028	981027/234436	16.72	85.86	696	NW wall.
U	983410126	981028/001452	16.47	85.68	505	Inside eye.
W	983340065	981028/001608	16.52	85.60	504	Near center of eye.
Y	983310180	981028/001709	16.58	85.53	504	Inside eye.
D	982720393	981028/001800	16.64	85.52	504	Inside eye, but intersects wall.
H	983410113	981028/002903	16.73	85.57	503	Inner edge/eye, intersects eyewall.
a	981040005	981028/003143	16.93	85.57	510	Outer eyewall/rainband.

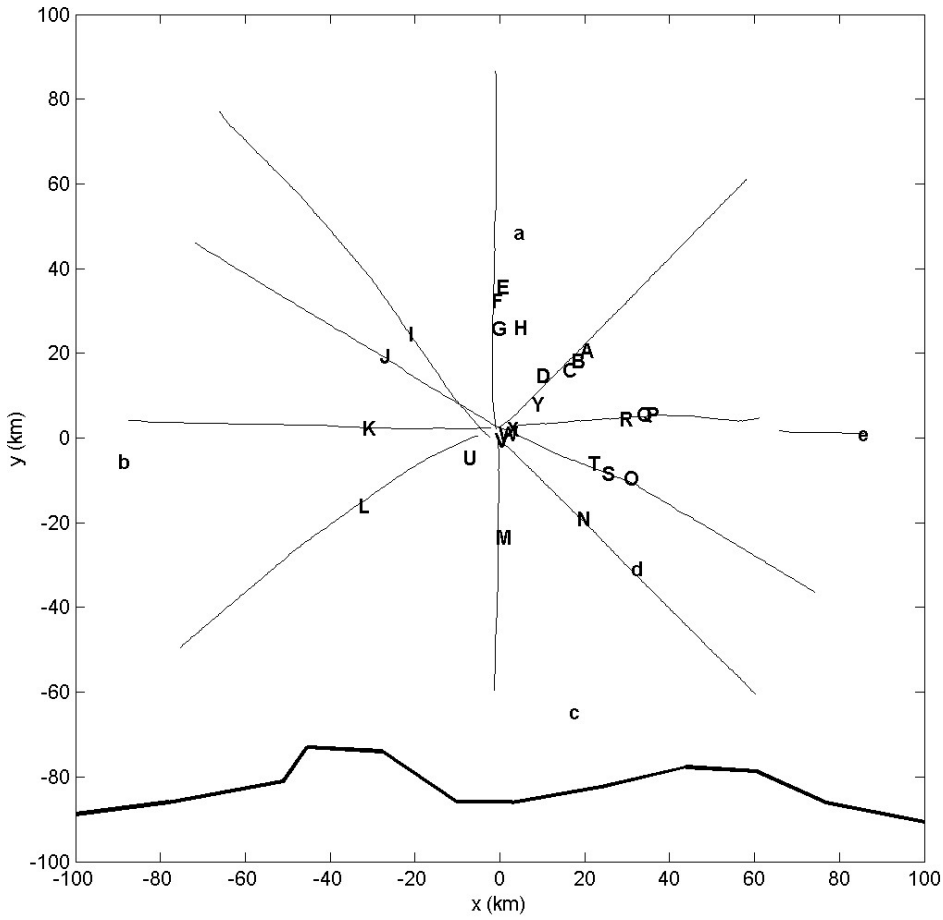

Figure 4.29 The aircraft reconnaissance radial legs (light curves) and dropsonde deployment points used in this study, in storm-relative coordinates. The heavy curve to the south of the panel is the coastline of Honduras.

- Several radar composite images from the lower-fuselage radar on the HRD aircraft
- Various infra-red, visible and passive microwave satellite imagery from GOES, DMSP and TRMM satellites.
- Analyses of the track of Mitch from NHC and HRD. Two analyses were available from HRD, with different degrees of smoothing. These will be referred to as the HRD high-resolution and low-resolution tracks. The various tracks are discussed in more detail below.

During this intensive observational period, Mitch had an asymmetric appearance on radar imagery (Fig 4.30), with the bulk of the eyewall convection located in the north-east, or left rear, quadrant, and an opening in the eyewall to the southwest. Similarly, the surrounding stratiform rain was predominantly located to the north and east. Examination of passive microwave imagery from DMSP and TRMM satellites (not shown here) shows that this asymmetry had first become apparent shortly after the time of maximum intensity, and that it continued to strengthen until landfall.

The causes of the asymmetry in the radar imagery, and the progressive weakening of Mitch, are not obvious. Motion can create eye asymmetries, but the slow speed of Mitch, and the fact that the strongest reflectivity is in the left rear quadrant, eliminates this possibility. Environmental wind shear is another common cause of asymmetries and weakening in tropical cyclones. However, there is little evidence of it being a substantial contributor here. In particular:

- Analyses from the Australian Bureau of Meteorology's Global Analysis and Prediction System were examined, and showed no evidence of significant shear over Mitch during this period.

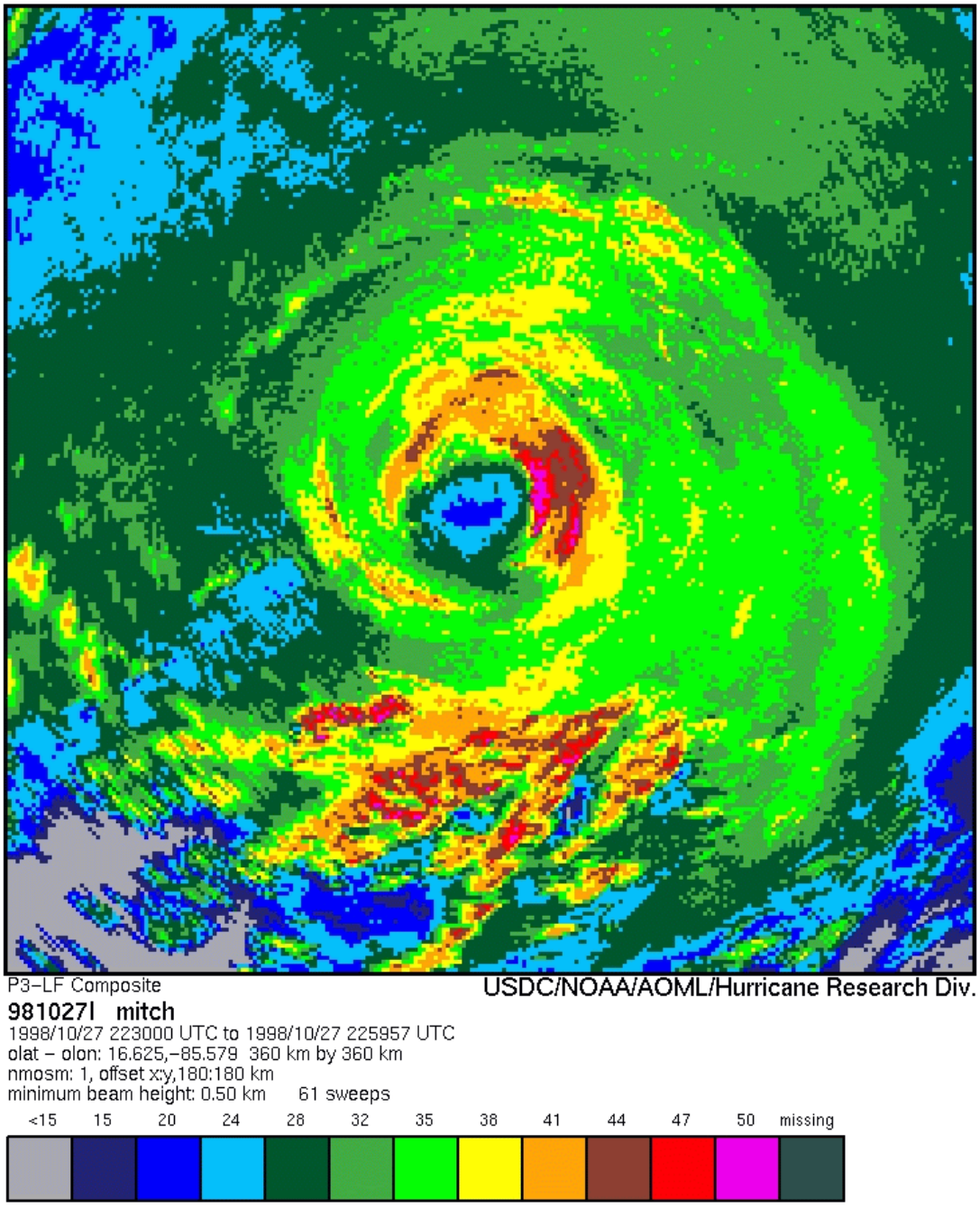

Figure 4.30 Composite airborne radar reflectivity radar image for Hurricane Mitch from 2230 to 2300 UTC on October 27, 1998. Image courtesy of NOAA HRD.

- Infra-red and visible satellite imagery showed that the cirrus overcast maintained a symmetric appearance while the storm was weakening, and up until landfall.
- Passive microwave imagery from the TRMM and DMSP satellites showed that spiral bands were present in all sectors around the storm, up until landfall.
- Usually, a cyclone weakening due to environmental shear becomes asymmetric in its outer regions, before the core is affected. In the case of Mitch, this has not occurred.

Another possible reason for the weakening is that the slow track meant Mitch was over progressively colder water, due to upwelling and mixing. Sea surface temperature observations were available from six airborne expendable bathythermographs deployed during the reconnaissance mission. Five of these recorded sea surface temperatures in the range 28 to 29^{o}C, while one (in the southwest eyewall, near islands) reported 26.5^{o}C (P.G. Black, personal communication 1998). These temperatures seem too warm to have been a major cause of the weakening, and would not have produced a marked asymmetry like that seen.

A further possibility is the proximity to land. Tropical cyclones weaken after landfall because the low heat capacity of soil means that the surface heat and moisture fluxes that fuel the storm are not able to be sustained after landfall (Tuleya, 1994). Usually, this does not noticeably affect the intensity before landfall, but Mitch approached land very slowly. The final 80 km to Honduras, after the study period, took some 30 hours, much longer than cyclones usually require to cross such a distance. Thus it is hypothesised that Mitch was affected by reduced fluxes for a relatively long while before landfall, allowing more time for the storm to respond to the reduced energy supply than is normally the case. It is also possible that the mountainous terrain of Honduras contributed. The effect of land will be explored further below.

4.3.2 Cyclone Track

All dropsonde and aircraft data were first renavigated into a Cartesian coordinate system with origin tangent to the earth at 16.65°N, 85.567°W and the *y*-axis directed northwards. Times were expressed relative to a nominal base time of 23 UTC on October 27th, 1998. The base latitude and longitude chosen were the location of Mitch at this time, interpolated from the NHC best-track analysis. The HRD aircraft storm-relative cylindrical coordinate wind data were converted back into earth-relative Cartesian winds, using the same track (i.e. the HRD high-resolution) as for their conversion to storm-relative cylindrical coordinates, before being renavigated into the coordinate system used here.

The three track analyses available are shown in the upper panel of Fig 4.31, together with aircraft-derived centre-fixes from HRD. The aircraft fixes from the mission being analysed here suggest the track is close to directly southwards, which is confirmed by some Air Force reconnaissance fixes from the following day, shortly before the storm slowed and abruptly changed direction. Neither of the coarse resolution tracks depict the southward trajectory during the mission particularly well, while the high resolution HRD track also appears to diverge at the end of the mission. Thus it was necessary to derive a track from the flight-level observations.

Using the aircraft data out to radius 50 km, the track was found to be given by $(x_t, y_t) = (-2.5, -5.8)$ km and $(u_t, v_t) = (-0.20, -2.09)$ m s^{-1} by the translating-pressure-fit method. The Marks-circulation method gave $(x_t, y_t) = (-1.9, -4.1)$ km and $(u_t, v_t) = (-0.14, -1.63)$ m s^{-1}, which is slightly slower but otherwise barely distinguishable. The former of these is plotted in the lower panel of Fig 4.31, and appears to be more consistent with the aircraft centre fixes from the mission than the other tracks. It will be used for the storm-relative coordinate transformations in the rest of this analysis.

The surface track, as found by the translating-pressure-fit method applied to the dropsonde splash pressures, was found to be given by $(x_t, y_t) = (-2.9, -7.2)$ km and $(u_t, v_t) = (-0.08, -1.96)$ m s^{-1}. The difference between this and the aircraft track indicates a vortex tilt of, on average, (0.6,1.3) km from the surface to 3 km was present during the observational period, with the surface centre to the southwest of that at flight-level.

4.3.3 The Wind Field

Mean profiles of storm-relative azimuthal and radial wind were calculated for the annuli 0 to 15 km, 15 to 25 km, 25 to 40 km, and 40 to 100 km. These represent respectively the inner eye, the inner and outer sides of the eyewall, and the outer core, and are shown in Fig 4.32. The mean azimuthal wind in the outer core is nearly constant with height above 1 km, and decreases steadily below that towards the surface. The inflow layer here is approximately 1.3 km deep. The annulus around the outside of the eyewall has a marked azimuthal wind maximum at about 700-m height, while the mean inflow exceeds 30 m s^{-1} near the surface, is about 1 km deep, and lies beneath a deep layer of outflow. The inner edge of the eyewall is characterised by a very strong and sharp maximum in the azimuthal component near 250-m height. The near-surface inflow is a little weaker and deeper than on the outside of the eyewall, and similarly capped by outflow above 2 km. The eye mean sounding has nearly constant azimuthal flow with height, with a weak maximum near 250-m height, while the mean radial component is close to zero.

The maximum in the azimuthal flow becomes more pronounced and closer to the surface as we move inwards across the eyewall, and always lies within the inflow layer,

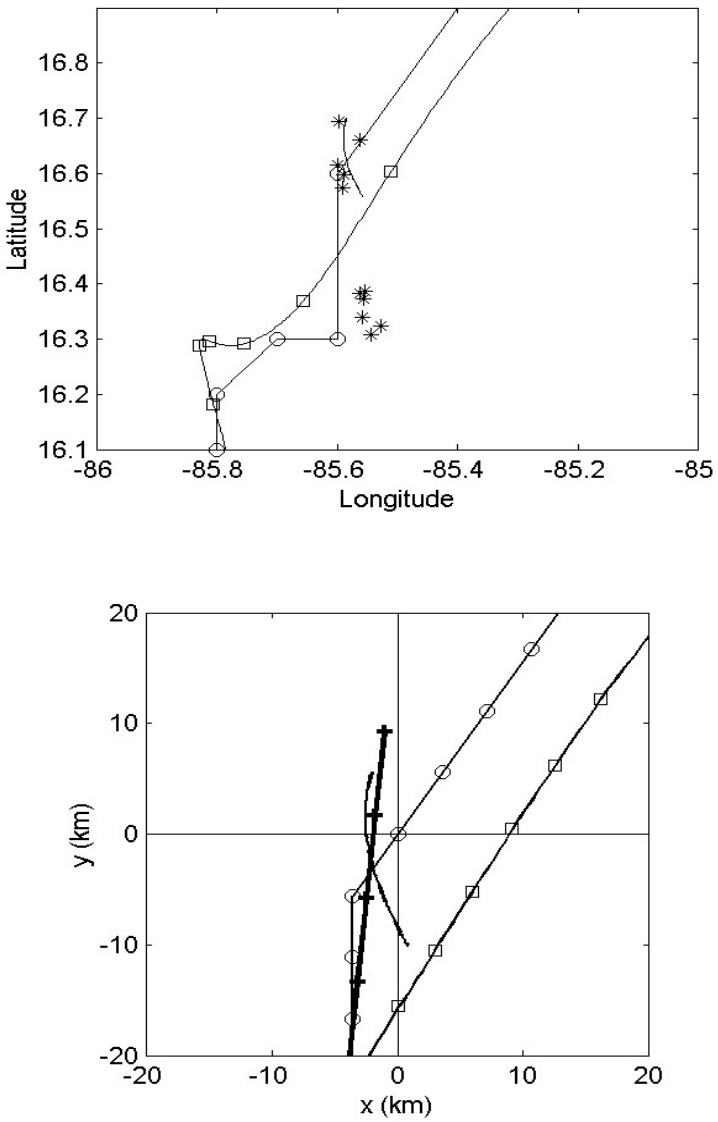

Figure 4.31 Top: NHC track (line with circles every 6 hours), HRD low-resolution track (line with squares every six hours) and HRD high-resolution track (short line) for Hurricane Mitch around 00UTC on October 28th, together with aircraft fixes (asterisks) from the mission discussed here (northern five) and an Air Force reconnaissance mission commencing some 6 hours afterwards (southern six). Bottom: NHC and HRD tracks (with hourly tick marks), together with track found by translating-pressure-fit method as described in text.

in accordance with the analytical and numerical modelling. The radial trend in inflow is similarly in agreement with the models for the two outer annuli, but the deeper inflow on the inner side of the eyewall is contrary to the theory. The data are however unevenly distributed in azimuth, and so this apparent anomaly may be due to insufficient sampling, in the presence of a strong azimuthal asymmetry.

The available dropsonde profiles are now divided into three groups, the near eyewall (20 profiles with radius between 15 and 40 km), the eye (5 profiles with radius less than 15 km) and the outer core (5 profiles with radius 40 to 100 km). The one remaining profile, at a radius of over 400 km, was not used. The flow in each region is now discussed.

4.3.3.1 Inner Core

Figures 4.33, 4.34 and 4.35 show the earth-relative speed, storm-relative azimuthal and radial flow components, and location, measured by these dropsondes. The data include three sets of closely spaced soundings across the eyewall, profiles A to D, E to H and P to T. Each set shows a similar trend, with the low-level wind speed maximum becoming more pronounced and closer to the surface, towards the centre of the storm. The upstream end of the most intense eye-wall convection (profiles P to T) has a strong deep inflow. The inwards component near the surface is around 40 m s^{-1} (or even 50 m s^{-1} if profile O is included), and the inflow layer 2 km deep at the outer end of the transect. The strength and depth of the inflow diminish towards the centre of the storm, and weak outflow is apparent in the upper part of profile T.

The second transect, profiles A to D, have weaker near-surface inflow, and more marked outflow aloft. A similar trend to that in profiles P to T, of decreasing inflow

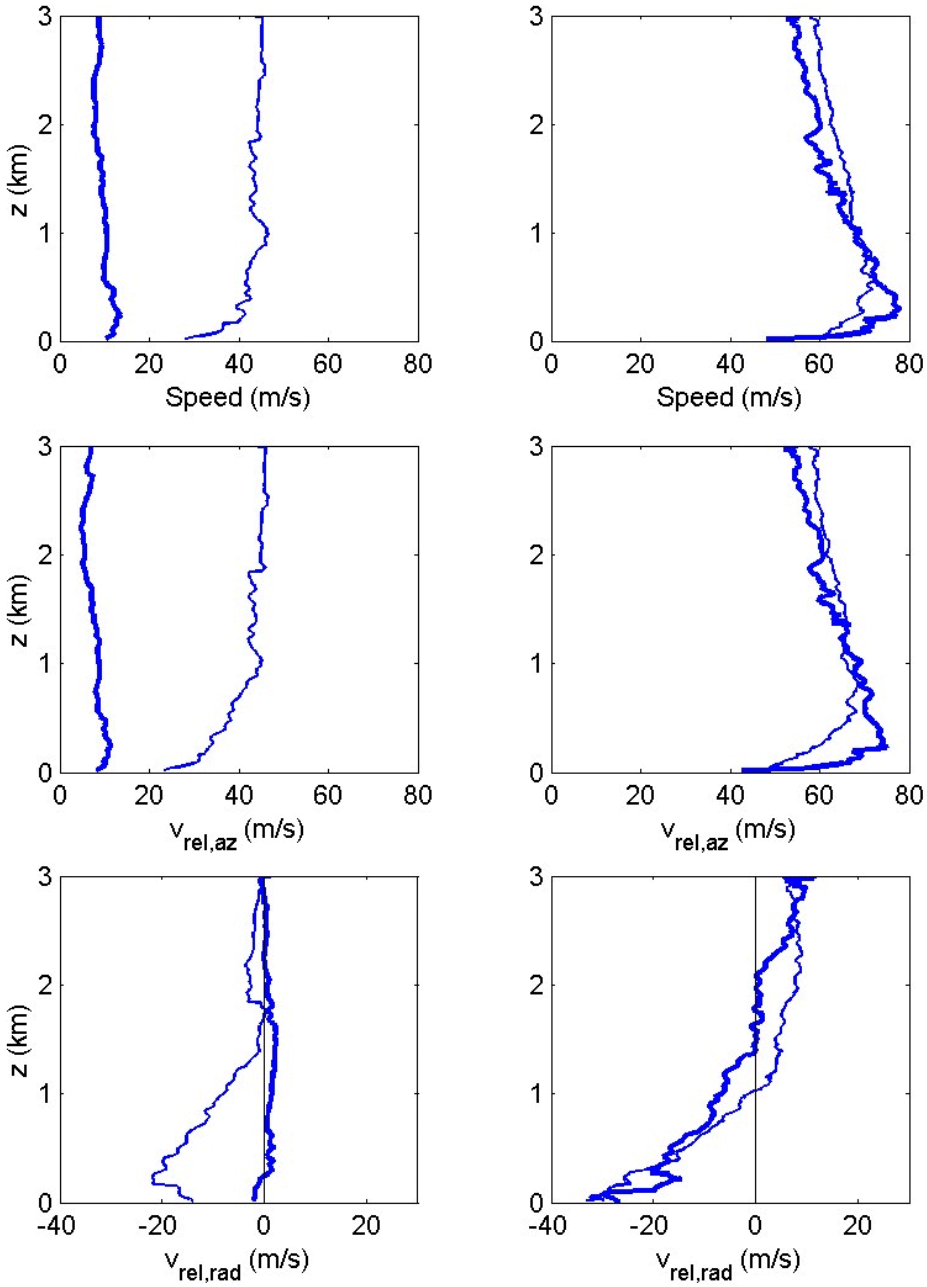

Figure 4.32 Mean profiles of wind speed (top, storm-relative azimuthal wind (middle) and storm-relative radial wind (bottom), over radius ranges 0 – 15 km (left, heavy), 15 – 25 km (right, heavy), 25 – 40 km (right, light) and 40 – 100 km (left, light).

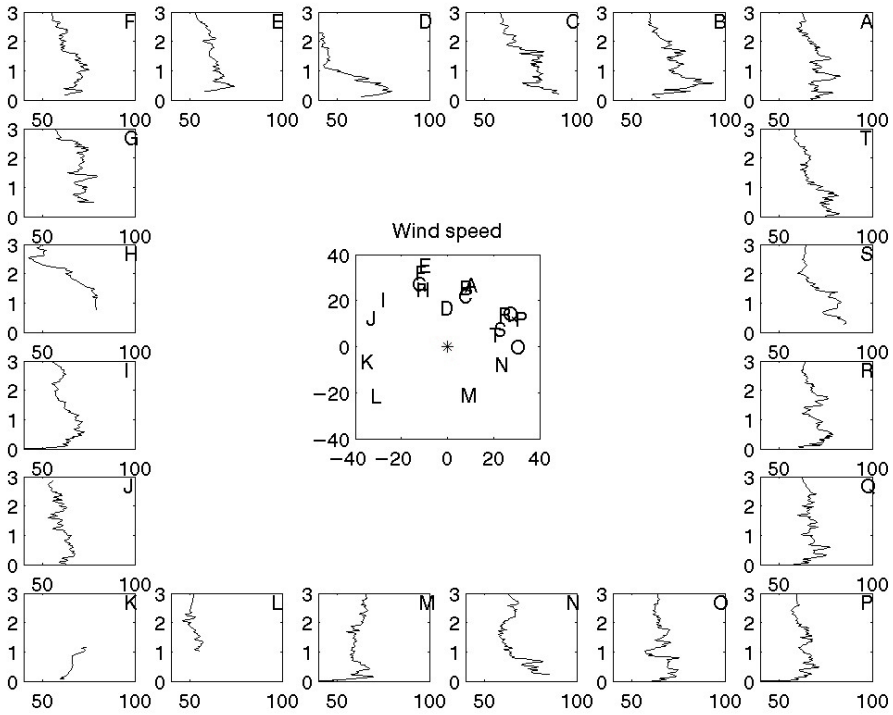

Figure 4.33 Profiles of earth-relative wind speed in Hurricane Mitch for the 20 near-eyewall dropsondes.

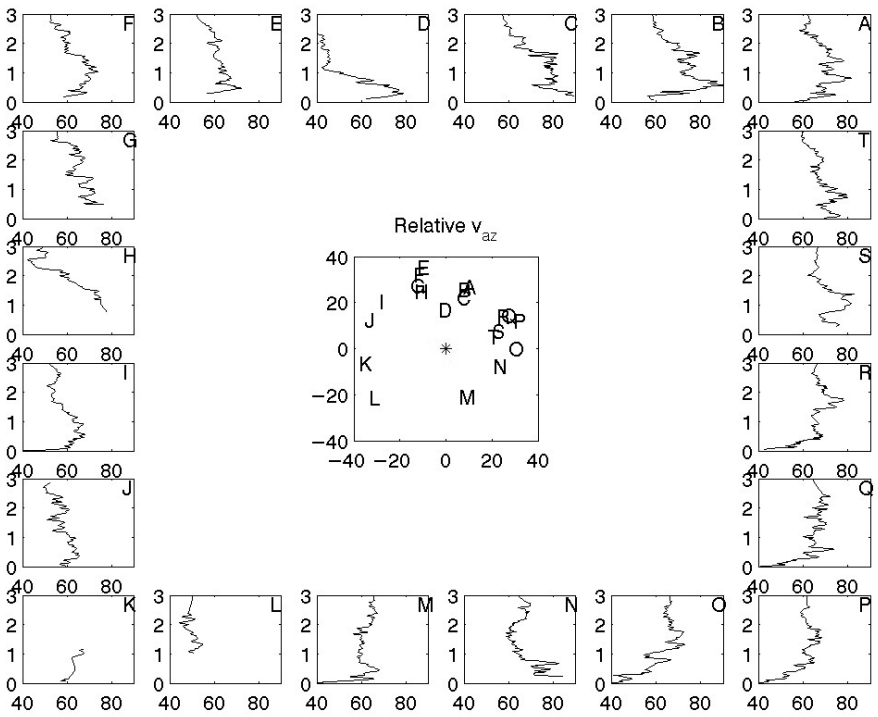

Figure 4.34 Same as Fig 4.33, but for storm-relative azimuthal wind.

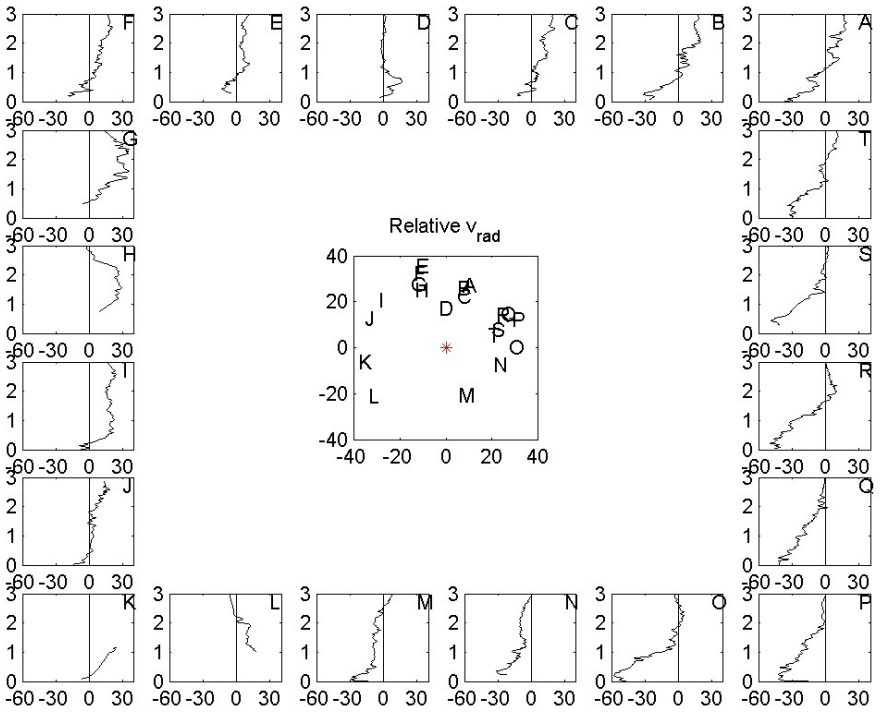

Figure 4.35 Same as Fig 4.33, but for storm-relative radial component.

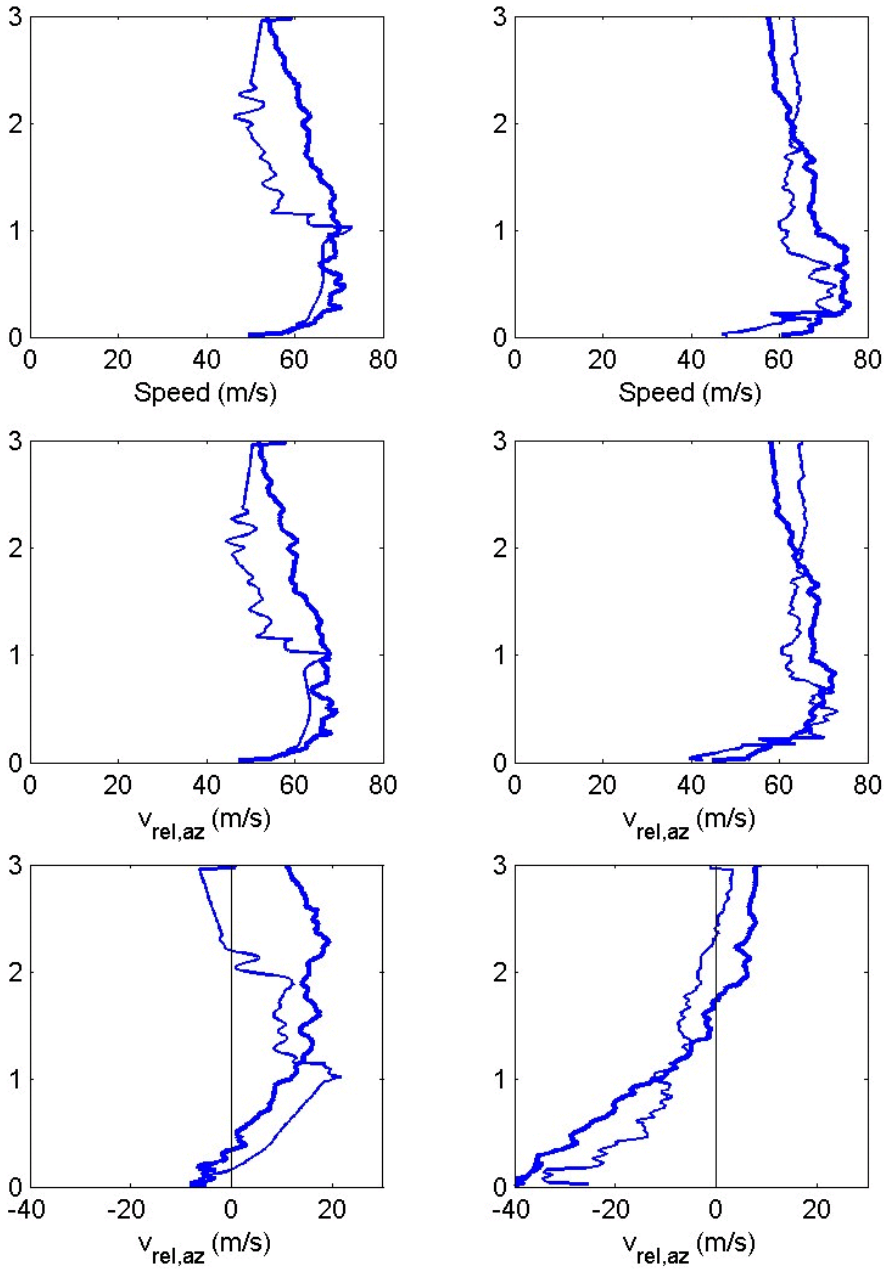

Figure 4.36 Profiles along dropsonde paths of wind speed (top), storm-relative azimuthal (middle) and radial (bottom) components, for dropsondes in the 15 to 40 km annulus. The left panels have the two western quadrants, and the right panels the eastern. Heavy curves denote the northern quadrants, and light curves the southern.

towards the centre, can be seen in profiles A to C. Profile D represents a discontinuity here, possibly as it was taken at a different time. Little change in the jet structure is apparent in the third transect, E to H. Inflow is weak and confined close to the surface in these profiles, with a deep layer of outflow above, which increases in strength towards the centre of the storm. However, as in the other transects, the radial variation of inflow implies low level convergence.

These strong radial gradients apparent in the transects may explain the substantial differences between profiles N and O, which are at 1-km radii of 25 and 31 km, respectively. The substantial difference in the shape of the azimuthal wind profiles appears to be because they lie in a region of such strong radial gradient, and is not due to transient effects.

Figure 4.36 shows the mean wind components in each quadrant. The maximum inflow is in the northeast quadrant in the lowest 1.2 km, and it rotates anticyclonically through the southeast to the southwest above that. The maximum azimuthal component lies to the west very near the surface, followed by a layer in which all the quadrants except the southwest are roughly equal. The northeast quadrant has the strongest azimuthal winds between 700 m and 1.8 km, and the southeast quadrant above that. Thus the asymmetry in this component also rotates anticyclonically with height. Furthermore, the strongest azimuthal winds at any level tend to occur about one quadrant downstream of the strongest inflow, that is, the asymmetries are in quadrature.

The above phase relationship and anticyclonic rotation with height of the wind components, is identical to that of the dominant asymmetric component identified in Chapter 2, which was shown to be equivalent to a frictionally stalled inertia wave. However, the strongest storm-relative inflow is here located in the northeast or left-rear

quadrant, not the right-front as the theory there predicts. Thus the vertical structure of the asymmetry suggests that frictional processes may be governing the form of the asymmetry, even though it is clearly not being generated by the motion-induced surface-friction asymmetry. The possibility that the asymmetry is due to the proximity to land will be examined later.

4.3.3.2 The Winds in the Eye

The five profiles in the eye fall on an approximately north-south transect. The wind components from these soundings, and their positions, are shown in Fig 4.37. The radial flow components show a marked through-flow, with those to the south of the centre exhibiting inflow, and those to the north, outflow. Profiles U and Y, at radii near 10 km, show pronounced near-surface maxima in the azimuthal component, while the remaining profiles, within a few kilometres of the centre, have little in the way of coherent vertical structure.

4.3.3.3 The Winds in the Outer Core

The five outer core wind profiles are plotted in Fig 4.38. The profiles clearly exhibit general through-flow from the east to the west. The three profiles to the east and north of the storm show wind speed maxima near 1 km height, which are absent from the other two.

4.3.3.4 Surface-Wind Factor

The surface-wind reduction factors were analysed from three levels, 500 m, 1.5 km and 2.5 km. As with Hurricane Georges, it was necessary to use the 50-m wind as the “surface” wind, as a substantial proportion of the sondes failed to report winds below this level. The analyses, which are shown in Fig 4.39, were prepared using the same objective analysis technique and modelling of the observational and background errors

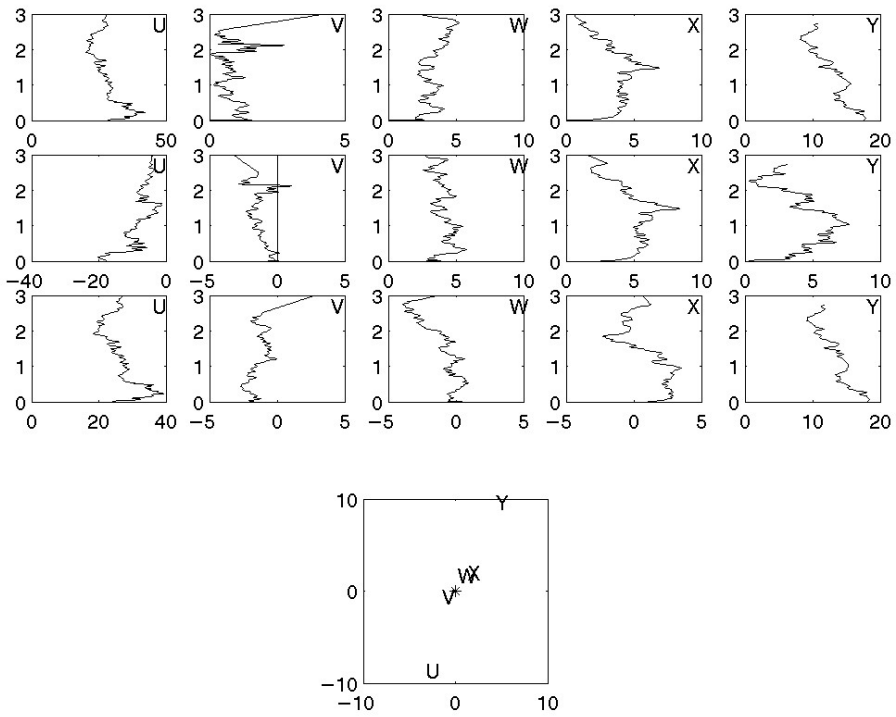

Figure 4.37 Profiles of wind speed (top row) and storm-relative azimuthal (second from top row) and radial (second from bottom row) components, for five dropsondes in the eye of Mitch. Positions at 1-km height are shown in the bottom panel.

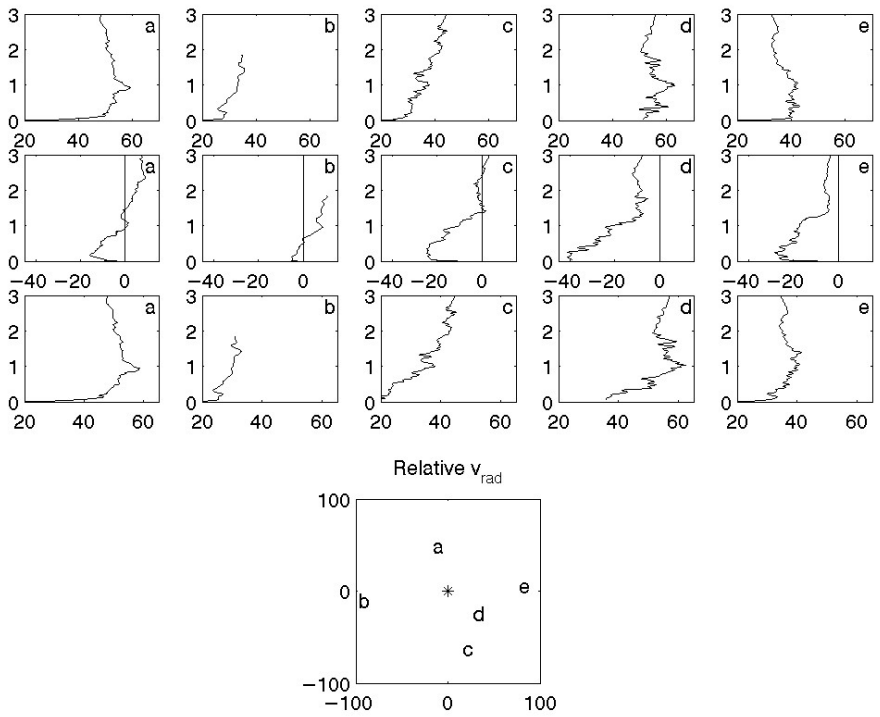

Figure 4.38 The same as Fig 4.37, but for profiles outside of radius 40 km.

as for Hurricane Georges.

The analyses from the lower two levels show a wave-number two structure, with maxima to the east and west of the storm. Whether this is also present in the reduction from 2.5 km is unknown, as an absence of data at the higher level to the west of the storm prevents a reliable analysis there. There is a clear tendency for the higher values to occur near the eyewall from the lower two levels, and within it from 2.5 km.

The general increase towards the storm centre is consistent with the theoretical analysis in earlier chapters. However, the asymmetry is different. As with other aspects of the wind asymmetry in Mitch, this appears to be because it was produced by something other than motion.

4.3.4 Analysis of Balance

The same steps are followed as in the analysis of balance in Hurricane Georges. However, the analysis is more straightforward as there is no need to split the data into two periods. This also has the advantage that there are approximately twice as many observations at each level, and less of a data void just outside the RMW, as in Georges.

4.3.4.1 Hydrostatic Integrations

As before, it was necessary to carry out the hydrostatic integrations taking account of the change of radius of each sonde as it fell. In fact, because of the strong radial flow in some quadrants, the differences between the surface pressure calculated by a downwards integration along the slant trajectory from the aircraft and the splash pressures are quite large. In particular, the mean difference is 1.8 hPa, with a standard deviation of 3.5 hPa, while individual values ranged from −6 to 10 hPa.

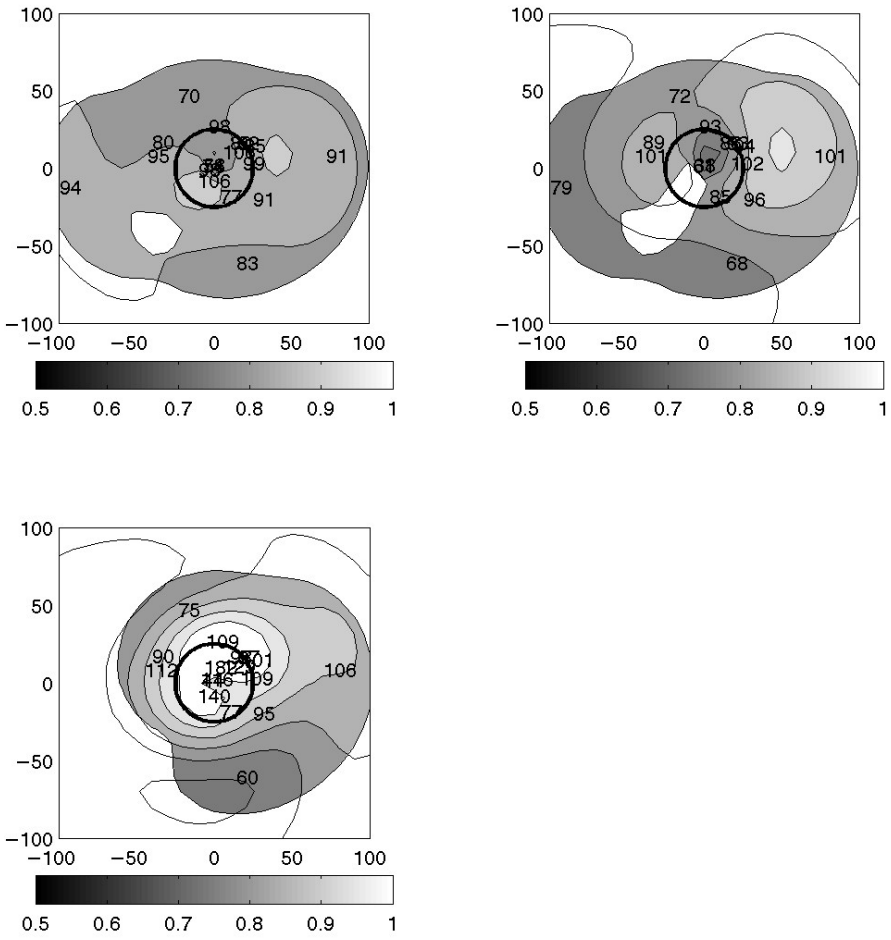

Figure 4.39 Analysis of surface-wind factor, from 500 m (top left), 1.5 km (top right) and 2.5 km (bottom), together with observed values multiplied by 100. Unshaded parts of the plots correspond to areas where low data density results in the estimated analysis error being relatively large; in particular, greater than 0.08. Contour interval is 0.1.

The technique differed from that used on Georges only in the way the radial virtual temperature gradient was estimated. Instead of using a piecewise linear fit, it was found that an analytical profile similar to the Holland (1980) pressure profile fit the data well. In particular, curves of the form

$$T_v(r) = T_c - \Delta T \exp(-(r_T/r)^{b_T}) \qquad \textbf{(4.8)}$$

were fit to the temperature data on pressure surfaces, at 1 hPa intervals. Here, T_c is the virtual temperature at the cyclone centre, ΔT is the environment to centre virtual temperature difference, r_T defines the radial extent of the warm core, and b_T the shape of the profile.

A sample fit is shown in Figure 4.40. The top panel shows the virtual temperature observations as a function of radius, and the fitted curve. There is a degree of scatter near the RMW. The same observations are plotted and analysed in the bottom panel; the analysis was prepared by a similar OI method to that used for the surface-wind factor analyses. It is clear that the warm core was displaced to the southwest of the vortex centre, and that this is the cause of much of the scatter near the RMW visible in the top panel. A similar asymmetry is also apparent in the flight-level temperature observations, and at other levels (not shown). This temperature asymmetry is hydrostatically consistent with the vortex tilt previously diagnosed, and is presumably a result of the general subsidence on this side of the hurricane. Although an asymmetry is present, only the radial temperature gradient is used from these analyses. As it comprises a relatively small correction, the axisymmetric temperature analyses were deemed to be sufficiently accurate for this purpose.

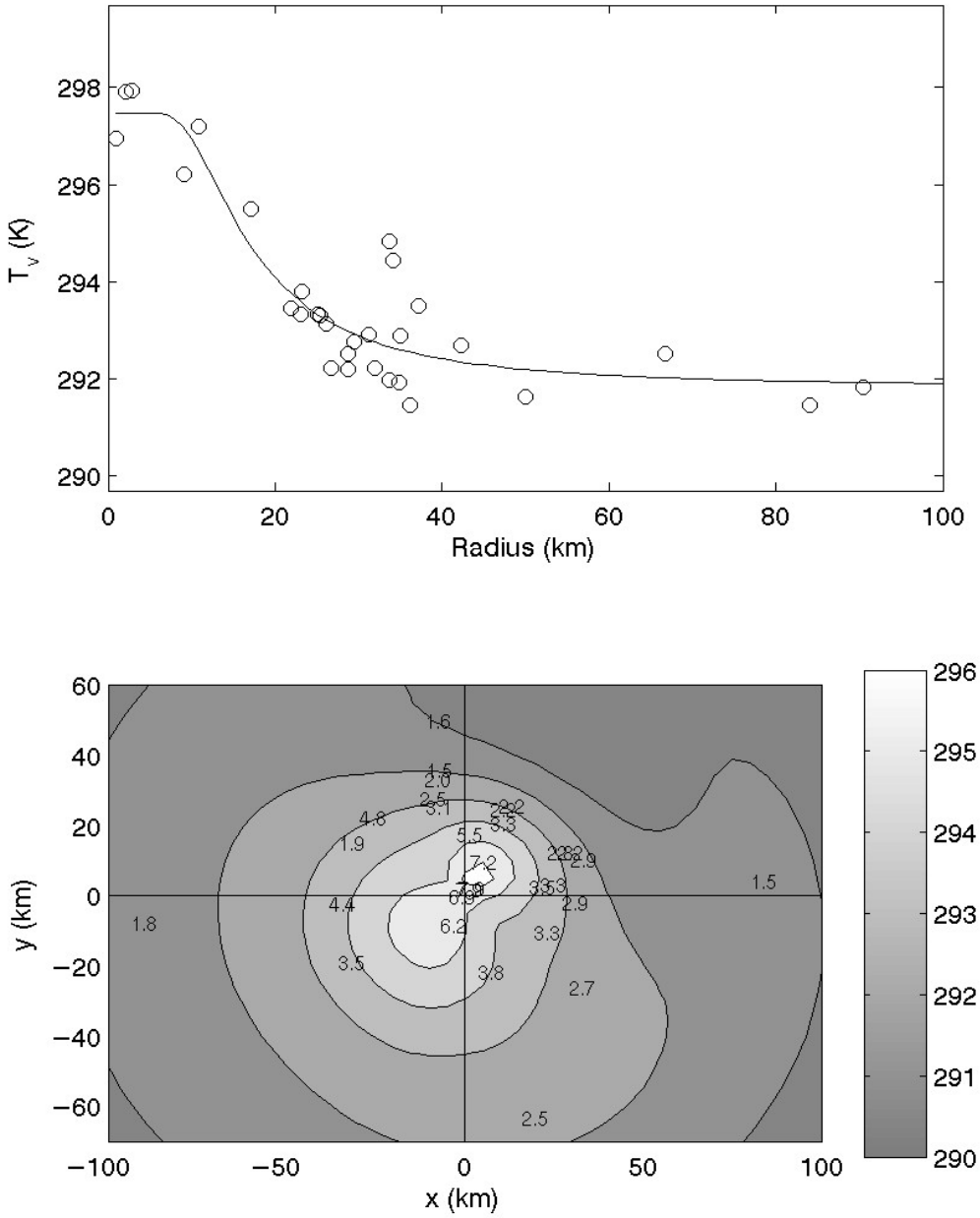

Figure 4.40 Top: Observed virtual temperature at 800 hPa in Hurricane Mitch as a function of radius, together with fitted radial profile. Bottom: Objective two-dimensional analysis of the same data, showing the asymmetry with warm temperatures to the southwest. The plotted figures are the observations with 290K subtracted and the contour interval is 1 K.

These fitted curves were differentiated with respect to radius, and the temperature gradients so obtained used to adjust each temperature soundings to a constant radius. The hydrostatic equation was then integrated, and the resulting profiles of height as a function of pressure were assigned to the location and time of the hydrostatic anchor point. This was the splash position, except for two cases when this was not available and the aircraft geopotential altitude and pressure were used instead.

As a consistency check, downwards integrations, using the aircraft height and pressure (corrected for the radius change) as the boundary condition, were also carried out to estimate a surface pressure. The difference between this and the splash pressure had a mean of 0.3 hPa and standard deviation of 1.6 hPa, with values ranging from −4 to 3.5 hPa. This is therefore substantially better agreement than given by the slant integrations, and shows that the correction of the soundings for slant effects is valid.

4.3.4.1 Gradient-Wind Equation I: Pressure Analysis

The pressure form of the Willoughby profile was fit to the pressure-height data obtained from the hydrostatic integrations, at every 100 m from the surface to 3 km. The vertical profiles of the fitted control parameters are shown in Fig 4.41. The fitted amplitude of the second outer exponential, v_{m2}, was found to be zero at all levels. This is in contrast to the situation in Georges, which had a relatively "flat" wind profile much outside the RMW. The other parameters have reasonably smooth vertical consistency, as well as a physically plausible variation with height. In particular, the maximum gradient-wind speed decreases with height, and its radius increases, as it should in a warm-cored vortex. The value of the cost function also decreases with height, at a rate that is consistent with the pressure error being proportional to pressure, rather than constant. As discussed earlier in the case of Hurricane Georges, this is possibly a

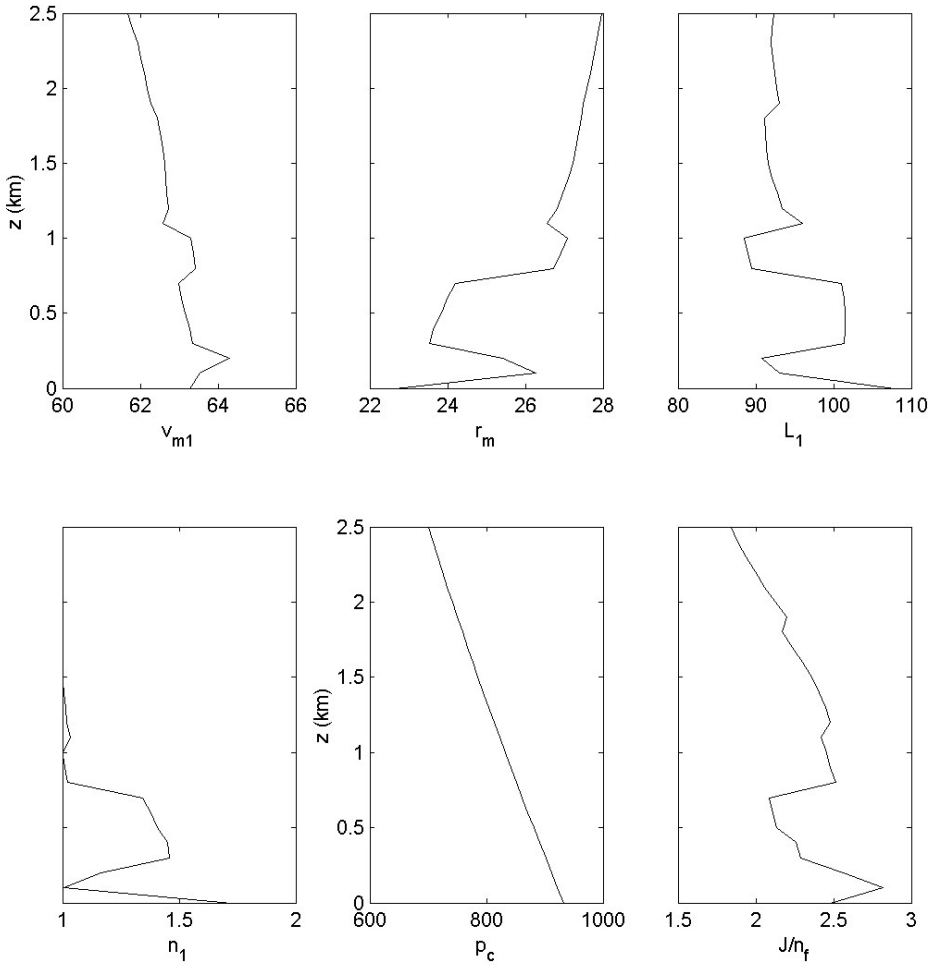

Figure 4.41 Vertical profiles of control parameters for fits of the Willoughby parametric pressure profile in Hurricane Mitch.

reflection of the bulk of the error being representational; that is, due to small-scale features or asymmetries not resolved by the analysis.

The data and fitted curve are shown for three representative levels in Fig 4.42, together with the observed storm-relative azimuthal winds and gradient-wind speed. It is apparent that the majority of the near-eyewall wind observations are substantially greater than the gradient-wind; that is, that the flow is supergradient. This imbalance exists from about 400 m to over 2-km height[6], and is strongest at 700 m, where the average difference between the storm-relative azimuthal observations and the gradient-wind, over the 15 to 40 km annulus, is 10 m s^{-1}.

The analysed pressure profiles necessarily contain errors. It is desirable to estimate these, and hence the gradient-wind error, to determine whether the observed winds are significantly different, in a statistical sense, to the gradient-wind. While it is in principal possible to do this analytically, it would be difficult because the fitted pressure profile must be differentiated to calculate the gradient-wind. Thus, to correctly propagate the analysis errors, it would be necessary to know not just the pressure analysis-error at any point, but also its spatial correlation. Even then, the inherent nonlinearities would make the calculation very cumbersome. The nonlinear nature of the problem would also make determining the probability distribution of the gradient-wind analysis errors and the interpretation of the usual statistical tests for difference difficult.

[6]It is difficult to define the top of the layer of supergradient flow, as the observed winds tend smoothly back to the estimated gradient-wind, a little above 2 km. However the flow appears to be still weakly supergradient at this level.

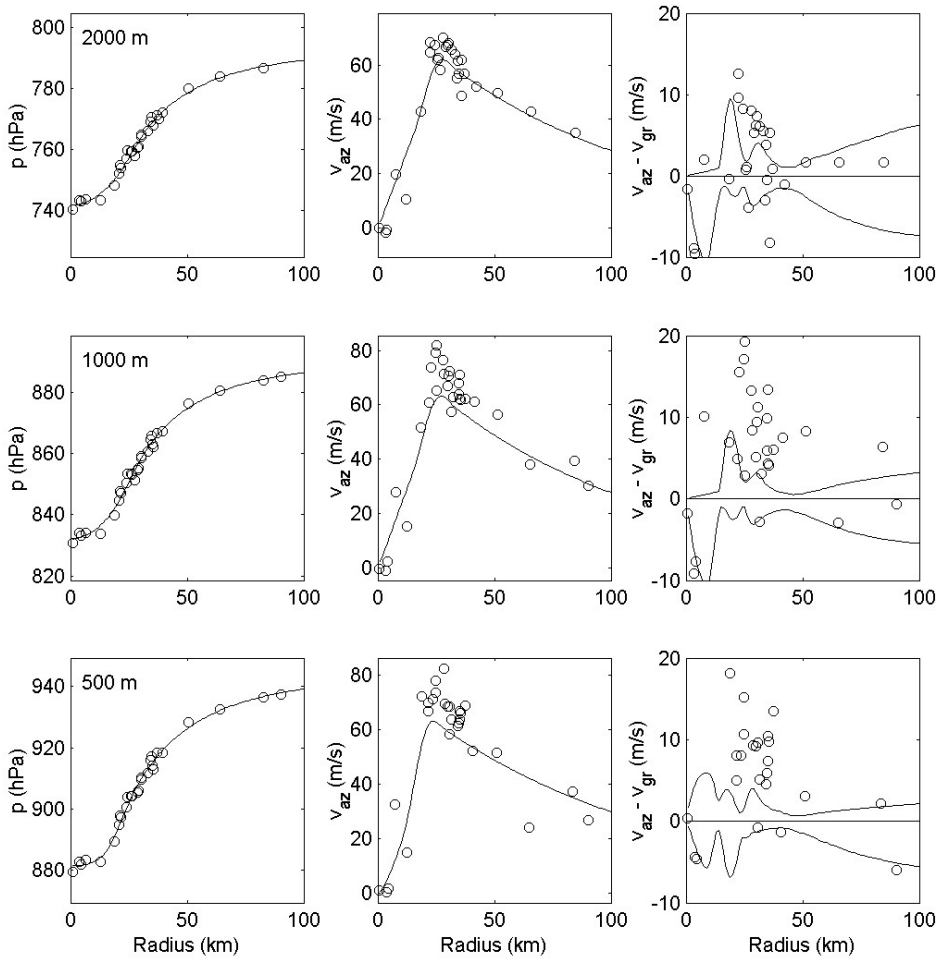

Figure 4.42 Left column: Dropsonde pressure observations at 2 km (top), 1 km (middle) and 500 m (bottom), together with fitted profiles. Middle column: Gradient-wind calculated from the pressure analyses, together with observed storm-relative azimuthal wind. Right column: Difference between wind observations and the gradient-wind, together with the 5th to 95th percentile confidence interval about the gradient-wind.

Thus a Monte-Carlo technique was adopted. The observations were perturbed with independent normally distributed noise with a zero mean and standard deviation of 1 hPa, and the curve fitting performed. This was done two hundred times at each 100-m height level, and the 5th and 95th percentiles of the resulting pressure and gradient-wind found at every 1 km of radius from the centre to 100 km. Confidence intervals were used, rather than a calculation of means and standard deviations, to avoid having to make assumptions about the distribution of analysis error. The confidence bands are included in the right column of Fig 4.42. It is clear that the wind observations lie well outside the gradient-wind confidence band at 500 m and 1 km – indeed, this is true from 400 m to 2 km. Thus we can conclude that the apparently supergradient flow is unlikely to be the result of chance, but is real.

The pressure residuals (that is, the difference between the observations and the fitted values), were carefully examined to check that there was no systematic variation with time, azimuth, or radius. The residuals from the lowest 600 m showed a variation with time of about 1 hPa/hr, which is consistent with the NHC estimated weakening rate at the time of 0.83 hPa/hr. Interestingly, this trend was not found at higher levels. Otherwise, there was no significant azimuthal or radial variation in the residuals.

4.3.4.2 Gradient-Wind Equation I: Wind Analysis

The Willoughby wind profile was fitted to the observed storm-relative azimuthal winds every 100 m from 100 m to 3 km. The vertical profiles of the fitted parameters are shown in Fig 4.43; note that in contrast to the pressure fits v_{m2} is generally non-zero. There was insufficient data to reliably fit L_2, and so it was held fixed at 500 km. While there is substantial noise in the profiles of v_{m1} and v_{m2}, their sum varies smoothly with height. Note also that the RMW increases steadily with height, and the maximum wind has a broad maximum between about 300- and 700-m height.

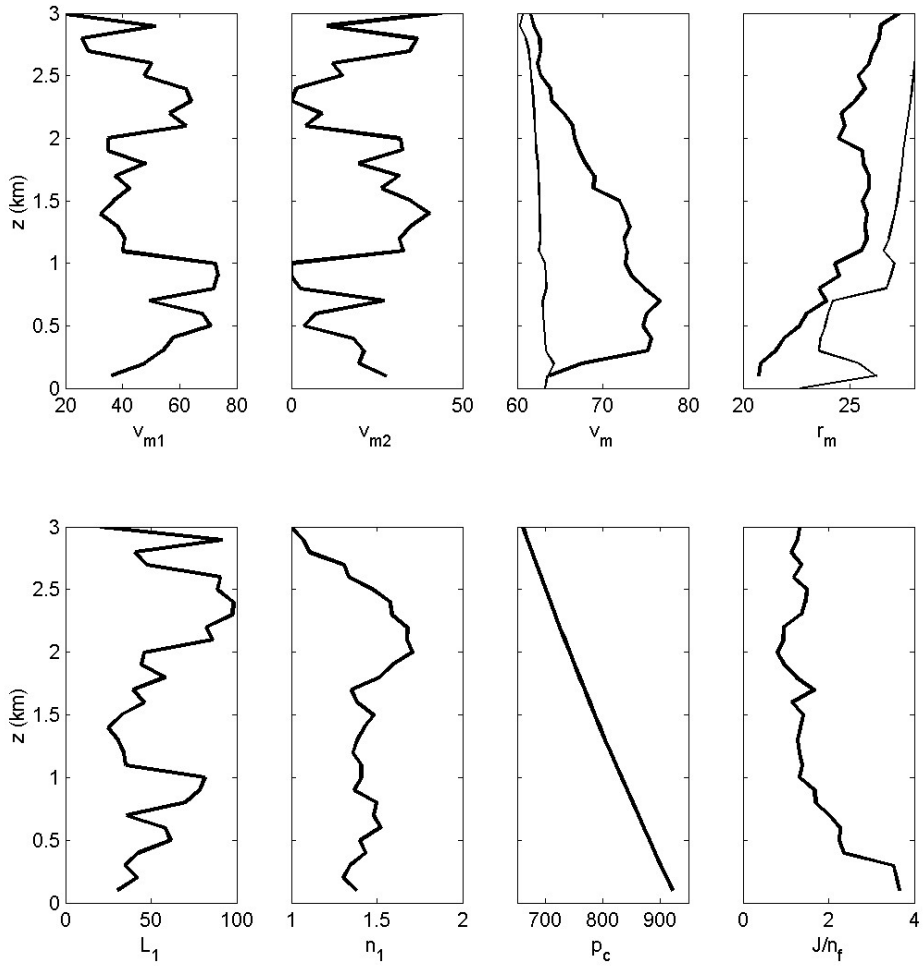

Figure 4.43 Parameters describing the fits of the Willoughby wind profile to the Mitch storm-relative azimuthal winds (heavy lines). From top left: v_{m1}, v_{m2}, maximum wind, radius of maximum winds, L_1, n_1, p_c and goodness of fit. The maximum wind speed and RMW panels also include these parameters from the pressure fits (light lines).

The residuals to these fits were examined for systematic variation. It was found that an azimuthal wave-number one pattern existed. This had amplitude about 7 m s^{-1} near the surface, decreasing to 3 m s^{-1} between 1 and 2 km, before increasing to 6 m s^{-1} at 3 km. The positive residuals were to the west at the surface, and rotated anticyclonically by about 70° km^{-1} with height. This is thus a reflection of the wind asymmetry already discussed.

The radial integration of the gradient-wind equation, to form a pressure profile, requires a boundary condition. This was chosen to be the mean pressure within 15 km of the hurricane centre. The wind observations and fitted curve together with the pressure observation and gradient pressure profile for the same three representative levels are shown in Fig 4.44. It is apparent that the gradient-wind integration leads to pressures near and inwards of the RMW which are substantially below those observed at the lower two of the levels shown. Thus, the flow is supergradient at these levels, at some radii. In fact, supergradient flow is diagnosed to occur in a similar height range, to that found in the previous subsection[7].

Confidence intervals for the fit were estimated by a similar Monte-Carlo technique. The wind observations were perturbed with random noise drawn from a normal distribution with zero mean and standard deviation of 4 m s^{-1}. Confidence bands were defined as lying between the 5th and 95th percentiles of the 200 curves, as before, and are also shown in Fig 4.44. Clearly, the diagnosis of supergradient flow is statistically

[7]Assigning boundaries is again somewhat subjective since the flow returns smoothly to gradient balance in the upper part of the domain. However, it is clearly supergradient at 300 m, and is at most only weakly supergradient above 1.6 km.

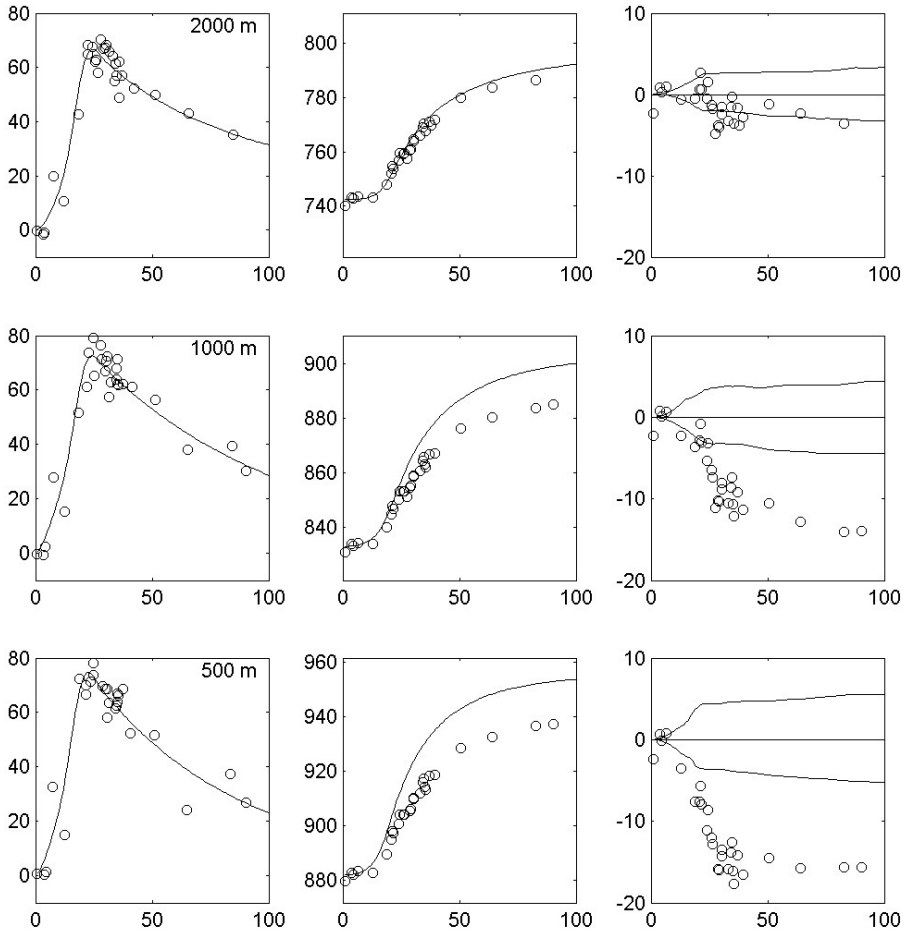

Figure 4.44 Fits of the Willoughby wind profile at 2 km (top), 1 km (middle) and 500 m (bottom), to dropsonde storm-relative azimuthal winds in Hurricane Mitch. Left: Observed and fitted winds. Middle: Pressure observations and gradient pressure curve. Right: Differences between the gradient pressure and observations, together with the 5th to 95th percentile confidence interval about the gradient pressure.

significant, to at least the 95% confidence level[8].

As a final illustration of the imbalance, the vertical profiles of fitted r_m and v_m as found by both the pressure and wind fits, together with their confidence intervals, are shown in Fig 4.43. The radius of maximum winds found by the wind fits is always less than that for the pressure fits, most significantly so near the surface, while the fitted maximum wind speed is 10 m s^{-1} greater for the wind fit, than the pressure fit, at and around 500 m. However, it is in agreement near the surface, and above about 2.2 km. This comparison thus confirms the presence of supergradient flow near the RMW over a substantial height range.

4.3.5 Model Simulations

Several experiments were performed with the numerical model to see how much of the observed flow could be reproduced. In these, the model was forced by a Willoughby (2002) parametric vortex with v_{m1} = 58.5 m s^{-1}, v_{m2} = 6.5 m s^{-1}, L_1 = 90 km, L_2 = 800 km, r_m = 25 km, n_1 = 0.9 and L_b = 10 km translating at 2 m s^{-1}. These are similar to the fitted values, apart from the addition of a small outer component with a long length scale to avoid inertial instability. The first experiment did not include the effects of land and showed a negligible asymmetry, so is not considered further.

The near-surface flow, and vertical velocity at 1-km height, from an experiment in which the cyclone approached a straight coastline behind which the land had a roughness length of 30 cm, at the moment when the land was 80 km away, are shown in Fig 4.45. Significantly enhanced inflow is apparent to the southeast, downstream of

[8]In fact, between 400 m and 1.1 km, none of the 200 Monte-Carlo fits produced as small a pressure drop from the outer core to the centre, as did the observations.

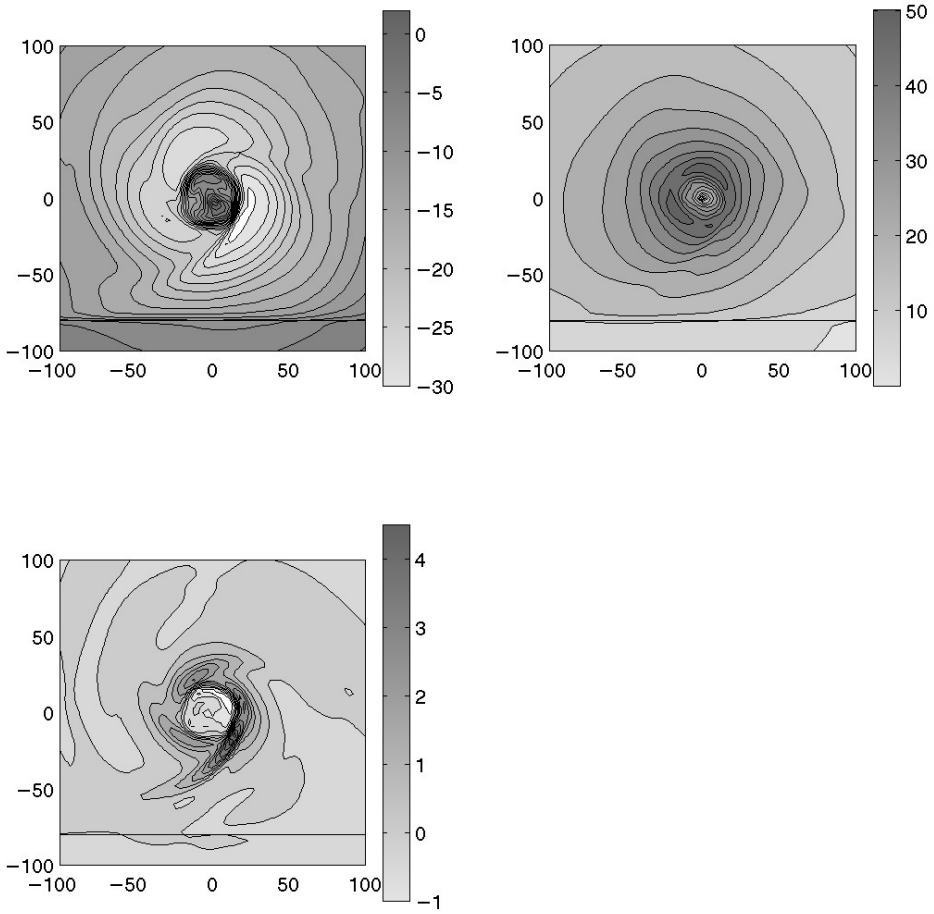

Figure 4.45 The simulated storm-relative 10-m radial (top left), 10-m azimuthal (top right) and 1-km vertical wind components for the model calculation of Mitch described in the text. The coastline is shown by the line at $y = -80$ km. Contour intervals are 2, 5 and 0.5 m s^{-1} respectively.

the rough land, with a wind speed maximum in the northeast eyewall, downstream of the enhanced inflow. The updraft is strongest to the southeast, and both it and the inflow show two additional weaker maxima near the eyewall. The enhanced frictionally forced updraft to the southwest is consistent with the strongest observed radar reflectivity being to the northeast, or downstream of this.

Comparisons of the dropsonde-measured azimuthal and radial wind profiles, and those from this model calculation, are shown in Figs 4.46 and 4.47 respectively. The level of agreement is quite good. The transects ABCD and EFGH are well handled, with the main shortcoming being that the model-predicted structures have a shorter height scale than the observations. Good agreement between model and observations is also found to the west of the storm, but there is little agreement to the south of the storm. To the east, the inflow component in profiles O to T is generally underpredicted, and the azimuthal component not in good agreement.

The level of agreement, while less than perfect, is encouraging. A substantial part of the observed wind asymmetry is reproduced simply by including an area of enhanced friction, representing land, in the model. The modelled vertical velocity field is also consistent with the strongest convection, once allowance for downstream advection is made. Earlier, it was noted that the observed wind asymmetry had structural similarities with the motion-induced frictionally stalled inertia wave discussed in previous chapters. It seems that asymmetric friction, due to the proximity to land, is indeed generating similar structures here.

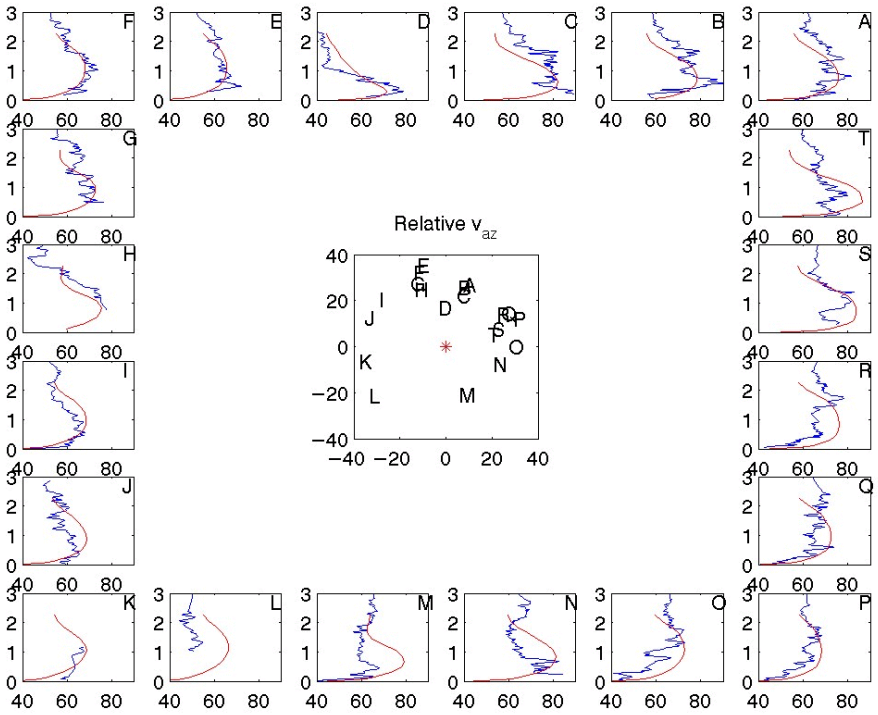

Figure 4.46 Profiles of storm-relative azimuthal wind in Hurricane Mitch for 20 near-eyewall dropsonde observations (blue), together with simulated flow from the model calculation described in the text (red).

4.3.6 Discussion

At the time of the observations analysed here, Hurricane Mitch was moving slowly southwards, and exhibited significant asymmetries. The southwest flank had a weak or absent updraft and an absence of strong convection, while the opposite prevailed to the northwest. The pressure centres tilted to the NNE with height, while the warm core was displaced to the southwest. The temperature asymmetry was presumably due to subsidence, and is hydrostatically consistent with the vortex tilt.

Tracks were fit to both the aircraft pressure-height, and dropsonde "splash" pressure data, and used to convert all observations to storm-relative coordinates.

Azimuthal mean storm-relative winds were calculated in several annuli and showed a marked low-level wind maximum in the vicinity of the RMW. This was stronger, and closer to the surface, on the inner side of the RMW than on the outer. Very strong shear existed above the low-level maximum, particularly on the inner side of the RMW. The wind asymmetry near the eyewall was similar in structure to the frictionally stalled inertia wave found to be the dominant motion-induced asymmetry in the modelling chapters. However, its phase appeared to be determined by the proximity to land, rather than by the motion.

Analysis of the surface-wind factor showed a tendency to increase towards the centre of the storm, in agreement with the models. The asymmetry was of azimuthal wave-number two, with maxima to the west and east of the storm, and is distinct to that found in the theoretical studies, presumably because it is not dominated by motion here.

Gradient-wind balance was diagnosed in two ways, by differentiating a pressure analysis to calculate the gradient-wind speed and comparing this to the observations, and

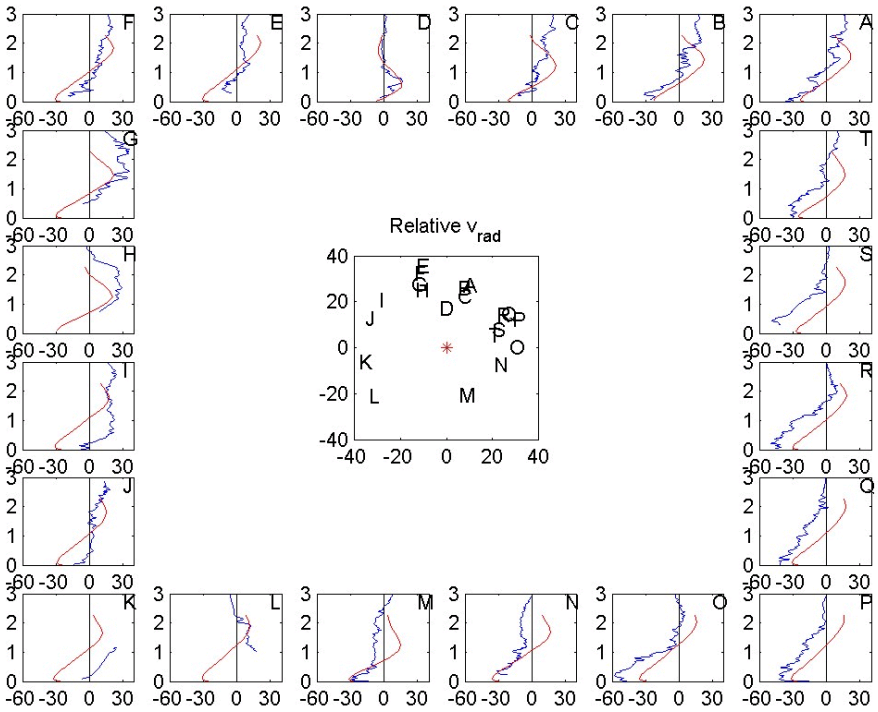

Figure 4.47 Same as Fig 4.46, but for the storm-relative radial flow component.

by radially integrating the gradient-wind equation using a wind analysis, and comparing the resulting pressure field to the pressure observations. The results in either case were quite consistent; that the flow was supergradient between about 300 m and 2 km, with the imbalance being largest near 500 m altitude, where it reached 10 m s^{-1}.

The very prominent low-level maximum on the inner edge of the RMW could be regarded as being due to the tendency for the dropsondes to fall towards the inwardly sloping RMW. While this explanation is not incorrect, it tends to obscure the dynamics of what is happening. Above the boundary-layer, the RMW in hurricanes is well known to tilt with height. The flow seems to be very close to gradient balance, and the tilt can be explained using the Eliassen balanced vortex theory for the response of a balanced baroclinic vortex to thermal forcing (e.g. Willoughby 1995). However, the azimuthal mean wind profiles shown suggest that there was in Mitch a very pronounced inward bending of the strongest winds in the lowest kilometre. As this is where the warm core is the weakest, the tilt cannot be due to the baroclinic effect, but rather is the processes described earlier in this thesis, which produce a strong gradient in the height of the supergradient jet across the RMW.

The numerical and analytical models developed earlier each produced an inwards tilt of the RMW towards the surface. The dropsondes near the RMW tend to report steadily increasing winds in the first part of their fall, which is qualitatively consistent with thermal wind effects, and with them moving closer to the sloping RMW. However, close examination of Fig 4.32 shows that there is an increase in observed mean shear immediately above the low-level maximum. This increase in shear as the dropsonde falls, before it encounters the maximum, is particularly apparent in the average over the 15- to 25-km annulus, but can be seen also in the 25- to 40-km annulus. It cannot be explained by thermal wind effects, because the warm core weakens towards the surface.

While it is still consistent with the sonde “falling into the eyewall”, it must be recognised that the lower part of the eyewall tilt is predominantly frictionally forced. Simply describing the low-level wind maximum as the consequence of a dropsonde launched a little in from the eyewall, inevitably falling through it, fails to acknowledge the role of frictionally forced inflow in the details of the near-surface dynamics, which include supergradient flow, markedly different wind profiles on either side of the RMW, and an inwards slope of the RMW near the surface.

The numerical model was used to simulate a cyclone with structure similar to Mitch, as it approached land. Agreement between the observed and modelled winds was quite good, and it appears that the observed large asymmetries in Mitch can be explained by asymmetric friction due to the proximity to land.

4.4 Hurricane Andrew

Hurricane Andrew devastated Miami on the morning of 24 August, 1992. After crossing the Florida peninsula, it re-intensified in the Gulf of Mexico, before making landfall again in Louisiana. Damage in the United States was estimated to be near $25 billion, making Andrew the most expensive natural disaster in U.S. history. Andrew was also directly responsible for 15 deaths in Florida, 8 in Louisiana and 3 in the Bahamas.

Andrew has been very extensively studied and only a very brief summary will be given here. Further detail may be found in Rappaport (1992a, 1992b, 1993), Mayfield et al. (1994), Wakimoto and Black (1994), Powell et al. (1996), Powell and Houston (1996), and Willoughby and Black (1996). Moreover, Andrew continues to attract attention. Recently, on the 10th anniversary of its landfall in Florida, its estimated intensity at that landfall has been upgraded from category 4 to 5 on the Saffir-Simpson scale (Landsea, 2002).

Hurricane Andrew was a Cape Verde Hurricane, and formed from a tropical wave that crossed the African west coast on 14th August 1992. The NHC best track is shown in Fig 4.48. It became a tropical depression on the 16th, and was named on the 17th. Andrew then continued its generally west- to northwest-ward track across the Atlantic as a relatively weak system. A period of rapid intensification which began on the 22nd as the environment became more favourable, saw Andrew's central pressure drop from 1000 hPa to 922 hPa in 42 hours, while it accelerated to the west. Andrew made two landfalls in the Bahamas, late on the 23rd and early on the 24th, as a category 4 hurricane, and weakened slightly. However, a rapid re-intensification during the last few hours before its landfall in Florida gave it an estimated central pressure of 922 hPa at landfall in Miami.

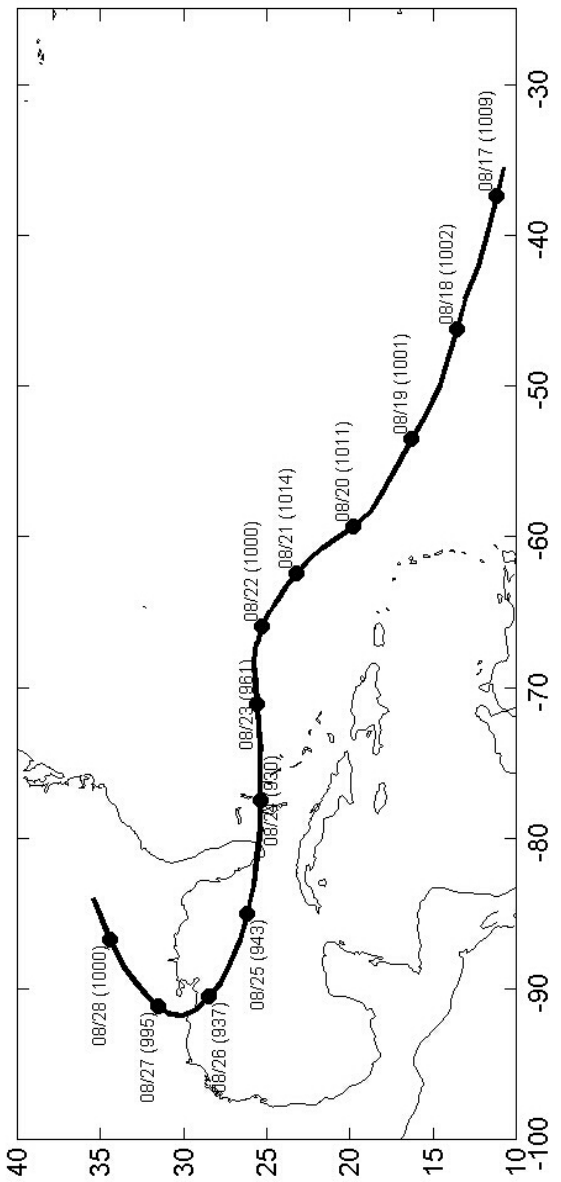

Figure 4.48 Best-track analysis of Hurricane Andrew by the National Hurricane Center. Tick marks are at 00UTC daily, in the format month/day (central pressure).

Andrew took about four hours to cross the southern part of Florida, during which time it weakened, but was still a major hurricane when it entered the Gulf of Mexico. Andrew turned gradually northwest, slowed and intensified, before making landfall on the south-central Louisiana coast on the morning of the 26th. It then weakened rapidly as it moved inland.

Powell et al. (1996) and Powell and Houston (1996) discussed the wind observations from surface platforms and aircraft in considerable detail. A substantial effort was devoted to post-calibration of anemometers, quality control of data, and the adjusting of land-based observations to a common exposure, height and averaging period. They included two tables of surface wind observations in and around Miami for which there were nearly co-located aircraft observations (from a height of about 700 hPa). The location of these observations, together with Andrew's track, are shown in 4.49. Surface-wind factors from these tables were stratified according to whether they lay to the left or to the right of the track, and are plotted as a function of distance from the storm centre in Fig 4.50. It is apparent (i) that there is an increase towards the centre of the storm, (ii) that the values are significantly higher on the left of the track than on the right, and (iii) that the highest observed values, of 0.97 and 1.03, occurred in the left eye-wall.

The increase towards the centre, left-right asymmetry, and values of near one in the left eye-wall, are all in strong agreement with the modelling work described in previous chapters. However, it should be noted that this is not an ideal comparison, as a mix of stations with marine and land exposures[9] were used. This issue is probably most

[9]Powell et al. (1996) had adjusted observations with land exposure to the WMO measurement standard of an anemometer height of 10 m and a roughness length of 3 cm,

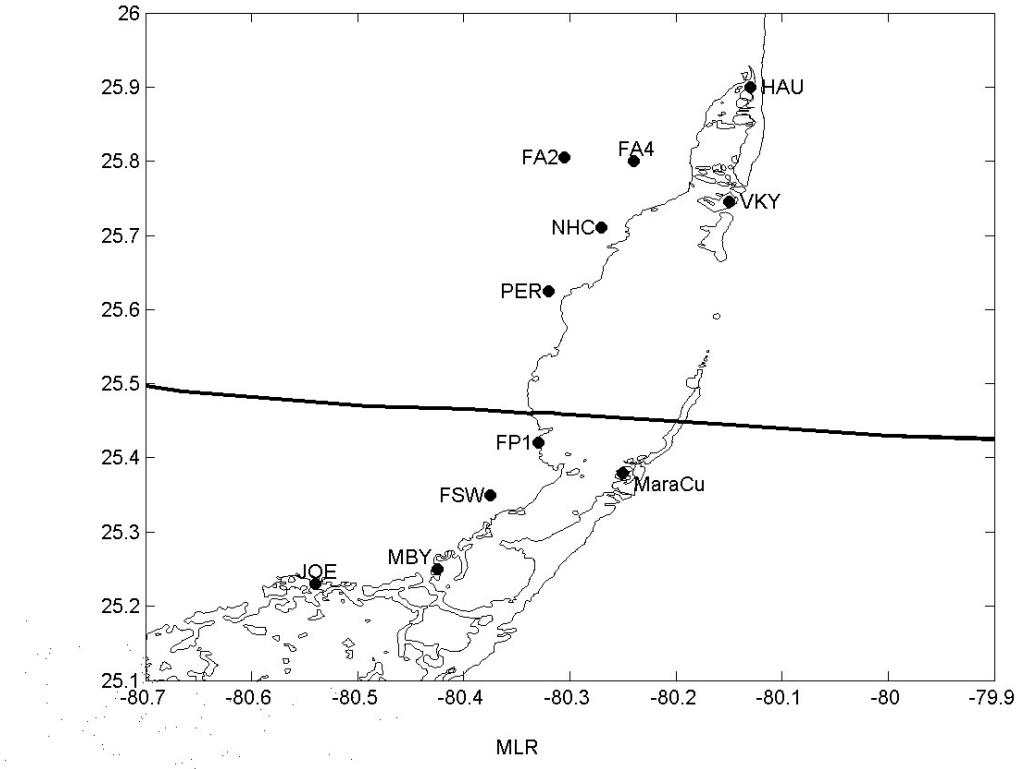

Figure 4.49 The track of Hurricane Andrew at landfall in Florida on August 24, 1992, together with the locations of surface observations used in the analysis here.

indicating flow over grass.

serious to the left of the track, where the flow was off-shore. Apart from the small-scale issue of anemometer exposure, there is also the larger-scale problem that the proximity to land induces a substantial frictional asymmetry, superimposed on that due to motion. This may be expected to produce an asymmetric flow in the cyclone similar to that caused by motion, as discussed for Hurricane Mitch. However, the situation is more complex here, since the motion-induced asymmetry would be expected to be larger, and the much more rapid approach to land means the land-induced asymmetry will have relatively less time to develop.

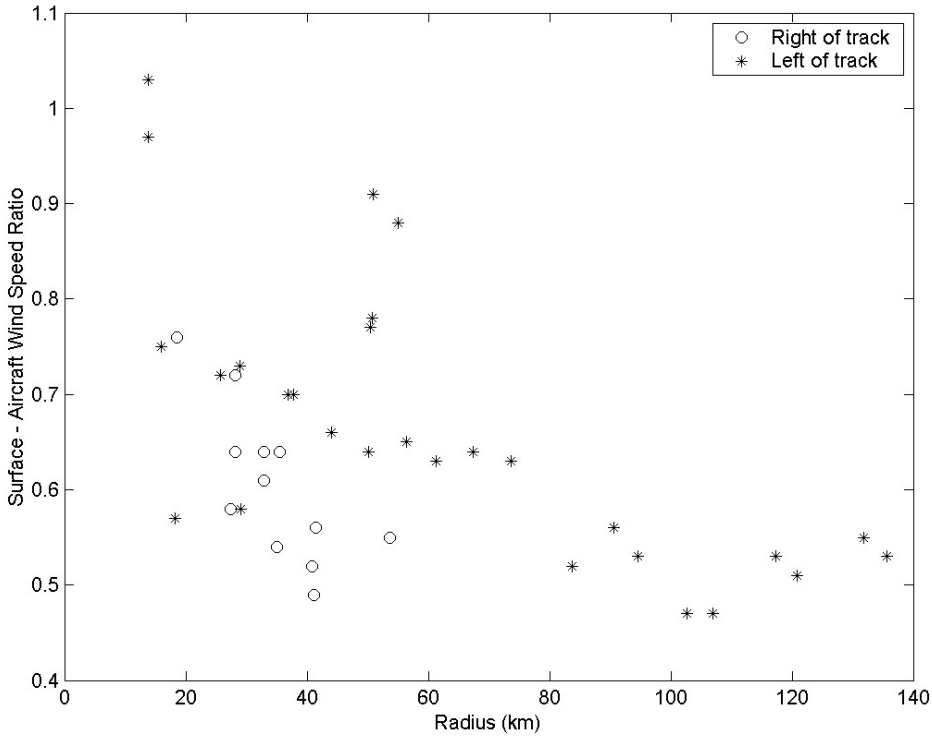

Figure 4.50 Observed ratio of the surface and flight-level wind speeds in Hurricane Andrew at landfall in Miami, as a function of distance from the storm centre. Circles and asterisks are for points to the right and left of track, respectively. Data from Tables A2 and A3 in Powell and Houston, 1996.

4.5 Hurricane Hugo

Hurricane Hugo was another Cape Verde Hurricane, whose track is shown in Fig 4.51. At landfall near Charleston, South Carolina, on the 22 September 1989, it was the most intense storm to strike the United States for 20 years. Powell et al. (1991) presented detailed analyses of the wind at the surface and flight-level during landfall. They also included a table of surface-wind observations for which there were nearly co-located aircraft data. Surface-wind factors derived from these data are shown in Fig 4.52. For those sites with land exposure, the SWF increases with decreasing radius. This trend is most apparent for those points to the right of the track, and less obvious for those to the left. The largest two land-based values were reported in the onshore flow to the right of the track, after the storm had passed inland of the station.

The points in Fig 4.52 with marine exposure were derived from two surface stations, and neither was particularly close to the centre of Hugo. Values of around 0.6 to 0.7 to the right of the track are consistent with other marine studies and with the modelling work. The very large values of 0.99 and 1.21 to the left of track, in the offshore flow about 120 km from the centre 1.5 to 2.5 hours before landfall, are unexpected. The modelling work suggests values should be higher here than to the right, but not to this extent. Powell et al. (1991) point out the stratification here was probably more unstable than at the other marine exposure site, contributing to downward mixing of momentum. Radar imagery (their Fig 7) suggests that the higher value may have been affected by a convective rainband. Thus, the time difference of up to 1.5 hours between aircraft and surface observation, coupled with locally stronger winds near the rainband, may have contributed.

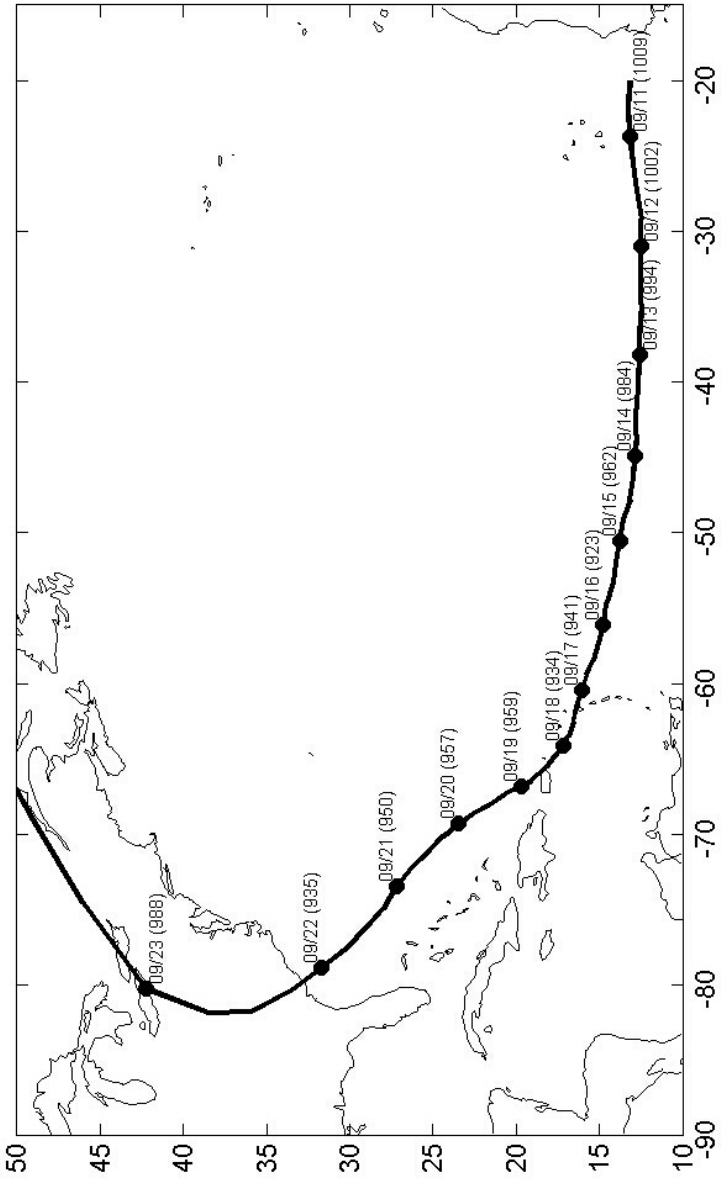

Figure 4.51 Best-track analysis of Hurricane Hugo of 1989 by the National Hurricane Center. Tick marks are at 00UTC daily, in the format month/day (central pressure).

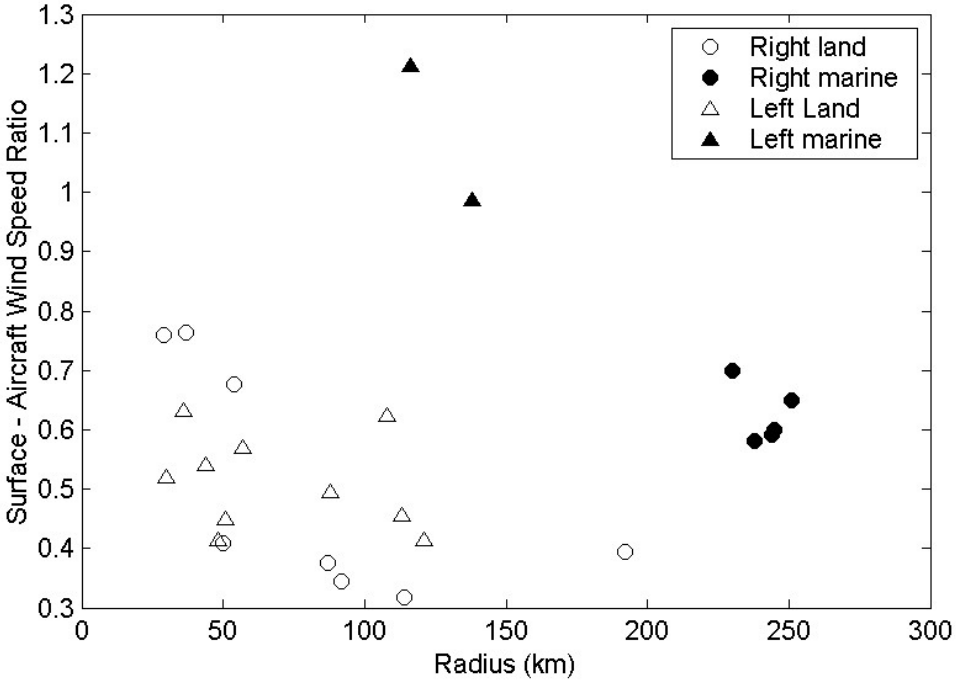

Figure 4.52 Observed ratio of the surface and flight-level wind speeds in Hurricane Hugo at landfall in South Carolina, as a function of distance from the storm centre. Circles and triangles are for points to the right and left of track, respectively, while filled and empty symbols denote data with a marine and land exposure. Data from Table 1 in Powell et al., 1991.

4.6 Severe Tropical Cyclone Vance

4.6.1 Introduction

Tropical cyclone Vance formed when a low within the monsoon trough, which had loitered within the vicinity of Darwin for several days, moved eastwards into the Timor Sea. It intensified steadily, reaching Category 3 late on 19th March 1999 and Category 5 a little over a day later, early on March 21st. The best-track analysis from the Perth Tropical Cyclone Warning Centre, and the locations of places mentioned here, are shown in Fig 4.53 and 4.54. While intensifying, Vance's track tended gradually from west-southwestwards, through the southwest to southwards, as it gradually recurved. On March 22nd it made landfall in Western Australia, the eye passing directly southwards down the Exmouth Gulf. A record wind gust for the Australian mainland of 74 m s^{-1} was recorded on the Dines anemograph at Learmonth, 35 km south of Exmouth, as Vance passed by. A substantial proportion of the buildings in Exmouth suffered wind damage, as did parts of the adjacent Navy and Air Force bases, although no lives were lost. There was also serious damage to essential infrastructure such as electricity and water supply. In addition, very high seas and storm surge caused severe beach erosion and damaged jetties in and around Exmouth, and beached three barges at Onslow. As Vance passed further southeastwards through Western Australia there was additional wind damage, and flooding cut the main transcontinental road and railway for several days.

Vance made landfall almost directly over the Bureau of Meteorology observational site at North West Cape (Kepert and Holland 1999). At the time, there was a 920 MHz wind profiler with RASS adjacent to Point Murat, and sonic anemometers were operating at the 42-m and 84-m levels of a nearby Royal Australian Navy communications tower. Data from the Bureau of Meteorology weather-watch radar at Cape Range showed that the instruments would have been under the eyewall on the

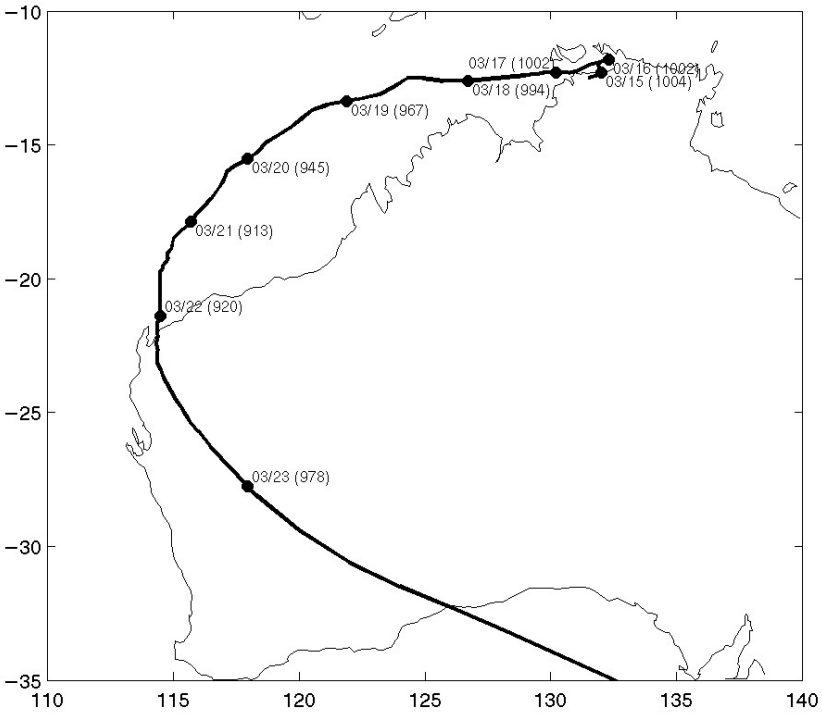

Figure 4.53 Track of Severe Tropical Cyclone Vance. Tick marks are at 00UTC, labelled month/day (central pressure). Post-season best-track analysis courtesy of the Bureau of Meteorology Tropical Cyclone Warning Centre in Perth, Western Australia.

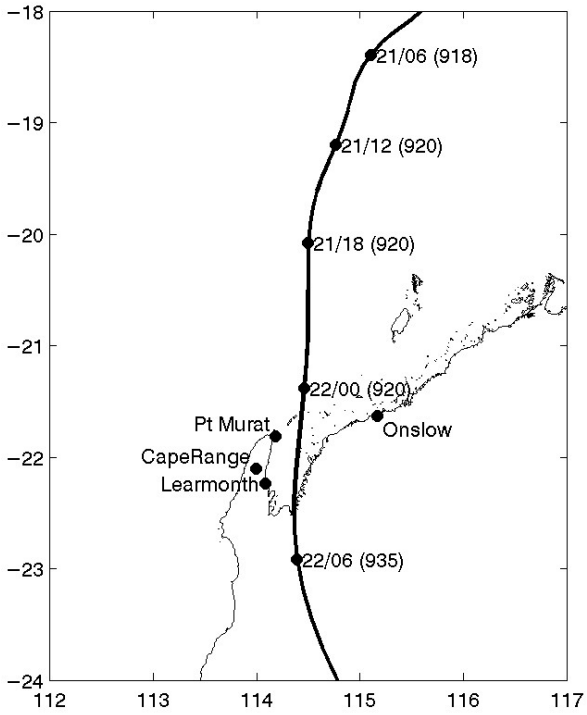

Figure 4.54 Detail of the track of Vance as it made landfall down the Exmouth Gulf, with 6-hourly positions in the format day/hour (central pressure), together with locations of the places mentioned in the text.

right-hand side of the storm for approximately an hour. Unfortunately, due to the destruction of an electrical switchboard, the wind profiler and sonic anemometers collected data only up until 2150 UTC, when the centre of Vance was some 100 km away.

Pressure and wind data from the Bureau of Meteorology observing station at Learmonth, along with 10-minute volumetric reflectivity scans from the weather-watch radar on Cape Range, were also obtained.

4.6.3 Mean Wind Data

The profiler wind data were consensus-averaged in 30-minute bins, and the horizontal components extracted. The sonic anemometers are known to be subject to producing noisy data, with frequent spikes, during rain. These erroneous data were removed and the winds averaged similarly. Both were processed into storm-relative coordinates using the best-track analysis.

Figure 4.55 and 4.56 shows the wind components, with the storm motion subtracted, in storm-centred cylindrical coordinate system. There are two maxima in the azimuthal wind, at heights of about 1500 m and 5 km, with both becoming apparent inwards of about 300-km radius. The first of these appears similar to the jet discussed earlier, since it is accompanied by strong inflow below, with weaker outflow above. Equation 2.24 gives an expression for the height of the jet in the linear theory. This is shown as the heavy curve in Fig 4.56 and is in reasonable agreement. For this calculation, the gradient-wind profile described in section 4.6.4 below was used to get the inertial stability. The drag coefficient was given by

$$10^3 C_D = 0.5 + 0.056 u_{42} \qquad \textbf{(4.9)}$$

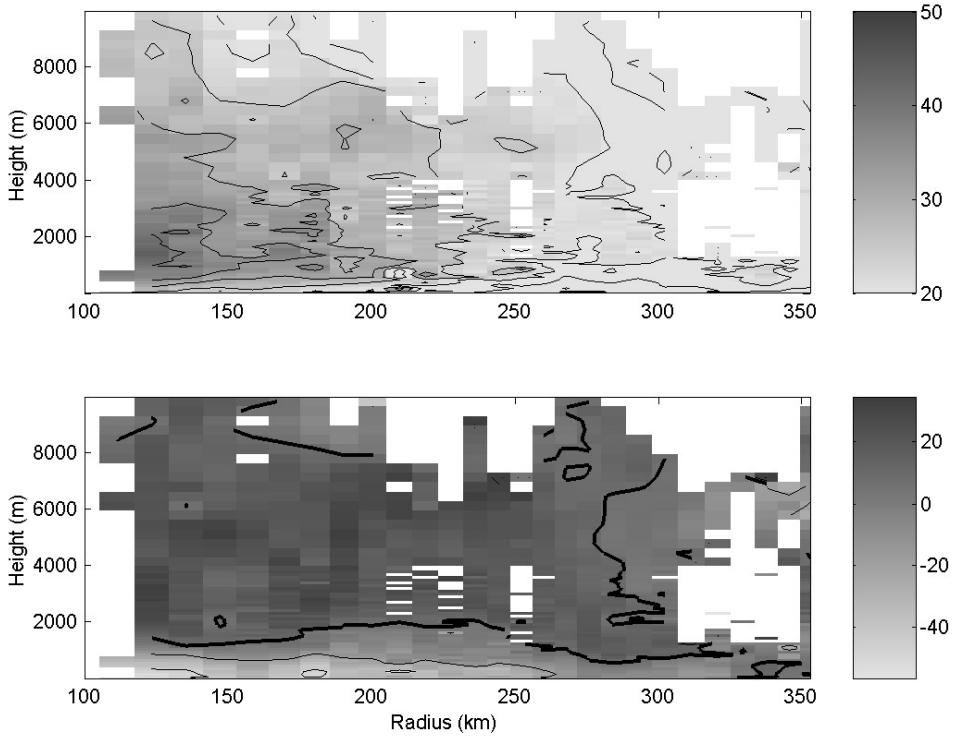

Figure 4.55 Radius-height section of storm-relative azimuthal (top) and radial (bottom) wind components from the profiler at Point Murat. Contour interval is 10 m s^{-1}, zero contour shown in bold.

applied to the measured 42-m winds. This formula was derived by adjusting Garratt (1977) to 42-m winds using a logarithmic profile. The turbulent diffusivity was given by

$$K = k\, u_* \, l_{mix} \qquad \textbf{(4.10)}$$

where l_{mix} = 250 m is a mean mixing length in the boundary-layer, k = 0.4 is von Kármán's constant and $u_* = u_{42}\, C_D^{1/2}$. While these parameterisations are somewhat arbitrary, they nevertheless lead to encouraging agreement with the theory.

The upper wind maximum lies immediately above the melting level in the predominantly stratiform rain deck. It may be the result of generation of potential vorticity within the rainband, as discussed by May and Holland (1999).

4.6.4 Gradient Balance Analysis

The surface pressure observations from Learmonth were navigated into storm-relative coordinates, and a Holland (1980) pressure profile of the form (4.15) fitted. The fitted values were v_m = 56 m s^{-1}, r_m = 30.5 km, b = 1.08, while p_c = 920 hPa was taken from the best-track analysis, and T_v = 298 K from the Learmonth observations. The observations and fitted curve are shown in the top panel of Fig 4.57. No data were available within 50 km of the centre of the storm, so the fitted profile probably underestimates the intensity there. With the lack of data near the eye, there was no need to get the details correct there for this analysis, and so the Holland profile was adequate.

Figure 4.57 also contains the measured radial profiles of storm-relative winds at all heights between 1 and 2 km, and the gradient-wind calculated from the Holland profile. For the latter, the cyclone was assumed to be barotropic. It is clear that the observed winds exceed the gradient-wind. A plot of the ratio of the observed to gradient

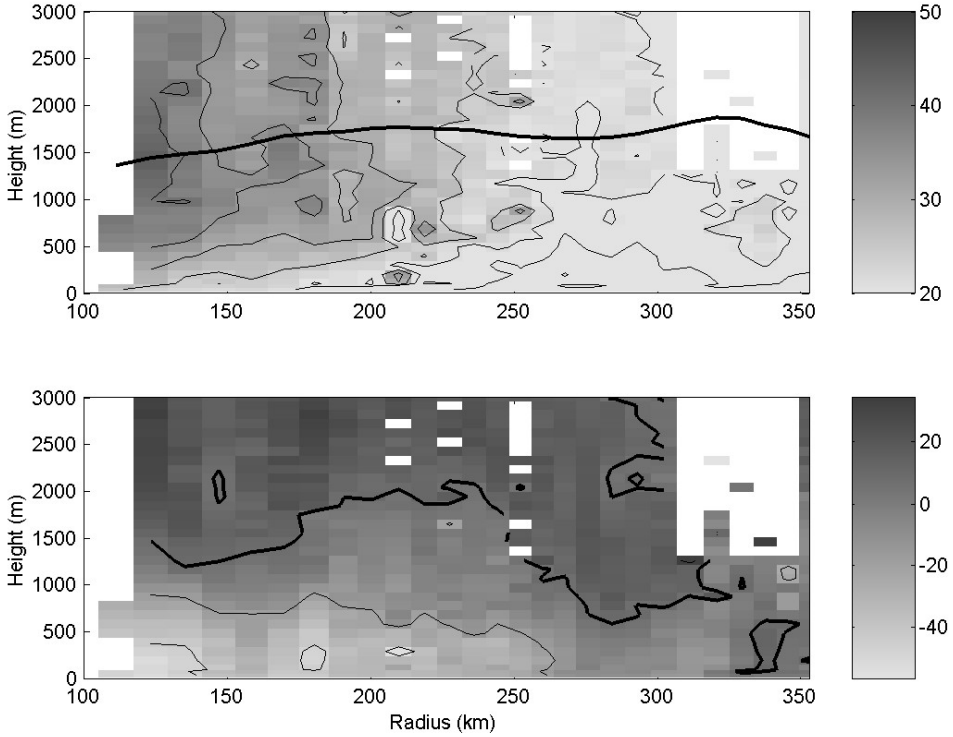

Figure 4.56 As in Fig 4.55, but only the lower 3 km shown, with a contour interval of 5 m s^{-1}. The heavy line in the top panel shows the jet height from the linear model, calculated as described in the text.

wind, at heights of 1 and 2 km, also included in Fig 4.57 shows that they are supergradient by up to 30%, although most are in the range of 10 – 20%.

Further, calculation of the inertial stability, either from the observed winds or the observed pressure, shows that Vance had a relatively flat wind profile with relatively high values of inertial stability away from the eyewall. This was shown to be conducive to a relatively widespread and less intense jet, and hence is in agreement with the occurrence of supergradient flow up to 300 km from the centre.

4.6.5 Surface-Wind Reduction

The spatial variation of the modelled surface-wind reduction factor (SWF) is given in Fig 4.58. Here, the value relative to the gradient-wind calculated above, and relative to the observed 1- and 2-km winds, are shown. The values are in the vicinity of 0.7, which is at the lower end of the range found in previous studies and earlier in this chapter, once the fact that the "surface" winds were measured at 42-m height is considered. A steady increase of the observed SWF is apparent inwards from about 280-km radius.

There is also a pronounced variation over a length-scale of approximately 50 km, or period of two hours. Examination of the individual time series (not shown) shows that the oscillation at 42 m is out of phase with those at 1 and 2 km. Part of this oscillation is visible in the upper part of Fig 4.56, as an intermittent jet maximum at about 700 m. These appear to not be boundary-layer rolls similar to those observed by Wurman and Winslow (1998), because of the long length. Possibly they are similar to the bands found by Gall et al. (1999), although the wavelength again seems long, unless they were crossing the site at a very acute angle.

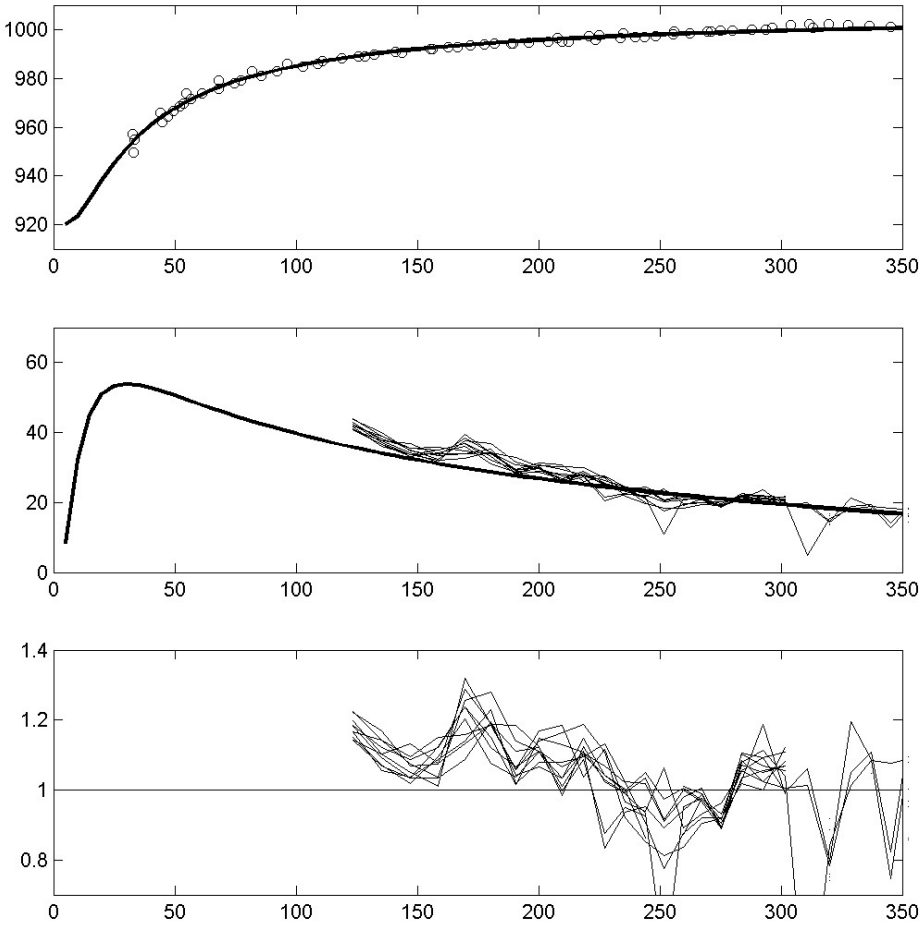

Figure 4.57 Top: Pressure observations from Learmonth (circles), together with fitted Holland profile. Middle: Gradient-wind speed (heavy curve), together with all profiler-observed storm-relative azimuthal winds between 1- and 2-km height (light curves). Bottom: Ratio of the observed storm-relative azimuthal-wind speed, to the gradient-wind speed, for all observations between 1- and 2-km height.

4.6.6 Modelling

The numerical model was run with forcing by the fitted Holland profile discussed above, and the motion from the best-track analysis. The predicted jet pattern is shown in Fig 4.59, and it can be seen that the jet ahead of the storm is expected to be about 15% supergradient, at a height of about 1500 m. These are in good agreement with the analysis of balance carried out above. A clearer comparison is provided by radius-height sections of the modelled winds, shown in Fig 4.60. Good agreement is apparent, except that the near-surface inflow is weaker, and the modelled 42-m wind speed about 10% stronger, than the observed.

This model simulation used the same Charnock coefficient of 0.011 to parameterise the surface roughness as elsewhere in this thesis. However, the flow at the profiler site would have been off the relatively shallow Exmouth Gulf, and with a restricted fetch. Thus a higher value is possibly more appropriate, and so the calculation was repeated with a range of different Charnock coefficients. The results for a value of 0.1 are shown in Fig 4.61. The jet is a little higher and stronger, and there is a significant increase in the near-surface inflow, and a reduction in the near-surface wind speed and consequently the SWF, improving the agreement with the observations.

4.6.6 Discussion

The modelled wind structure was in excellent agreement with the observations, once an increased surface roughness was applied. This included the winds being up to 15% supergradient in both observations and model[10], and a good match with the surface speed and inflow components. Thus the model captures the large scale features of the

[10]A stronger jet was predicted closer to the eyewall, but observations were not available there.

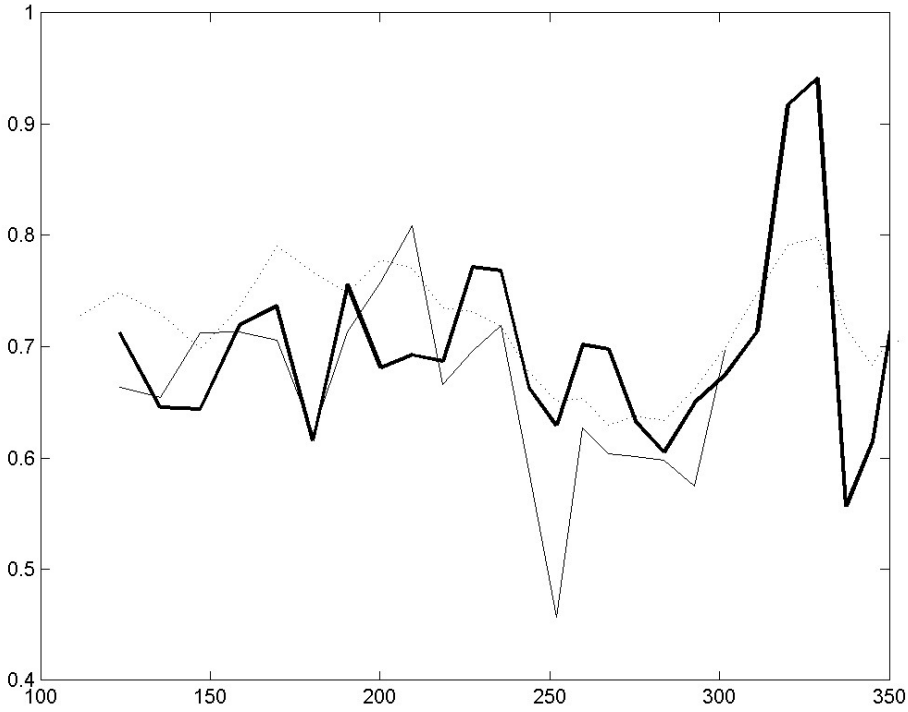

Figure 4.58 Observed surface-wind factors: The ratio of the 42-m wind speed to the 1-km wind (heavy line), to the 2-km wind (light wind) and to the gradient-wind (dotted line).

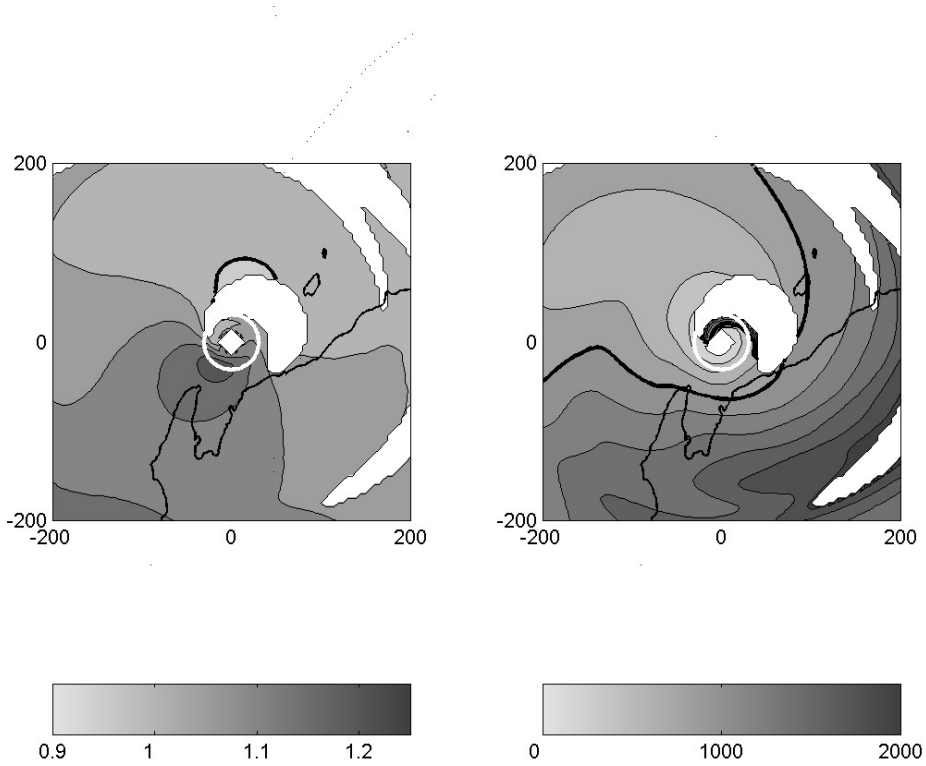

Figure 4.59 Modelled jet strength relative to the gradient-wind speed (left) and height (right) for Tropical Cyclone Vance. Contour intervals are 0.05 with 1.0 shown in bold (left) and 200 m with 1 km shown in bold (right). Unshaded areas are points where the strongest winds occurs at the model top level.

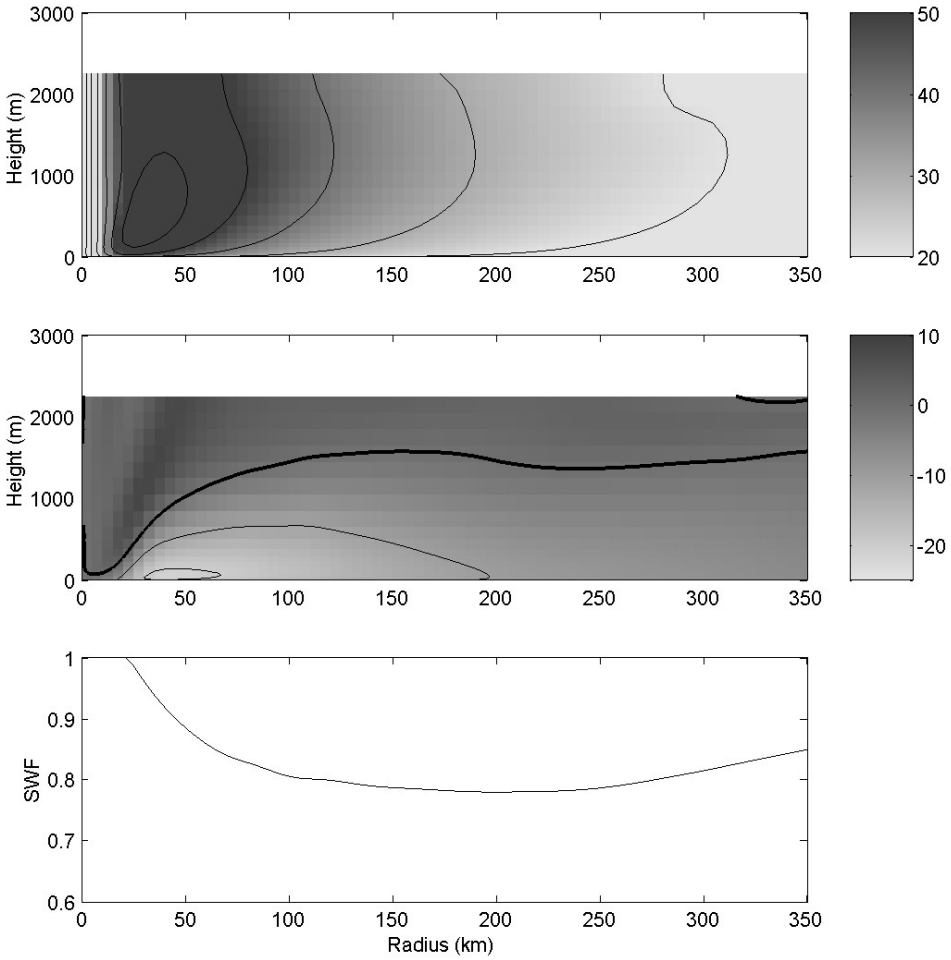

Figure 4.60 Radius-height sections ahead of the storm of modelled storm-relative azimuthal- (top) and radial-wind (middle) components. Contour interval is 10 m s^{-1}, zero contour shown in bold. Radial variation of the SWF; that is, the ratio of the 42-m earth-relative wind speed to the gradient-wind speed along the same radial (bottom).

leading part of Vance's boundary-layer very well.

Out-of-phase oscillations between near-surface and upper boundary-layer winds were also observed. Several cycles of the oscillation were observed. The wavelength of approximately 50 km seems to be too long for these to be boundary-layer rolls, and it is unclear what is causing this. They may be similar to the bands observed by Gall et al. (1999), with the apparently longer wavelength due to crossing angle.

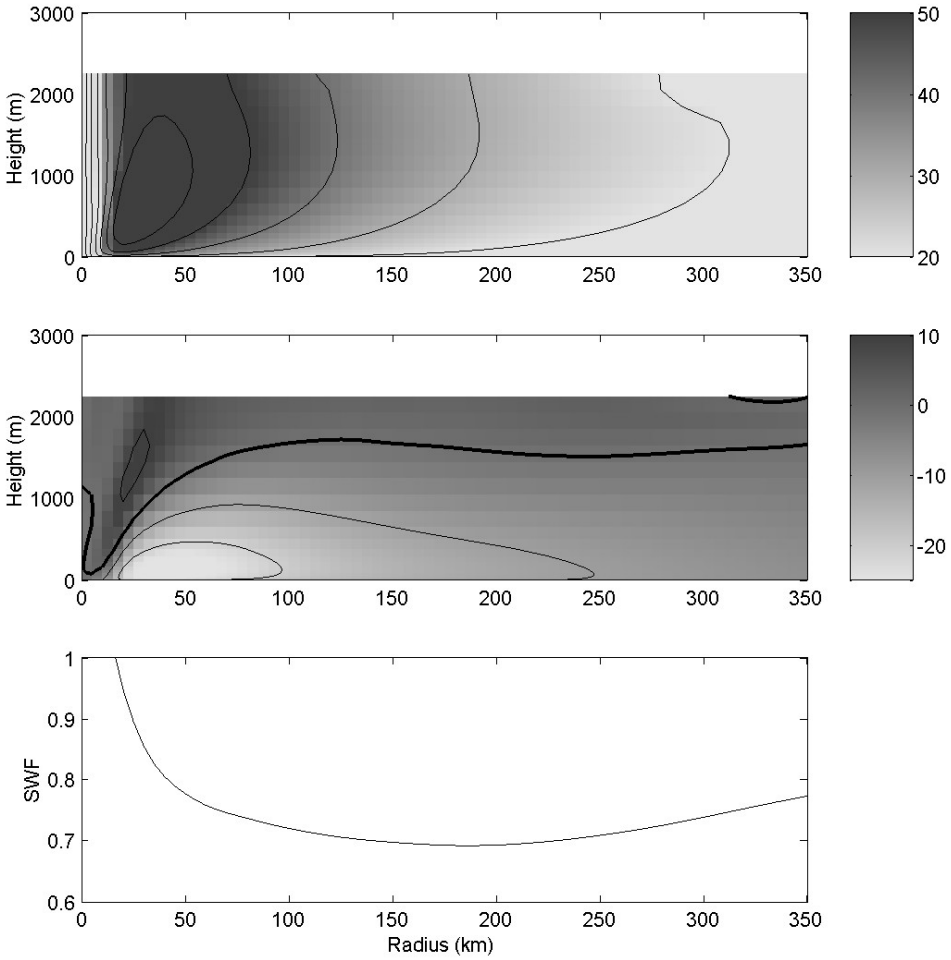

Figure 4.61 Same as figure 4.59, but Charnock coefficient increased to 0.1. Note the increased inflow and decreased azimuthal component near the surface, and decreased SWF.

4.7 Concluding Remarks

This purpose of this chapter was to test some specific predictions of the analytical and numerical modelling work against observations. Several points were identified for particular attention: (i) the radial and left-right gradients in the SWF, (ii) the supergradient nature of the upper boundary-layer jet (particularly near the eyewall), and (iii) the spatial variability of the jet strength and height. To this end, five case-studies of tropical cyclones were presented. All were towards the upper end of the intensity spectrum, but were otherwise quite different in character.

These analyses required accurate determination of the cyclone track, and a new technique was developed to objectively find the track from pressure observations. This produced similar results to wind-based algorithms, but was preferred as it was numerically more robust and was less affected by storm asymmetries. It was found that the slant trajectories of dropsondes produced some systematic biases in the analysis, which were quite severe for sondes released near the eyewall. These biases were removed by first correcting the dropsonde-measured virtual temperature profiles for their radial displacement, and then re-doing the hydrostatic integrations to determine the pressure-height relationship. This procedure substantially reduced the discrepancy between the upwards and downwards hydrostatic integrations which otherwise arose.

Each of the five case-studies yielded information on the SWF. Objective analysis of the dropsonde winds in Hurricane Georges yielded a pattern which was nearly identical to that found in the idealized modelling studies, with both the increase towards the RMW and the left-right asymmetry being readily apparent. A similar analysis in the slow-moving Hurricane Mitch showed an azimuthal wavenumber-two asymmetry, with a less clear increase towards the centre. The higher wavenumber asymmetry may have

been because the frictional asymmetry due to the proximity to land contained a significant component at this wavenumber, or because of nonlinear interactions.

Previously published data in Hurricanes Hugo (Powell et al, 1991) and Andrew (Powell and Houston, 1996) were used to plot the SWF as a function of radius, for points to the left and to the right of the track. It was found that the SWF increased with decreasing radius, and was higher on the left of track than on the right, in both storms. Both these trends are entirely consistent with the modelling work, although some caution is necessary in interpretation as the frictional asymmetry in these cases would have also included the effects of land. Finally, Severe Tropical Cyclone Vance did not have sufficient data to analyse the spatial variability, but was interesting because the observed values of the SWF were rather low. Experiments with the numerical model suggests that this may have been because the shallow water, and short fetch, were producing a greater surface roughness than would have normally been the case.

Hurricane Mitch was shown to have very marked azimuthal-mean supergradient flow in the eyewall above about 400 m, blending back to gradient balance around 2 km. At its peak near 800-m height the storm-relative azimuthal flow was about 10 m s^{-1}, or 15%, in excess of the gradient-wind speed. Confidence intervals were calculated by a Monte-Carlo technique and the gradient imbalance shown to be statistically significant to well in excess of the 95% level. This result was thus in strong agreement with the modelling predictions. In contrast, a similar analysis in Hurricane Georges showed that the flow at all levels was very close to being in gradient balance. The reason for the difference in not clear, but it was suggested that it may have been the result of larger-scale adjustment in the hurricane as it commenced an eyewall replacement cycle. The flow to the left front of Severe Tropical Cyclone Vance was also shown to be supergradient between 1 and 2 km above the surface, and from 120 to 220 km from the

storm centre. Simulations with the numerical model suggested that the observations were fortuitously near the azimuth of maximum supergradient flow in Vance.

In the eyewall of Hurricane Georges, the jet was stronger and lower to the left of the storm than the right, in excellent agreement with the theory. The radial flow component was similarly in good agreement, particularly in the phase relationship of the azimuthal and radial asymmetries. Simulations with the numerical model forced by a pressure field and motion representative of Georges showed remarkably strong agreement between model and observations. Thus it appears that a large part of the substantial variability between eyewall dropsonde wind profiles is due to the factors identified by the modelling work in this thesis.

The wind asymmetries in the eyewall of Hurricane Mitch were shown to be similar in structure to the "deep component" frictionally stalled inertia wave identified in Chapter 2. In particular, the asymmetries rotated anticyclonically with height, and the azimuthal and radial flow asymmetries were in quadrature, with the maximum azimuthal flow always downstream of the maximum inflow. However, they were almost 180^{o} in azimuth away from where motion-forcing would have placed them. It was suggested that as Mitch was slow-moving, and only about 80 km from land during the observation period, that frictional asymmetry due to land could have supplied a forcing similar to the frictional asymmetry due to motion. This idea was tested using the numerical model with an appropriately modified surface boundary condition, and it was shown that the simulated winds were very similar to the observations. Moreover, the frictionally forced updraft at the top of the boundary-layer was a maximum at the upstream end of a substantial convective eyewall asymmetry apparent on the radar imagery, so the asymmetric friction seems to have also been responsible for organising the eyewall convection.

The predictions from the modelling work are thus to a large degree supported. There seems to be a need for further work to determine whether Mitch or Georges represents the most common case, in terms of the presence of azimuthal-mean supergradient flow, and also to acquire sufficient data to analyse the flow further away from the eyewall.

Appendix 4.A: Some Mathematical Details

4.A1 The Holland Parametric Profile

Holland (1980) gives a parametric radial pressure profile which can be written in the form

$$p(r) = p_c + \Delta p \exp(-(r_m/r)^b) \qquad \textbf{(4.11)}$$

Here, p_c is the central pressure, Δp the pressure drop from the environment to the centre, r_m the radius of maximum cyclostrophic winds, and b a radial shape parameter. The maximum cyclostrophic wind v_m (assuming constant density ρ) is

$$v_m^2 = \frac{e\Delta p}{b\rho} \qquad \textbf{(4.12)}$$

where e is the base of the natural logarithms.

However, ρ does vary significantly with radius. For the lower tropospheric analyses here, where the warm core is weak, an improvement is to take the virtual temperature T_v as constant with radius. The density at r_m is then

$$\rho_m = \frac{p_c + \Delta p/e}{R_d T_v} \qquad \textbf{(4.13)}$$

whence (4.12) gives

$$\Delta p = \frac{p_c v_m^2 e}{b R_d T_v - v_m^2} \qquad \textbf{(4.14)}$$

and the radial pressure profile becomes

$$p(r) = p_c \left(1 + \frac{v_m^2 \exp(1 - (r_m/r)^b)}{b R_d T_v - v_m^2} \right) \qquad \textbf{(4.15)}$$

One advantage of this form is that the density disappears from the gradient-wind:

$$v(r) = -fr/2 + \sqrt{v_m^2 \exp(1 - (r_m/r)^b) (r_m/r)^b + (fr/2)^2} \qquad \textbf{(4.16)}$$

The iterative statistical fits require the derivatives of (4.15) and (4.16) with respect to the each of the control variables and *r*. These are

$$\begin{aligned}
\frac{\partial p}{\partial v_m} &= \frac{2 b p_c R_d T_v v_m \exp(1 - (r_m/r)^b)}{(b R_d T_v - v_m^2)^2} \\
\frac{\partial p}{\partial r_m} &= \frac{-b p_c v_m^2 \exp(1 - (r_m/r)^b) (r_m/r)^b}{r_m (b R_d T_v - v_m^2)} \\
\frac{\partial p}{\partial b} &= \frac{-p_c v_m^2 \exp(1 - (r_m/r)^b)[(b R_d T_v - v_m^2)(r_m/r)^b \log(r_m/r) + R_d T_v]}{(b R_d T_v - v_m^2)^2} \\
\frac{\partial p}{\partial p_c} &= 1 + \frac{v_m^2 \exp(1 - (r_m/r)^b)}{b R_d T_v - v_m^2} \\
\frac{\partial p}{\partial r} &= \frac{b p_c v_m^2 \exp(1 - (r_m/r)^b)(r_m/r)^b}{r(b R_d T_v - v_m^2)}
\end{aligned} \qquad \textbf{(4.17)}$$

and

$$
\begin{aligned}
\frac{\partial v}{\partial v_m} &= \frac{v_m \exp(1 - (r_m/r)^b)(r_m/r)^b}{[v_m^2 \exp(1 - (r_m/r)^b)\ (r_m/r)^b + (fr/2)^2]^{1/2}} \\
\frac{\partial v}{\partial r_m} &= \frac{b v_m^2 \exp(1 - (r_m/r)^b)\ (r_m/r)^b\ (1 - (r_m/r)^b)}{2r_m[v_m^2 \exp(1 - (r_m/r)^b)\ (r_m/r)^b + (fr/2)^2]^{1/2}} \\
\frac{\partial v}{\partial b} &= \frac{v_m^2 \exp(1 - (r_m/r)^b)\ (r_m/r)^b\ (1 - (r_m/r)^b)\ \log(r_m/r)}{2[v_m^2 \exp(1 - (r_m/r)^b)\ (r_m/r)^b + (fr/2)^2]^{1/2}} \\
\frac{\partial v}{\partial p_c} &= 0 \\
\frac{\partial v}{\partial r} &= -\frac{f}{2} + \frac{(fr)^2 - 2b v_m^2 \exp(1 - (r_m/r)^b)\ (r_m/r)^b\ (1 - (r_m/r)^b)}{4r[v_m^2 \exp(1 - (r_m/r)^b)\ (r_m/r)^b + (fr/2)^2]^{1/2}}
\end{aligned}
\qquad \textbf{(4.18)}
$$

The derivatives of p and v with respect to x_t, y_t, u_t, and v_t, are necessary for track finding. These follow from the derivatives with respect to r by a straight-forward application of the chain rule.

4.A2 The Willoughby Parametric Profile

Willoughby (2002) gives a parametric profile which he claims overcomes some of the limitations of other profiles, including that of Holland (1980). In particular, it allows a sharper maximum at the RMW, and allows the shape of the profile within and outside of the RMW to be independently adjusted. Unlike Holland's, which is written in terms of pressure and must be differentiated to find the equivalent gradient-wind, Willoughby's is written in terms of wind and must be integrated to find the pressure.

Willoughby's wind profile is given by

$$
\begin{aligned}
v_1(r) &= (v_{m1} + v_{m2})(r/r_m)^{n_1} \\
v_2(r) &= v_{m1} \exp((r_m - r)/L_1) + v_{m2} \exp((r_m - r)/L_2) \\
v(r) &= (1 - w(r))\ v_1(r) + w(r)\ v_2(r)
\end{aligned}
\qquad \textbf{(4.19)}
$$

The profile consists of the weighted average of an eye profile v_1 with shape defined by n_1 ($1 < n_1 < 2$), and an outer wind profile v_2 which is the sum of two exponentials of length scales L_1 and L_2, and amplitudes v_{m1} and v_{m2}. The maximum wind is $v_m = v_{m1} + v_{m2}$ at the RMW r_m. The weighting function increases monotonically from 0 to 1 across a blending zone of width $2L_b$ which contains r_m. The precise location of the blending zone is determined by the requirement that the maximum wind occur at r_m, and is found by solving $\partial v/\partial r = 0$ at r_m. This gives the weight at r_m as

$$w(r_m) = w_m = \frac{(v_{m1} + v_{m2})L_1L_2n_1}{v_{m1}L_2(L_1n_1 + r_m) + v_{m2}L_1(L_2n_1 + r_m)} \qquad \textbf{(4.20)}$$

which is sufficient to locate the blending zone radially. The blending function can be constructed from any suitably smooth function that goes from zero to one over a finite interval. Willoughby used a segment of a cubic polynomial, but here a quintic is preferred as the extra couple of continuous derivatives are expected to be of benefit when the profile is used for forcing the numerical model.

In particular, w is given by

$$w(r) = w_s(r_s) = \begin{cases} 0 & r_s < -1 \\ \frac{1}{2} + \frac{1}{16} r_s (3r_s^4 - 10r_s^2 + 15) & |r_s| \le 1 \\ 1 & r_s > 1 \end{cases} \qquad \textbf{(4.21)}$$

where

$$r_s(r) = \frac{r - r_m}{L_b} + r_{sm} \qquad \textbf{(4.22)}$$

and r_{sm} is the solution of $w_s(r_{sm}) = w_m$.

Physically, the eye-profile v_1 can range from solid-body rotation ($n_1 = 1$) to something more "bowl-shaped". The outer profile consists of the sum of two exponentials. An earlier version of the profile had only one (i.e. $v_{m2} = 0$) but was found to not adequately fit storms with a large radius of gales. Willoughby (personal communication, 2002) suggests L_2 would normally be several hundred kilometres, and recommends 5 km for the blending zone half-width, L_b.

In the case that $v_{m2} = 0$, the vorticity is easily shown to have a minimum at $r = (\sqrt{5}+1)L_1/2$. For realistic parameter values, this minimum is often deep enough to make the profile inertially unstable there. This instability can often be removed by adding on a little of the second exponential, since its vorticity minimum falls at a different radius, and reducing v_{m1} accordingly. Constraints on inertial stability were not applied during the statistical fits, but were imposed when the profile was used to force the model.

The derivatives of v with respect to the control vector (v_{m1}, v_{m2}, L_1, L_2, r_m, n_1) and to r, needed for the Levenberg-Marquadt fits, are straightforward, with the only complication being that the radial location of the blending zone depends on the control vector through (4.20). Incorporating this, the derivatives of w with respect to the control vector are:

$$
\begin{aligned}
\frac{\partial w}{\partial v_{m1}} &= \frac{w_s'(r_s)}{w_s'(r_{sm})}\frac{\partial w_m}{\partial v_{m1}} \\
\frac{\partial w}{\partial L_1} &= \frac{w_s'(r_s)}{w_s'(r_{sm})}\frac{\partial w_m}{\partial L_1} \\
\frac{\partial w}{\partial v_{m2}} &= \frac{w_s'(r_s)}{w_s'(r_{sm})}\frac{\partial w_m}{\partial v_{m2}} \\
\frac{\partial w}{\partial L_2} &= \frac{w_s'(r_s)}{w_s'(r_{sm})}\frac{\partial w_m}{\partial L_2} \\
\frac{\partial w}{\partial r_m} &= w_s'(r_s)\left(\frac{1}{w_s'(r_{sm})}\frac{\partial w_m}{\partial r_m} - \frac{1}{L_b}\right) \\
\frac{\partial w}{\partial n_1} &= \frac{w_s'(r_s)}{w_s'(r_{sm})}\frac{\partial w_m}{\partial n_1}
\end{aligned}
\qquad \textbf{(4.23)}
$$

The equivalent pressure profile is found by radially integrating

$$
\frac{1}{\rho}\frac{\partial p}{\partial r} = R_d T_v \frac{\partial \log(p(r))}{\partial r} = \frac{v(r)^2}{r} + fv(r) \qquad \textbf{(4.24)}
$$

A radially constant T_v, rather than constant ρ, is used for the reasons discussed above for the Holland profile. A numerical integration was deemed to be unsuitable, as the derivatives of p with respect to the control vector are also needed, and the integration needs to be done with high accuracy to avoid problems with the iterative fits. Moreover, the integration can be done analytically everywhere, although in the blending zone the analytic solution is too long to be practically useable. Inside of the blending zone, where $v = v_1$:

$$
\begin{aligned}
\frac{1}{p_c}\,p(r) &= \exp\left(\frac{(v_{m1}+v_{m2})[2fn_1r+(v_{m1}+v_{m2})(1+n_1)(r/r_m)^{n_1}](r/r_m)^{n_1}}{2R_dT_vn_1(n_1+1)}\right)\\
\frac{1}{p}\,\frac{\partial p}{\partial v_{m1}} &= \frac{[fn_1r+(v_{m1}+v_{m2})(n_1+1)(r/r_m)^{n_1}](r/r_m)^{n_1}}{R_dT_vn_1(n_1+1)}\\
\frac{\partial p}{\partial L_1} &= 0\\
\frac{1}{p}\,\frac{\partial p}{\partial v_{m2}} &= \frac{[fn_1r+(v_{m1}+v_{m2})(n_1+1)(r/r_m)^{n_1}](r/r_m)^{n_1}}{R_dT_vn_1(n_1+1)}\\
\frac{\partial p}{\partial L_2} &= 0\\
\frac{1}{p}\,\frac{\partial p}{\partial r_m} &= \frac{-(v_{m1}+v_{m2})[fn_1r+(v_{m1}+v_{m2})(n_1+1)(r/r_m)^{n_1}](r/r_m)^{n_1}}{R_dT_v(n_1+1)r_m}\\
\frac{1}{p}\,\frac{\partial p}{\partial n_1} &= \frac{(v_{m1}+v_{m2})(r/r_m)^{n_1}}{2R_dT_vn_1^2(n_1+1)^2}\Big(-2fn_1^2r-(v_{m1}+v_{m2})(n_1+1)^2(r/r_m)^{n_1}\\
&\quad +2n_1(n_1+1)[fn_1r+(v_{m1}+v_{m2})(n_1+1)(r/r_m)^{n_1}]\log(r/r_m)\Big)\\
\frac{1}{p}\,\frac{\partial p}{\partial p_c} &= p_c\\
\frac{1}{p}\,\frac{\partial p}{\partial r} &= \frac{(v_{m1}+v_{m2})[fr+(v_{m1}+v_{m2})(r/r_m)^{n_1}](r/r_m)^{n_1}}{rR_dT_v}
\end{aligned}
\qquad \textbf{(4.25)}
$$

On the outside of the blending zone, some lengthy expressions arise:

$$
\begin{aligned}
p(r) = p_{b2}\exp\Bigg(&\frac{1}{R_dT_v}\Big(fv_{m1}L_1[\exp((r_m-r_{b2})/L_1)-\exp((r_m-r)/L_1)]\\
&+fv_{m2}L_2[\exp((r_m-r_{b2})/L_2)-\exp((r_m-r)/L_2)]\\
&+v_{m1}^2\exp(2r_m/L_1)[\mathrm{Ei}(-2r/L_1)-\mathrm{Ei}(-2r_{b2}/L_1)]\\
&+v_{m2}^2\exp(2r_m/L_2)[\mathrm{Ei}(-2r/L_2)-\mathrm{Ei}(-2r_{b2}/L_2)]\\
&+2v_{m1}v_{m2}\exp(r_m(1/L_1+1/L_2))\times\\
&\qquad[\mathrm{Ei}(-r(1/L_1+1/L_2))-\mathrm{Ei}(-r_{b2}(1/L_1+1/L_2))]\Big)\Bigg)
\end{aligned}
\qquad \textbf{(4.26)}
$$

$$\frac{1}{p(r)}\frac{\partial p(r)}{\partial v_{m1}} = \frac{1}{p_{b2}}\frac{\partial p_{b2}}{v_{m1}} + \frac{1}{R_d T_v}\Big(fL_1[\exp((r_m - r_{b2})/L_1) - \exp((r_m - r)/L_1)] + 2v_{m1}\exp(2r_m/L_1)[\mathrm{Ei}(-2r/L_1) - \mathrm{Ei}(-2r_{b2}/L_1)] + 2v_{m2}\exp(r_m(1/L_1 + 1/L_2)) \times [\mathrm{Ei}(-r(1/L_1 + 1/L_2)) - \mathrm{Ei}(-r_{b2}(1/L_1 + 1/L_2))]\Big) \quad \textbf{(4.27)}$$

$$\frac{1}{p(r)}\frac{\partial p(r)}{\partial L_1} = \frac{1}{p_{b2}}\frac{\partial p_{b2}}{\partial L_1} + \frac{1}{R_d T_v}\Big(fv_{m1}\Big[\exp((r_m - r_{b2})/L_1)(1 + (r_{b2} - r_m)/L_1) - \exp((r_m - r)/L_1)(1 + (r - r_m)/L_1)\Big] + \frac{v_{m1}^2}{L_1}\Big[\exp(2(r_m - r_{b2})/L_1) - \exp(2(r_m - r)/L_1)\Big] + \frac{2r_m v_{m1}^2 \exp(2r_m/L_1)}{L_1^2}\Big[\mathrm{Ei}(-2r_{b2}/L_1) - \mathrm{Ei}(-2r/L_1)\Big] + \frac{2v_{m1}v_{m2}L_2}{L_1(L_1 + L_2)}\Big[\exp((r_m - r_{b2})(1/L_1 + 1/L_2)) - \exp((r_m - r)(1/L_1 + 1/L_2))\Big] + \frac{2v_{m1}v_{m2}\, r_m \exp(r_m(1/L_1 + 1/L_2))}{L_1^2} \times \Big[\mathrm{Ei}(-r_{b2}(1/L_1 + 1/L_2)) - \mathrm{Ei}(-r(1/L_1 + 1/L_2))\Big]\Big) \quad \textbf{(4.28)}$$

$$\frac{1}{p(r)}\frac{\partial p(r)}{\partial v_{m2}} = \frac{1}{p_{b2}}\frac{\partial p_{b2}}{\partial v_{m2}} + \frac{1}{R_d T_v}\Big(fL_2[\exp((r_m - r_{b2})/L_2) - \exp((r_m - r)/L_2)] + 2v_{m2}\exp(2r_m/L_2)[\mathrm{Ei}(-2r/L_2) - \mathrm{Ei}(-2r_{b2}/L_2)] + 2v_{m1}\exp(r_m(1/L_1 + 1/L_2)) \times [\mathrm{Ei}(-r(1/L_1 + 1/L_2)) - \mathrm{Ei}(-r_{b2}(1/L_1 + 1/L_2))]\Big) \quad \textbf{(4.29)}$$

$$\frac{1}{p(r)}\frac{\partial p(r)}{\partial L_2} = \frac{1}{p_{b2}}\frac{\partial p_{b2}}{\partial L_2}$$
$$+ \frac{1}{R_d T_v}\Big(f v_{m2}\Big[\exp((r_m - r_{b2})/L_2)(1 + (r_{b2} - r_m)/L_2)$$
$$- \exp((r_m - r)/L_2)(1 + (r - r_m)/L_2)\Big]$$
$$+ \frac{v_{m2}^2}{L_2}\Big[\exp(2(r_m - r_{b2})/L_2) - \exp(2(r_m - r)/L_2)\Big]$$
$$+ \frac{2v_{m2}^2 r_m \exp(2r_m/L_2)}{L_2^2}\Big[\mathrm{Ei}(-2r_{b2}/L_2) - \mathrm{Ei}(-2r/L_2)\Big]$$
$$+ \frac{2v_{m1}v_{m2}L_1}{L_2(L_1+L_2)}\Big[\exp((r_m - r_{b2})(1/L_1+1/L_2)) - \exp((r_m - r)(1/L_1+1/L_2))\Big]$$
$$+ \frac{2v_{m1}v_{m2}r_m \exp(r_m(1/L_1+1/L_2))}{L_2^2}$$
$$\times\Big[\mathrm{Ei}(-r_{b2}(1/L_1+1/_2)) - \mathrm{Ei}(-r(1/L_1+1/L_2))\Big]\Big) \quad \textbf{(4.30)}$$

$$\frac{1}{p(r)}\frac{\partial p(r)}{\partial n_1} = \frac{1}{p_{b2}}\frac{\partial p_{b2}}{\partial n_1} \quad \textbf{(4.31)}$$

$$\frac{1}{p(r)}\frac{\partial p(r)}{\partial r_m} = \frac{1}{p_{b2}}\frac{\partial p_{b2}}{\partial r_m} + \frac{1}{R_d T_v}\Big(fv_{m1}\left[\exp((r_m - r_{b2})/L_1) - \exp((r_m - r)/L_1)\right] + fv_{m2}\left[\exp((r_m - r_{b2})/L_2) - \exp((r_m - r)/L_2)\right] + \frac{2v_{m1}^2\exp(2r_m/L_1)}{L_1}\left[\mathrm{Ei}(-2r/L_1) - \mathrm{Ei}(-2r_{b2}/L_1)\right] + \frac{2v_{m2}^2\exp(2r_m/L_2)}{L_2}\left[\mathrm{Ei}(-2r/L_2) - \mathrm{Ei}(-2r_{b2}/L_2)\right] + 2v_{m1}v_{m2}(1/L_1 + 1/L_2)\exp(r_m(1/L_1 + 1/L_2)) \times \left[\mathrm{Ei}(-r(1/L_1 + 1/L_2)) - \mathrm{Ei}(-r_{b2}(1/L_1 + 1/L_2)\right]\Big) \quad \textbf{(4.32)}$$

$$\frac{1}{p(r)}\frac{\partial p(r)}{\partial p_c} = \frac{1}{p_{b2}}\frac{\partial p_{b2}}{\partial p_c} \quad \textbf{(4.33)}$$

where Ei is the exponential integral function, and p_{b2} is the pressure at the r_{b2}, found as described below.

These are not the full expressions for the derivatives of p with respect to the control vector. There are some small but complicated terms which result because the location of the blending zone depends on the control vector, which have been omitted. Given the complexity of the equations, the pragmatic view was taken that it was easier to use the Levenberg-Marquadt iteration for a simplified profile in which the location of the blending zone was fixed, and enclose this in another iteration to calculate that location.

Within the blending zone, the gradient-wind integration is in principal solvable analytically for polynomial weighting functions. However, attempts with symbolic algebra software yielded expressions containing thousands of terms, so this part of the integration was done numerically. Derivatives with respect to the control vector in this annulus were found using

$$\frac{1}{p(r)}\frac{\partial p(r)}{\partial v_{m1}} = \int_{r_{b1}}^{r} \frac{1}{R_d T_v}\left(\frac{2v(s)}{s} + f\right)\frac{\partial v(s)}{\partial v_{m1}}\,ds + \frac{1}{p_{b1}}\frac{\partial p_{b1}}{\partial v_{m1}} \qquad \textbf{(4.34)}$$

and similarly for the remainder of the control vector. Here s is a dummy variable for the integration, which is done numerically. These integrations also gave p_{b2} and its derivatives, required for the outer part of the vortex.

4.A3 Some Notes on the Levenberg-Marquadt Fitting Procedure

This appendix begins by briefly outlining how Levenberg-Marquadt algorithm works, followed by some extensions used here. The first part closely follows the treatment in Press et al. (1992, section 15.5).

Suppose there are N observations y_i with error variance σ_i^2 at points x_i, to which to fit a curve $y_i = \varphi(x_i; \boldsymbol{a})$ where $\boldsymbol{a} = (a_1, \ldots a_m)$ is a vector of parameters. Then the minimum variance fit is found by minimising the cost function

$$J(\boldsymbol{a}) = \sum_{i=1}^{N} \frac{(y_i - \varphi(x_i; \boldsymbol{a}))^2}{\sigma_i^2} \qquad \textbf{(4.35)}$$

At the minimum,

$$\beta_k = -\frac{1}{2}\frac{\partial J}{\partial a_k} = \sum_{i=1}^{N}\frac{(y_i - \varphi(x_i;\, \boldsymbol{a}))}{\sigma_i^2}\frac{\partial \varphi}{\partial a_k} = 0 \qquad \textbf{(4.36)}$$

The second derivatives of J are approximated by

$$\alpha_{kl} = \frac{1}{2}\frac{\partial^2 J}{\partial a_k \partial a_l} = \sum_{i=1}^{N}\frac{1}{\sigma_i^2}\frac{\partial \varphi}{\partial a_k}\frac{\partial \varphi}{\partial a_l} \qquad \textbf{(4.37)}$$

The latter has terms in $\partial^2\varphi/\partial a_k \partial a_l$ omitted for the reasons given in Press et al. (1992). Then each step in the iteration involves solving a linear equation for an increment $\boldsymbol{\delta a}$ to $\boldsymbol{a}$,

$$([\alpha_{kl}]\otimes(\mathbf{1} + \lambda \boldsymbol{I}))\ \delta \boldsymbol{a} = [\beta_k] \qquad \textbf{(4.38)}$$

where $\mathbf{1}$ is the $N\times N$ matrix of ones, $\boldsymbol{I}$ is the $N\times N$ identity matrix, and $\otimes$ denotes the Schur (i.e. element-wise) matrix product. The parameter λ, which controls the extent to which the diagonal of $[\alpha_{kl}]$ is inflated, is adjusted during the iteration depending on whether the previous trial increment $\delta\boldsymbol{a}$ reduced J. In the limit of large λ, (4.38) reduces to a steepest-descent algorithm with the step length set by $1/(\lambda\alpha_{kk})$, while for $\lambda = 0$, it reduces to solving a second-order Taylor-series approximation to (4.25). The parameter λ is adjusted during the iteration, depending on the success or otherwise of previous steps, to give an appropriate compromise between these extremes.

Equation 4.38 was solved by Q-R decomposition except when the matrix became ill-conditioned. In those cases, singular-value decomposition of the matrix allowed the identification of the element of $\boldsymbol{a}$ which could not have an increment accurately

calculated. This element was then held constant for that iteration.

The first extension to the above is used in fitting a pressure profile and the track simultaneously; that is, in the translating-pressure-fit track-finding method. The vector ***a*** includes the parameters for the chosen pressure profile, as well as four extra elements representing the offset from the origin and velocity of the track. The independent variables x_i are replaced by triplets representing the position and time of the observation, and the fitted profile function modified to include the earth-relative to storm-relative coordinate transformation. The remainder of the algorithm is unaffected by this change.

The second extension, used in the translating-wind-fit track finding method, is slightly less trivial. Here, the observations $y_i = (u_i, v_i)$ are wind vectors, and the aim is to fit a parametric wind profile φ to their azimuthal component. Thus the control vector ***a*** will contain parameters for both the shape of the profile, and for the track. Now, the projection of (u_i, v_i) into cylindrical coordinates depends on the track part of the ***a***. To accommodate this, it is necessary is to redefine α and β:

$$\begin{aligned}\beta_k &= -\frac{1}{2}\frac{\partial J}{\partial a_k} \\ &= \sum_{i=1}^{N} \frac{1}{\sigma_i^2}\left(f_1(\boldsymbol{a})u_i + f_2(\boldsymbol{a})v_i - \varphi(x_i;\, \boldsymbol{a})\right)\left(\frac{\partial f_1}{\partial a_k}u_i + \frac{\partial f_2}{\partial a_k}v_i - \frac{\partial \varphi}{\partial a_k}\right)\end{aligned} \qquad \textbf{(4.39)}$$

$$\begin{aligned}\alpha_{kl} &= \frac{1}{2}\frac{\partial^2 J}{\partial a_k \partial a_l} \\ &= \sum_{i=1}^{N} \frac{1}{\sigma_i^2}\left(\frac{\partial f_1}{\partial a_k}u_i + \frac{\partial f_2}{\partial a_k}v_i - \frac{\partial \varphi}{\partial a_k}\right)\left(\frac{\partial f_1}{\partial a_l}u_i + \frac{\partial f_2}{\partial a_l}v_i - \frac{\partial \varphi}{\partial a_l}\right)\end{aligned} \qquad \textbf{(4.40)}$$

Here $f_1(\boldsymbol{a})$ and $f_2(\boldsymbol{a})$ are components of the projection of (u_i, v_i) to the azimuthal wind v_{az}:

$$v_{\mathrm{az}} = f_1(\boldsymbol{a})u_i + f_2(\boldsymbol{a})v_i \qquad \textbf{(4.41)}$$

It is physically preferable to make v_{az} the storm-relative, rather than the earth-relative, azimuthal wind, but as far as the algorithm is concerned, the difference only occurs in the definition of f_1 and f_2. The terms involving the second derivatives of f_1 and f_2 are omitted from (4.40) for precisely the reasons given for the omission of the second derivative of φ, and the remainder of the algorithm is identical.

The final extension involves the situation where both the x_i and y_i have errors. The cost function J is the sum of squared differences between the observations and the fitted value, normalised by the variance of this difference. When the x_i has insignificant errors, so does the fitted value $\varphi(x_i; \boldsymbol{a})$, and the variance of the difference is just the variance of the errors in the y_i. For the more general case,

$$J(\boldsymbol{a}) = \sum_{i=1}^{N} \frac{(y_i - \varphi(x_i; \boldsymbol{a}))^2}{\mathrm{Var}(y_i) + (\partial\varphi/\partial x_i)^2 \mathrm{Var}(x_i)} \qquad \textbf{(4.42)}$$

where Var denotes the variance of the error. Here, the errors in x_i and y_i are assumed to be independent, so that

$$\mathrm{Var}(y_i - \varphi(x_i; \boldsymbol{a})) = \mathrm{Var}(y_i) + \mathrm{Var}(\varphi(x_i; \boldsymbol{a})) \qquad \textbf{(4.43)}$$

Expanding φ as a Taylor series in x, and using the definition of variance,

$$\mathrm{Var}(\varphi(x_i;\ \boldsymbol{a})) \ = \ \left(\frac{\partial \varphi}{\partial x} \right)^2 \ \mathrm{Var}(x_i) \qquad \textbf{(4.44)}$$

and (4.42) follows immediately.

The minimisation was performed as above, with $\partial\varphi/\partial x$ evaluated at each iteration using the value of $\boldsymbol{a}$ from the previous step. It is clear that J decreases as $|\partial\varphi/\partial x|$ increases; thus fits which incorporate this term will tend to fit a steeper gradient, particularly in data-dense areas, than those which omit it.